DANMARKS OG GRØNLANDS
GEOLOGISKE UNDERSØGELSE
RAPPORT 1996/53

Mass balance and related topics of the Greenland ice sheet

Report of the 6th workshop

Editor Ole B. Olsen

GEUS

DANMARKS OG GRØNLANDS
GEOLOGISKE UNDERSØGELSE
RAPPORT 1996/53

Mass balance and related topics of the Greenland ice sheet

Report of the 6th workshop

Held at
Geological Survey of Denmark and Greenland,
Copenhagen, Denmark, 22nd - 23rd january 1996

Editor Ole B. Olsen

GEUS
Geological Survey of
Denmark and Greenland

Contents

Introduction

The 'Sixth Workshop on Mass Balance and related Topics of the Greenland Ice Sheet' took place at the Geological Survey of Denmark and Greenland (former Geological Survey of Greenland), Copenhagen, Denmark on January 22nd and 23rd 1996). The workshop was attended by 25 participants and 17 papers were presented.

Although the workshops were initially intended as a forum for discussion of plans, experiences and results from 'mass and energy balance studies related to the Greenland ice sheet', this year's workshop included results from both Scandinavia and North America. This was very appropriate in view of the proposal from N. Reeh (included in the final circular) to extend the geographical area covered by the Greenland mass balance workshops to the entire arctic region.

At the end of the workshop J. O. Hagen further amplified and seconded that the geographical area of interest of future workshops should include all of the arctic region. The meeting unanimously agreed on this, and that future workshops should be named 'Arctic Glaciers and Ice Sheets'.

It was also proposed that the workshop should be organised with presentation of papers in the morning and smaller specialised discussion groups in the afternoon, even if this meant extending the workshop over more days. There was a general consensus that this might be a suitable basis for future workshops.

As to the next workshop no final agreement was reached on the location but Norway (J. O. Hagen), Sweden (P. Holmlund) or England (R. Braithwaite) are the most likely candidates.

O. B. Olesen

Participants and addresses

Dr. Roger Braithwaite
Geography - Mansfield Cooper Bldg.
University of Manchester
Oxford Road
Manchester M13 9PL, England
UK
Tel. (int.+44) 61 275 3644 (direct)
Tel. (int.+44) 61 275 3636 (message)
Fax (int.+44) 61 273 4407
e-mail r.braithwaite@man.ac.uk

Carl Egede Bøggild
Danmarks og Grønlands Geologiske
Undersøgelse
Thoravej 8
DK-2400 København NV
Denmark
Tel. (int.+45) 31 10 66 00
FAX (int.+45) 31 19 68 68
e-mail boeggild@geus.dk

Dr. Dorthe Dahl-Jensen
Niels Bohr Institutet
for Astronomi, Fysik og Geofysik
Geofysisk Afdeling
Rockefeller Komplekset
Juliane Maries Vej 30
2100 København Ø
Denmark
Tel +45 3532 0560
FAX +45 3536 5357
E-mail: ddj@osiris.gfy.ku.dk

Simon Ekholm
Kort- og Matrikelstyrelsen
Geodætisk Afdeling
Rentemestervej 8
DK-2400 København NV
Denmark
tel.: +45 3587 5317
fax: +45 3587 5052
e-mail: se@kms.min.dk

Hubertus Fischer
Universität Heidelberg
Institut für Umweltphysik
Im Neuenheimer Feld 366
D-69120 Heidelberg
Germany
Tel. (int.+49) 6221 563315
Fax (int.+49) 6221563405
e-mail: fi@uphys1.uphys.uni-heidelberg.de

Jann Forrer-Bergamin
ETH Zürich
Geograhisches Institut
Winterthurerstr. 190
CH-8057 Zürich
Schweiz
Tel. (int.+41) 1257 5208
Fax (int.+41) 1362 5197
e-mail: forrer@geo.umnu.ethz.ch

René Forsberg
Kort- og Matrikelstyrelsen
Rentemestervej 8
DK-2400 København NV
Denmark
tel: +45 3587 5319
fax: +45 3587 5+052
e-mail: rf@kms.min.dk

Preben Gudmandsen
Electromagnetic Institute
Technical University of Denmark
Building 348
DK-2800 Lyngby
Denmark
tel.: +45 4525 3788
fax: +45 4593 1634
e-mail: pg@emi.dtu.dk

Dr. Jon Ove Hagen
Department of Geography
University of Oslo
Postboks 1042, Blindern
N-0316 Oslo
Norway
Tel. (int.+47) 2285 4038
FAX (int.+47) 2285 7230
e-mail: j.o.hagen@geografi.uio.no

Günther Heinemann
Meteorologisches Institut Univ. Bonn
Auf dem Hügel 20
53121 Bonn
Germany
Tel. (int.+49) 228 735 102
FAX (int.+49) 228 735 188
e-mail unf410@ibm.rhrz.uni-bonn.de

Dr. Per Holmlund
Dept.- of Physical Geography
Stockholm University
S-10691 Stockholm
Sweden
tel: +46 8 164 811
fax: +46 8 164 818
e-mail: pelle@natgeo.su.se

Christine S. Hvidberg
Niels Bohr Institutet
for Astronomi, Fysik og Geofysik
Geofysisk Afdeling
Rockefeller Komplekset
Juliane Maries Vej 30
DK-2100 København Ø
Denmark
Tel +45 3532 0560
FAX +45 3536 5357

Kristian Keller
Niels Bohr Institutet for
Astronomi, Fysik og Geofysik
Geofysisk Afdeling
Rockefeller Komplekset
Juliane Maries Vej 30
DK-2100 København Ø
Denmark
Tel +45 3532 0586
FAX +45 3536 5357
e-mail kk@gfy.ku.dk

O. Leeuwenburgh
Niels Bohr Institutet
for Astronomi, Fysik og Geofysik
Geofysisk Afdeling
Rockefeller Komplekset
Juliane Maries Vej 30
DK-2100 København Ø
Denmark
Tel +45 3532 0560
FAX +45 3536 5357
E-mail: ol@gfy.ku.dk

Dr. Anton G. C. A. Meesters
Vrije Universiteit Amsterdam
Faculty of Earth Sciences
De Boelelaan 1085
NL-1081 HV Amsterdam
the Netherlands
Tel. +31 20 444 7362
Fax +31 20 646 2457
e-mail: meea@geo.vu.nl

Johan Jacob Mohr
Danish Center for Remote Sensing
Electromagnetics Institute
Technical University of Denmark
B 348
DK-2800 Lyngby
Denmark
Tel +45 4525 3800
FAX +45 4593 1634
e-mail jm@emi.dtu.dk

Gunthard Niederbäumer
ETH Zürich
Geographisches Institut
Winterthurerstr. 190
CH-8057 Zürich
Schweiz
Tel. +41 1 257 5206
Fax +41 1 362 5197
e-mail: gunthard@geo.umnw.ethz.ch

Dr. Friedrich Obleitner
Universität Innsbruck
Institut für Geophysik und Meteorologie
Innrain 52
A-6020 Innsbruck
Austria
Tel. (int.+43) 512 507 5451
Fax (int.+43) 512 507 2924
e-mail meteorologie@uibk.ac.at

Ole B. Olesen
Danmarks og Grønlands Geologiske
Undersøgelse
Thoravej 8
DK-1350 København
Denmark
Tel.: (int.+45) 31 10 66 00
Fax.: (int.+45) 31 19 68 68
e-mail oleseno@geus.dk

Dr. W. Tad Pfeffer
University of Colorado
Inst. of Arctic and Alpine Research
CB 450
Boulder CO 80309
USA
Tel. +1 303 492 6387
Fax. +1 303 492 6388
e-mail: pfeffer@tintin.colorado.edu

Niels Reeh
Dansk Polarcenter/Danmarks og Grønlands
Geologiske Undersøgelse
Thoravej 8
DK-2400 København NV
Denmark
Tel. (int.+45) 31 10 66 00
FAX (int.+45) 31 19 68 68
e-mail: reeh@geus.dk

Matthias Schwager
AWI
Sektion Geophysik/Glaziologie
Postfach 120161
D-27515 Bremerhaven
Germany
Tel.: +49 471 4831 175
Fax: +49 471 4831 149
e-mail: mschwage@awi-bremerhaven.de

Prof. Dr.-Ing. Manfred Stober
Fachhochschule Stuttgart
Hochschule für Technik
Schellingstr. 24
D-70174 Stuttgart
Germany
Tel. (Int.+49) 711 121 2563
Fax (Int.+49) 711 121 2666

Henrik Højmark Thomsen
Danmarks og Grønlands Geologiske
Undersøgelse
Thoravej 8
DK-2400 København NV
Denmark
Tel.: (int.+45) 31 10 66 00
Fax.: (int.+45) 31 19 68 68
E-mail: hoejmark@geus.dk

Dr. A. Weidick
Danmarks og Grønlands Geologiske
Undersøgelse
Thoravej 8
DK-2400 København NV
Denmark
Tel. (Int.+45) 31 10 66 00
Fax (Int.+45) 31 19 68 68

APPLICATION OF INTERFEROMETRY TO STUDIES OF GLACIER DYNAMICS

Johan Jacob Mohr

Danish Center for Remote Sensing, Dept. of Electromagnetic Systems
Technical University of Denmark, B-348, DK-2800 Lyngby, Denmark
Phone: +45 4525 3800, Fax: +45 4593 1634, Email: jm@emi.dtu.dk

ABSTRACT

Interferometric synthetic aperture radar (SAR) has the potential for measurements of changes from one image to another with sub-millimeter accuracy, thus being a promising tool for studies of glacier dynamics. The Danish Center for Remote Sensing[†] has in corporation with Danish Polar Center (DPC) established a test cite on the Storstrømmen glacier in North East Greenland. DCRS has with EMISAR[††] on one day in august 1994 acquired C-band repeat track interferometry (RTI) data over the glacier and again on two consecutive days in august 1995 acquired L-band RTI and C-band across track interferometry data. DPC has in 1994 deployed corner reflectors on the glacier and performed in-situ measurements of the glacial flow. Tandem mode interferometry data from the ERS-1/2 satellites has also been investigated.

INTRODUCTION

With synthetic aperture radar (SAR) Interferometry two radar images (acquired either from a satellite or an airplane) are combined to an interferogram. This allows the detection of geometrical distortions between the two images with sub-millimeter accuracy. If the images are acquired from flight tracks separated spatially, i.e. having a spatial baseline, the viewing geometry for the two images will be slightly different and a potential for estimation of topography arises, [1]. If, on the contrary, the images are acquired from exactly the same track but at different times, i.e. having a temporal baseline, small differences caused by a physical change in the scene can be detected i.e. a potential for velocity and displacement measurements exists, [2]. Note that only changes in the radar to pixel line of sight direction can be measured.

In general a spatial baseline as well as a temporal baseline will be present and topography as well as (line of sight) glacial movement will therefore contribute to the interferogram phase. In one interferogram generated from to images denoted 1 and 2, the pixel phase φ_{12} are (to first order)

$$\varphi_{12} = -\frac{4\pi}{\lambda}\left(B_{\parallel,12} + B_{\perp,12}\Delta\theta - T_{12}v_{12}\right) + \varepsilon_{12} \qquad (1)$$

[†] The Danish Center for Remote Sensing (DCRS) is established and funded by the Danish National Research Foundation.

[††] Development of the EMISAR was sponsored by the Thomas B. Thriges Foundation, the Danish Technical Research Counsil (STVF), the Royal Danish Air Force (RDAF), the Technical University of Denmark and the Joint Research Centre (JRC).

where λ denotes the radar wavelength, $B_{\|,12}$ the parallel and $B_{\perp,12}$ the perpendicular baseline (assuming flat earth), $\Delta\theta$ the angular deviation from the reference surface, $T_{12}v_{12}$ the line of sight (LOS) motion of the scene in the pixel and ε_{12} the phase noise, [3],. see Fig. 1. The parallel baseline component only depend on the acquisition geoemtry and are initially removed - a processes also called interferogram flattening. Now for the application of interferometry to studies of glacial flow the topography component, $B_{\perp,12}\Delta\theta$, need to be separated from the flow component, $T_{12}v_{12}$. One obvious solution is to utilize another interferogram generated either with one image in common with the first interferogram giving the pixel phase, φ_{23}, or from two completely different images (3 and 4) covering the same area, [3]. The interferogram phase φ_{23} are similar to (1)

$$\varphi_{23} = -\frac{4\pi}{\lambda}\left(B_{\|,23} + B_{\perp,23}\Delta\theta - T_{23}v_{23}\right) + \varepsilon_{23} \tag{2}$$

Now if the glacial velocity is constant it can be extracted from (1)-(2) if the baseline parameters can be estimated with sufficient accuracy. The critical part is the spatial baselines, since an error is directly reflected in the measurement of displacement from which the velocities are calculated. The temporal baselines are usually known with great accuracy.

Other options exists to separate the velocity and topography components. The most simple (but very rare) is that $B_{\perp}$ by change is zero. Another approach is to supply the angular deviation, $\Delta\theta$, caused by topography from another source. Though apparently simple, the method has the practical problem that elevation data (e.g. from a DEM) must be co-registered with radar data. The other drawback is of course that elevation data of Arctic regions are note widely available.

EXPERIMENTS ON STORSTRØMMEN

Two projects at the Danish Center for remote Sensing are dedicated to an investigation of 'the utility of repeat track interferometry for studies of glacier dynamics'. One concerns the airborne EMISAR data acquired by DCRS another satellite data from the ERS-1/2 satellites launched by the European Space Agency (ESA). For both studies Storstrømmen is selected as the test area.

The airborne EMISAR experiments is conducted in a 10 km (N-S) times 30 km (E-W) area in the lower part of Storstrømmen. In 1994 the Danish Polar Center deployed four corner reflectors on

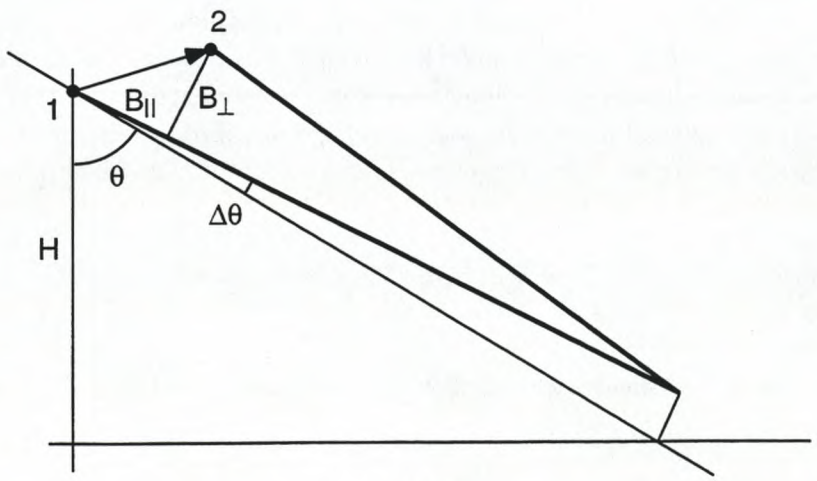

Figure 1.
The viewinng geometry.

solid rock in the test area and measured their position by GPS; two on the semi-nunatak, two on the mountains in the western part of the area. In 1995 the four reflectors was checked and their position remeasured.

The reflectors serve as reference points for the repeat track interferometry (RTI) data acquired with EMISAR. In august 1994 the area was covered with C-band RTI data on a one day mission. In august 1995 L-band data was acquired on two consecutive days, thus giving a one day temporal baseline - an order of magnitude greater than in the 1994 data. The data has been focused and interferograms has been formed. The interferograms shows very low phase noise and are easily unwrapped. The uncertainties on the baseline estimates, though reduced from several meters to the centimeter level, are still not sufficiently accurate to be used for an extraction of the glacial velocity know to be in the order of some m/y. The major unknown, now being investigated, is probably a very low frequent drift in the Inertial Navigation Unit (INU) measuring the aircraft movements around the reference track.

The other project concerns data from ERS-1 (launched June, 1991) and it successor ERS-2 (launched April , 1995). The satellites are until May 16., 1996 operated in a tandem mode such that, seen from the earth, ERS-2 repeats the ERS-1 trajectory with a one day delay. The satellites are in a 35 day repeat cycle (corresponding to 501 revolutions), thus allowing the generation of one interferogram with a one day temporal baseline each 35 day.

The raw data from ESA has been cleaned, data are focused, baselines estimated and interferograms formed. The interferograms still has a minor baseline residual, but since the trajectories are known to be perfectly straight lines this is much more easy to remove than in the airborne case. The major problem with the satellite data is phase unwrapping. The interferograms are quite noisy and some work needs to be done before an automatic phase unwrapping can be performed. The interferogram from images acquired 35 days later has also been generated, but due to the phase unwrapping problems a resulting velocity product has not yet been generated.

The results, though, are quite promising. On Fig. 2 a raw interferogram covering a 100 km times 200 km area around Storstrømmen is shown. On the left the interferogram phase is shown on the right the amplitude. The phase is color coded and is repeated for each 2π, in this case corresponding to either a change in the terrain height of 800 m or a line of sight motion of 2.8 cm/day. Careful counting of the fringes on the mountains shows that a minor tilt of 1-2 fringes is still present. It is also noted (what is confirmed by a fringe counting on the mountains) that the topography in this area can account for at most 2 fringes. With this in mind the fringe pattern on the upper part of the glacier (with an eastward flow) must be due to an horizontal surface velocity of approximately 300 m/y in the central part decreasing to approximately zero at the sides. The almost vanishing fringe pattern on the lower part (with a southward flow) can not easily be interpreted because only the line of sight component of the motion can be determined, thus giving virtually no sensitivity on the velocity measurement with this flow direction.

AIRBORNE VS. SATELLITE INTERFEROMETRY

From an end user point of view the most obvious advantages and disadvantages of airborne vs. satellite interferometry are:

- **Coverage and resolution.** Satellite images has large coverage and coarse resolution. Data amounts as well as acquisition time limits the coverage of an airborne sensor. One airborne

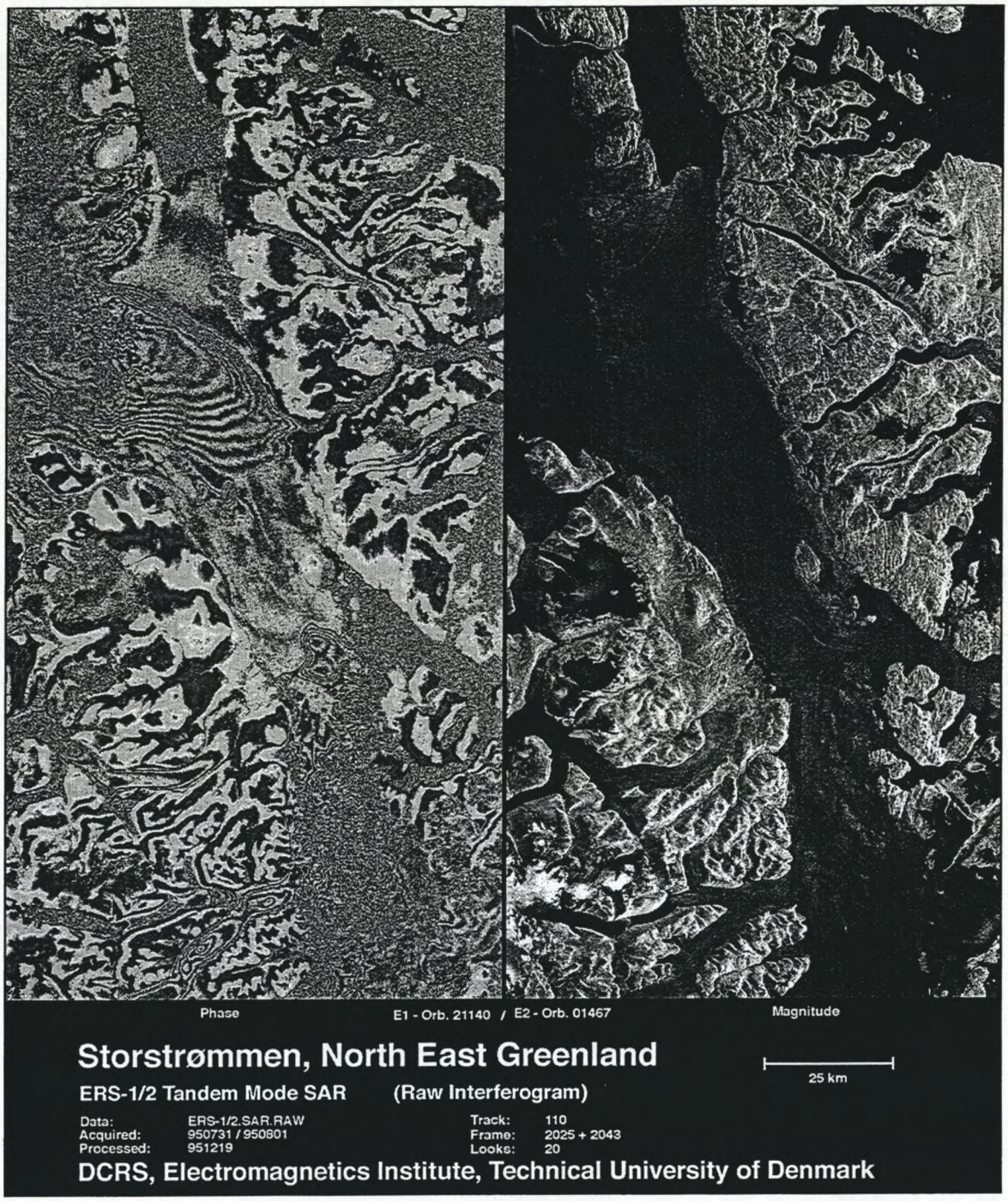

Figure 2.

Raw interferogram from ERS-1/2 tandem data.

image of the 10 km times 30 km test fields has approximately the same size (1 Gbyte) as the full 100 km times 200 km ERS image. Also note that at least 10 tracks of approximately 200 km is needed to cover the full ERS scene with airborne data - at least an order of magnitude more than feasible within one flight.

- **Spatial availability.** With satellite the imaged areas are predetermined since the satellite tracks are predetermined, as opposed to airborne interferometry. On the other hand, if a satellite cover the interesting area, one gets repeated coverage's of this with almost no extra effort.

- **Temporal availability.** The satellite data has a fixed temporal baseline. The spatial baseline for an airborne system can in principle be chosen freely, but of course cost issues are of major importance. Also note that the ERS-1/2 tandem mission terminates on May 16, 1996.

- **Velocity modeling.** Again since the satellite tracks are predetermined only one velocity component can be measured. In special cases descending as well ascending orbit data are available, but at least in the ERS case the angle between the tracks will be small (20°-30°). With airborne interferometry the possibility of coverage's from different angles exists, in principle enabling the measurement of the 2-D (or even the 3-D) velocity pattern.

From an engineering point of point of view other issues are also important. Airborne interferogram are usually easy to unwrap as opposed to satellite. On the other hand baseline estimation is much more difficult in airborne system.

CONCLUSION

A processor for focusing of airborne as well as satellite data has been developed. Raw data from the ERS-1/2 satellites has been cleaned and processed and the (relative) spatial baselines are estimated to within 10 cm. Precision orbit data are now available from ESA with a similar accuracy, and might in the future be integrated. The interferograms has, due to phase noise, not yet been unwrapped. The interferograms, though, looks quite promising for velocity estimation. Airborne data on the other hand unwraps well. The uncertainty on the spatial baselines has been reduced from several meters to the centimeter level, but since the residual errors are not linear but rather caused by a small drift in the INU, this is not sufficiently accurate. Work on the estimation of such a non-linear baseline uncertainty is in progress.

REFERENCES

[1] H.A. Zebker and R.M. Goldstein, "Topographic Mapping from Interferometric Synthetic Aperture Radar Observations", J. of Geophys. Res., 91(B5), pp. 4993-4999, April 1986.

[2] Goldstein, R.M., H. Engelhardt, B. Kamb andR.M. Frolich, "Satellite Radar Interferometry for Monitoring Ice Sheet Motion: Application to an Arctic Ice Stream", Science, Vol. 262, pp. 1282-1285.

[3] Søren N. Madsen and Howard Zebker, "Imaging Radar Interferometry", chapter 17 in Manual of Remote Sensing, Vol III, 1996, in press.

ABOUT THE ACCURACY OF THE LEVELLING METHODS ALONG THE EGIG LINE

Manfred **Stober**

Fachhochschule Stuttgart -Hochschule für Technik-
Stuttgart, FRG

1. Height measurements in the EGIG line.

The EGIG line is crossing the Greenland ice sheet from West to East in a latitude of about 70-72° North. For determining the heights several campaigns had been performed and different measuring methods had been applied. Terrestrial levelling methods were used in:

1959: Geometric levelling from A14 (West) to T53 (MÄLZER 1964),
1968: Geometric levelling A14 - Cecilia Nunatak (SECKEL 1977),
1990/92: Trigonometric levelling T1 (West) - Cecilia Nunatak (MÖLLER 1994).

Completely different methods using satellite altimetry had been applied in the eighties (ZWALLY 1989) and recently (ANDERSEN 1994).

The resulting temporal height changes in the western part of the EGIG-line are contradicting. So we obtain from terrestrial levellings:

1959 --▸ 1968 : + 1,1 m = + 0,12 m/year ,
1968 --▸ 90/92 : - 3,6 m = - 0,15 m/year ,

From satellite altimetry ZWALLY 1989 has derived a growth of +0,2...0,3 m/year and ANDERSEN 1994 has found an amplitude of annual variations (summer/winter) of 0,39 m.

To evaluate the results of levelling methods we have to discuss the possible systematic and random errors. These are mainly:
- random measuring errors in aiming and reading,
- sinking of rods and instruments during measurement,
- scale errors of levelling rods,
- refraction,
- reconstruction of old positions in repeated levelling.

Most of these errors had been discussed before in detail (MÄLZER 1964, SECKEL 1977). In this paper we shall have a closer look especially to the refraction.

2. Modelling of refraction influences in the levelling methods.

2.1 Refraction study at the ETH/CU-Camp

Refraction is caused by penetrating of light through air layers with different density. The refraction coefficient k is defined as ratio between earth radius (R) and radius of light beam (r)

$$k = R/r \, . \qquad (1)$$

Assuming a symmetrical refraction between both stations (A,B) in a range (S) the efficcient refraction coefficient (k) can be derived from simultaneous reziprocal zenith angles (Z_A, Z_B) by

$$k = 1 * R/S * (200 - Z_A - Z_B) * \pi/200 , \qquad (2)$$

and from one station in combination with known true height difference (Δh_{true}) as

$$k_A = 1 + (S^* \cos Z_A - \Delta h_{true}) * 2R/S^2 . \qquad (3)$$

It is also possible to calculate a local refraction coefficient (κ) by meteorological data, especially by the vertical temperature gradient (dT/dh)

$$\kappa = 501{,}52 . \sin Z . p/T^2 (0{,}034 + dT/dh) \qquad (4)$$

with Z = zenith angle, p = air pressure (hPa), T = absolute temperature (K) .

For investigation of refraction over the Greenland ice surface two campaigns had taken place (1991, 1994) with different weather conditions. The measuring methods and results had been reported in STOBER 1994. Summarizing some important results we find:

- Refraction coefficients -0.1 < k < 1.7, decreasing with the weather conditions sunny with wind, sunny without wind, overcast with wind, overcast without wind.
- Inspite of simultaneous reciprocal zenith angles remaining height errors (range 1 km) < 12 mm. Possible causes are:
  - different temperature gradients in both stations,
  - different temperature gradients due to topography.
- Refraction may be calculated from vertical temperature profiles ($k \approx \kappa$).

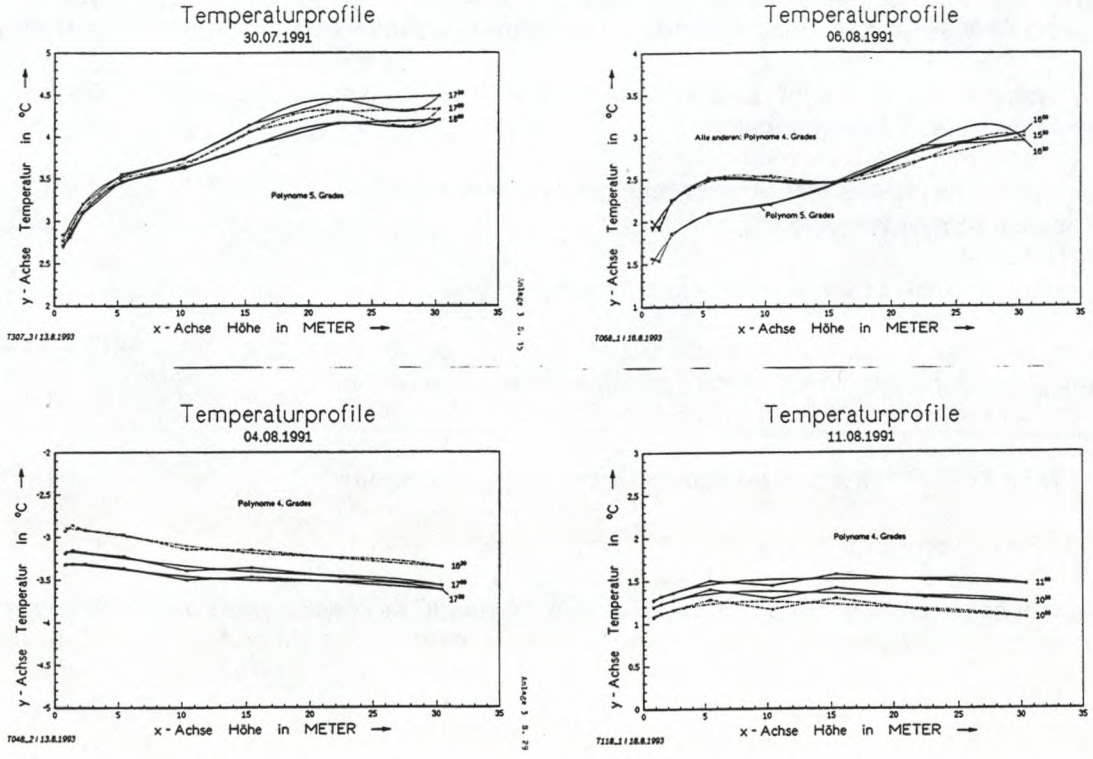

Figure 1: Vertical temperature profiles of 4 typical model atmospheres

For modelling of refraction errors in the EGIG line we have no real measured temperature gradients, but we can substitute those from the experiences got at the ETH/CU-camp. So we choose four typical days representing the four typical types of atmospheric conditions (fig. 1).

Model 1: sunny, with wind, k = 1,53
30.07.91, 17:00 local time

Model 2: overcast, without wind, k = 0,12
04.08.91, 17:00 local time

Model 3: sunny, without wind, k = 1,33
06.08.91, 15:40 local time

Model 4: overcast, with wind, k = 0,54
11.08.91, 10:30 local time

2.2 Modelling local refraction influences in the EGIG-line

The altitudes in the EGIG line in general are slowly increasing from the western margin to the central part with local topographical undulations (amplitudes of some 10 meters, periodes of about 10 km). These undulations can be considered as stationary ones (SECKEL/STOBER 1968). As test area for refraction influences we take the section (430 km) between T1 (altitude 1700 m) and T43 (3300 m), which was digitized from the levelling 1968 every 100 meters. For calculation the local refraction we need the actual ground distance of beam and we apply the model of vertical polygon, using formula (4) for every part of a levelled sight line (SCHMID 1994).

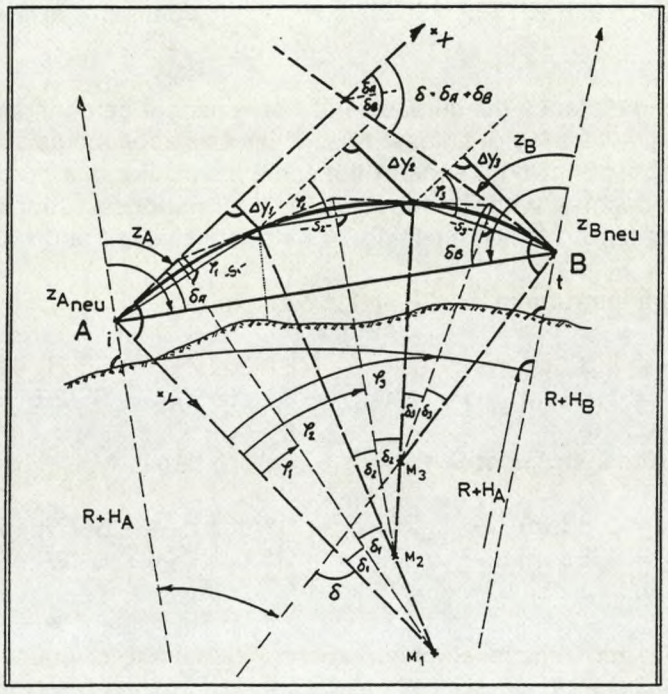

Figure 2: Modelling local refraction effects in levelling by vertical polygon of light beam depending on variable ground distance.

2.3 Refraction influences in the trigonometric levelling

The measuring procedure of the trigonometric levelling (figure 3) was developped by the TU Braunschweig (KOCK 1987, MÖLLER/RITTER 1988). It is working with two simultaneously observing groups (1 theodolite and two targets at each station). According to the polygon model (figure 2) the refraction influences are calculated as y-components in the local coordinate system with origin in the theodolite (figure 4).

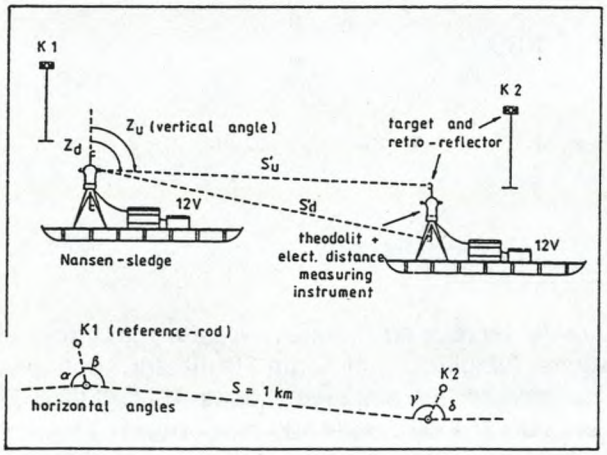

Figure 3: Measuring procedure for the trigonometric levelling (MÖLLER/RITTER 1988).

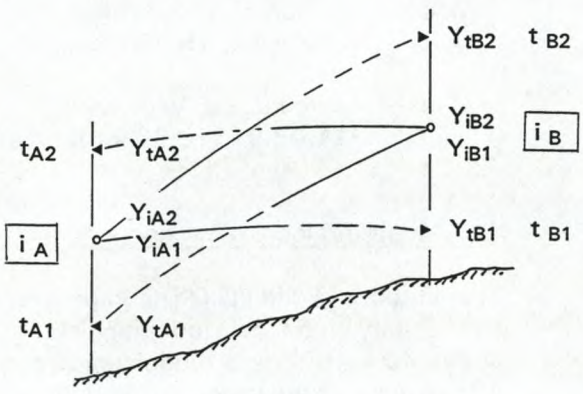

Figure 4: Principle of refraction influences in the trigonometric levelling

Due to variable ground distance the curvature of beam cannot be constant because usually the vertical temperature gradient is not a linear one. A measure for the asymmetry of a beam is the difference of y-components at both ends of the same beam. For this purpose we have to consider forward and backward sights with the formulas for *one-side* observations between two stations (A,B) . When meaning i = instrument height and t = target height, we obtain:

Forward sight: From instrument A (i_A = 1,62 m) to target B

lower target (t_{B1} = 0,83 m) --▸ $\Delta h_{AB1} = S^* \cos Z_{A1} + S^2/2R - y_{tB1}$,
upper target (t_{B2} = 1,83 m) --▸ $\Delta h_{AB2} = S^* \cos Z_{A2} + S^2/2R - y_{tB2}$,

Backward sight: From instrument B (i_B = 1,62 m) to target A

lower target (t_{A1} = 0,83 m) --▸ $\Delta h_{BA1} = S^* \cos Z_{B1} + S^2/2R - y_{tA1}$,
upper target (t_{A2} = 1,83 m) --▸ $\Delta h_{BA2} = S^* \cos Z_{B2} + S^2/2R - y_{tA2}$.

In the general formula for *reciprocal* observations we have to calculate the "*average*" from forward and backward sights algebraically as "*difference*" of the height differences (because of contrary signs)

$\Delta h = (\Delta h_{AB} - \Delta h_{BA})/2$ with $\Delta h_{AB} = S^* \cos Z_A + S^2/2R - y_B$,
$\Delta h_{BA} = S^* \cos Z_B + S^2/2R - y_A$,

and following

$$\Delta h = S^* (\cos Z_A - \cos Z_B)/2 + (y_A - y_B)/2 .$$

As usually only symmetrical refraction is assumed we get the height difference

$$\Delta h = S^* (\cos Z_A - \cos Z_B)/2$$

but in case of unsymmetrical refraction a systematic refraction error (sign: "correction") is remaining

$$v_{\Delta h} = + (y_A - y_B)/2 .$$

Spezialized to the observation procedure of the motorized trigonometric levelling in Greenland we are modelling the refraction corrections (v) due to topography for several model situations:

Influence of asymmetry in **forward** *beams:*

a) from point A to target 1 (lower): $v_a = (y_{iA1} - y_{tB1})/2$ ====▸ diagram GZ1-P.ver

b) from point A to target 2 (upper): $v_b = (y_{iA2} - y_{tB2})/2$ ====▸ diagram GZ2-P.ver

c) average from A to targets 1 and 2

$v_c = (v_a + v_b)/2 = 0.5^*\{(y_{iA1} - y_{tB1})/2 + (y_{iA2} - y_{tB2})/2\}$ ====▸ diagram P12.ver

Influence of asymmetry in **backward** *beams:*

d) from point B to target 1 (lower): $v_d = (y_{iB1} - y_{tA1})/2$ ====▸ diagram GZ1-N.ver

e) from point B to target 2 (upper): $v_e = (y_{iB2} - y_{tA2})/2$ ====▸ diagram GZ2-N.ver

f) average from B to targets 1 and 2

$v_f = (v_d + v_e)/2 = 0.5^*\{(y_{iB1} - y_{tA1})/2 + (y_{iB2} - y_{tA2})/2\}$ ====▸ diagram N12.ver

Influence of **average** *from forward and backward*

g) to target 1 (lower): $v_g = (y_{tA1} - y_{tB1})/2$ ====▸ diagram GZ1-PN.ver

h) to target 2 (upper): $v_h = (y_{tA2} - y_{tB2})/2$ ====▸ diagram GZ2-PN.ver

i) to average from both targets 1 and 2

$v_i = (v_g + v_h)/2 = 0.5^*\{(y_{tA1} - y_{tB1})/2 + (y_{tA2} - y_{tB2})/2\}$ ====▸ diagram PN1_PN2.ver

The accumulated refraction corrections are shown in the diagrams **figure 5.**

The cases a) until f) are only for theoretical interest, because they are not really measured. We only see the asymmetry of beams due to varying ground distance if theodolite and target are not mounted in the same height. In the most unfavourabel case (between instrument and lower target) the error would grow up to 3 meters and for the higher target still we find 30 cm as accumulated asymmetry.

From most practical interest are the cases g) until i), because they are corresponding to the real measuring procedure with reciprocal observations. The remaining systematic refraction errors due to terrain undulations in the trigonometric levelling are very small, in maximum on sunny days between -10 mm and + 27 mm. So height differences from T1 to T43 (430 km) may only be influenced up to about 4 cm.

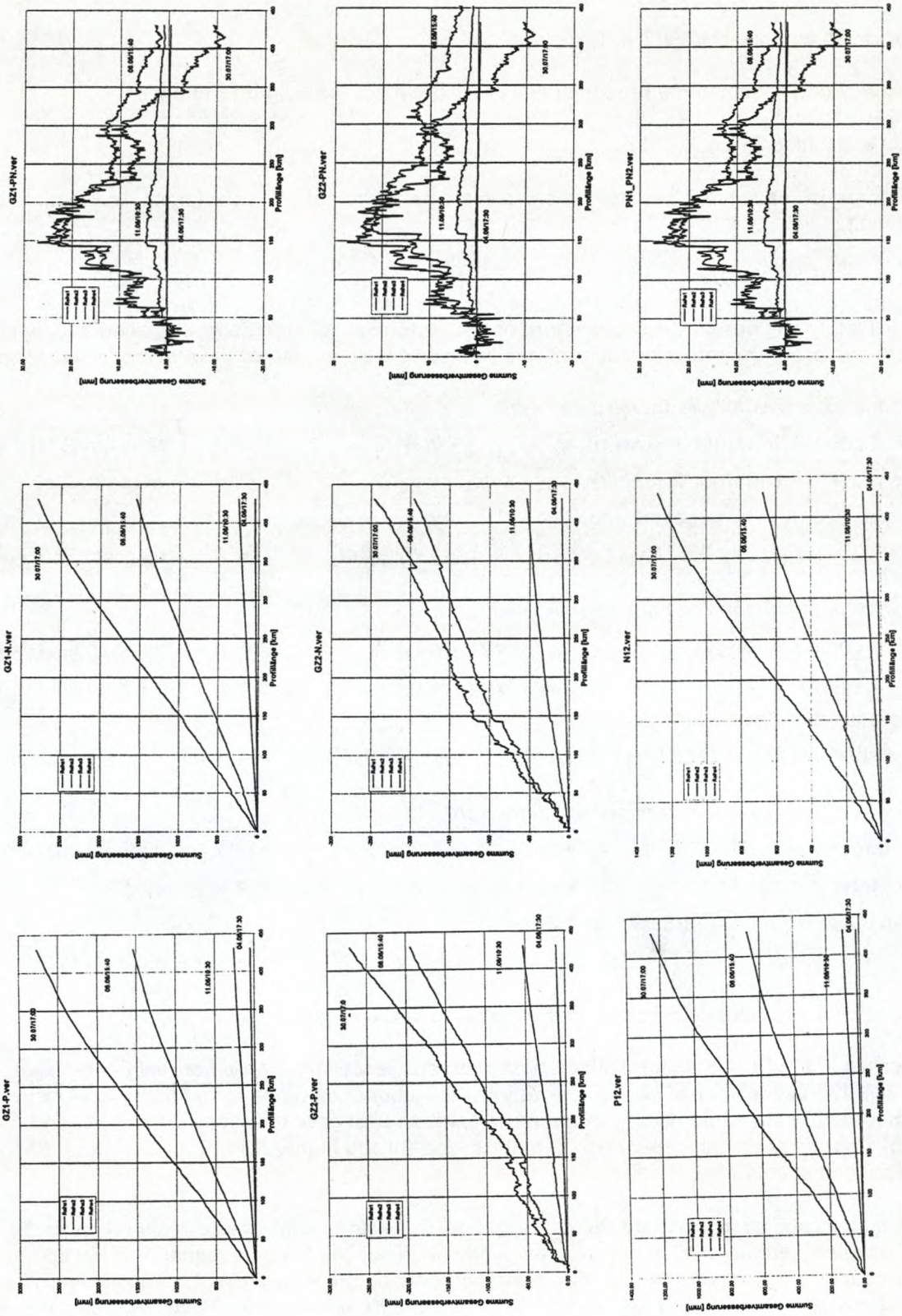

Figure 5: Modelled and accumulated refraction influences in the trigonometric levelling along the EGIG line from T1 to T43

2.4 Refraction influences in the geometric levelling

In the motorized EGIG levellings of 1959 and 1968 a special measuring procedure was applied (MÄLZER 1974). Two instruments measured simultaneously the height difference between the same two rods in a range of about 100 m (figure 6).

The effect of refraction is similar to the trigonometric levelling. We have reciprocal observations, too, but the horizontal forward and backward sights are systematically in different ground distances. The principle of resulting refraction errors are shown in figure 7.

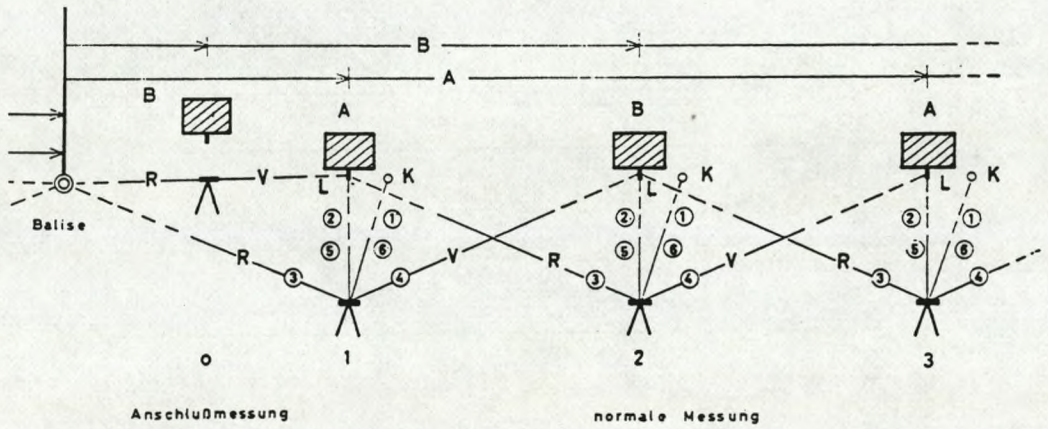

Figure 6: Measuring procedure in the motorized geometric levelling (from: MÄLZER 1974).

The refraction influences can be expressed by the following formulas and the results for the 4 model atmospheres are shown in the plots of figure 8.

Refraction asymmetry in every beam:

j) Forward sight: From point A to target (rod) B:

$v_j = (y_{iA} - y_{tB})/2$ =► diagram 100-P.ver

k) Backward sight: From point B to target (rod) A:

$v_k = (y_{iB} - y_{tA})/2$ =► diagram 100-N.ver

Refraction average forward and backward:

l) $v_l = (y_{tA} - y_{tB})/2$ ==► diagram 100-PN.ver

Figure 7: Principle of refraction influences in the geometric levelling.

The remaining refraction correction of the geometric levelling can be much larger than in the trigonometric levelling, because the forward and backward beams are influenced in a systematically different way corresponding to the general slope from T1 to T43. The largest effect might occur when weather is sunny with wind. In this case we have to consider accumulated refraction influences up to -180 mm. In case of overcast sky the refraction influence will reach only some millimeters.

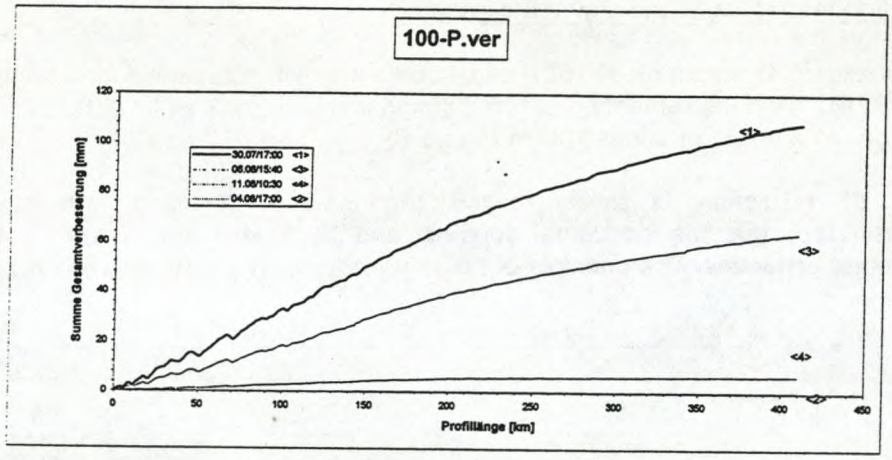

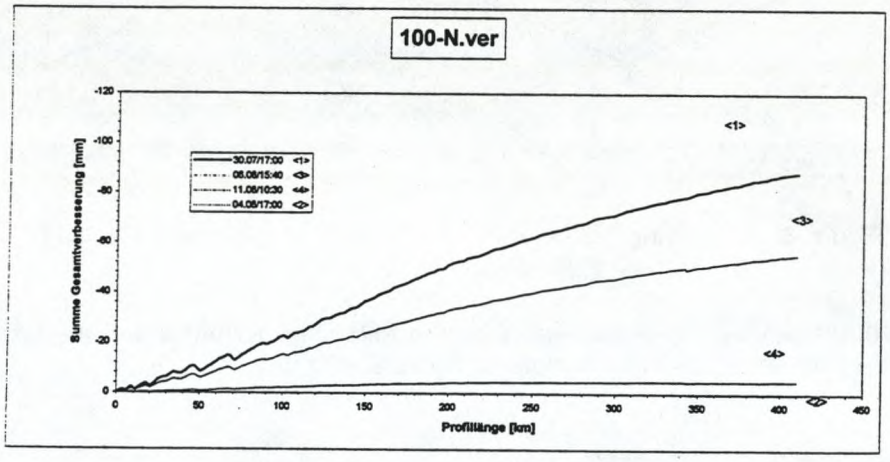

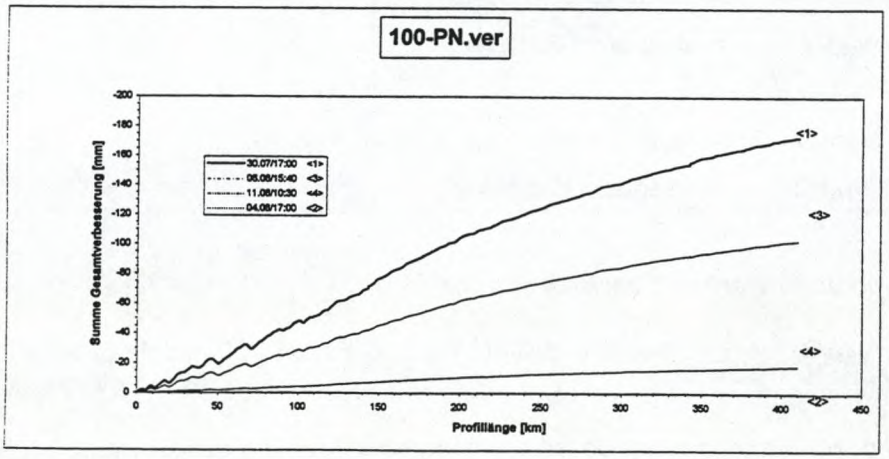

Figure 8: Modelled and accumulated refraction influences in the geometric levelling along the EGIG line from T1 to T43

3. Conclusions

Depending on weather conditions, the refraction coefficient on the Greenland ice surface is varying between -0.1 < k < 1.7 (dayly averages). Representing 4 typical weather conditions, 4 days were chosen with their temperature-height-profiles to calculate the refraction asymmetry in observations of trigonometric and geometric levellings due to local topographic situation. In the test area of the EGIG line (T1 to T43 = 430 km), the resulting possible uneliminated refraction influences in the worst case (sunny, wind) run up to about 40 mm (trig. lev.) and 180 mm (geom. lev.). With these datas we are able to discuss possible errors in the terrestrial height measuring technics used in the EGIG line and the significance of calculated temporal height changes. Therefore we have to summarize the error budget factors for the section T1 - T43 = 430 km:

Accuracy of geometric levelling (N), 1 campaign :

- random measuring errors (max):	62 mm
- sinking of rods, eliminated by procedure:	---
- scale errors of rods, eliminated by calibration:	---
- refraction influences (due to topography).	180 mm
- reconstruction of position:	100 mm

Total standard deviation T1 - T43: $s_{GN} = \pm \sqrt{(62^2 + 180^2 + 100^2)} = \pm 215$ **mm**

Accuracy of trigonometric levelling (T):

Random measuring errors (1 km: $s_{0T} = \pm 8{,}7$ mm):	180 mm
Sinking of instruments: eliminated from procedure:	---
Refraction influences:	
- random different refraction in both points $\Delta k \approx \pm 0{,}1 \rightarrow s_{0T(\Delta k)} = \pm 4$ mm $\rightarrow$ T1 - T43 $\rightarrow s_{gT(\Delta k)}$:	83 mm
- due to topography T1-T43:	40 mm
Influence of positioning:	100 mm

Total standard deviation T1-T43: $s_{GT} = \pm \sqrt{(180^2 + 83^2 + 40^2 + 100^2)} = \pm 226$ **mm**

Significance of height changes between 2 campaigns, (test level 95%; t=1,96):

Between geometric levellings (1959-▸1968)

$\Delta H_{N-N} = 1{,}96 * \sqrt{(215^2 + 215^2)}$ mm = 596 mm ≈ 0,6 m

As the height changes 1959 --▸ 1968 amount to 1,1 m > 0,6 m, they are significant!

Between geometric (G) and trigonometric (T) levellings (1968 --▸1990/92):

$\Delta H_{N-T} = 1{,}96 * \sqrt{(215^2 + 226^2)}$ mm = 608 mm ≈ 0,6 m

As the height changes 1968 --▸ 1990/92 amount to 3,6 m > 0,6 m, they are significant!

So we can conclude that the terrestrial levelling methods are precise enough for deriving temporal height changes of the Greenland ice sheet.

5. References

ANDERSEN, O. B.: ERS-1 altimetry on the Greenland ice sheet: Preliminary investigations of annual variations.
Geophysical Research letters, Vol. 21, No. 15, p. 1655-1658, July 15, 1994.

KOCK, H.: Konzeption eines schnellen motorisierten trigonometrischen Nivellements.
Geodätische Schriftenreihe der TU Braunschweig, Nr. 7, S. 39-45, 1987.

KOCK, H.: Height determination along the EGIG line and in the GRIP area. Mass balance and related topics of the Greenland ice sheet, 3rd workshop dec. 1992, GGU Open File Series 93/5, April 1993.

MÄLZER, H. : Das Nivellement über das Grönländische Inlandeis der Internationalen Glaziologischen Grönland-Expedition 1959. Meddelelser om Grönland, Band 173, Nr.7, (EGIG-Veröff. Bd. 3, Nr. 1), Kopenhagen 1964.

MÖLLER, D. und RITTER B.: Glacial Geodetic contributions to the Mass Balance and Dynamics of Ice Shelves. Annals of Glaciology 11, p. 89-94, 1988.

MÖLLER, D.: Das West-Ost-Profil der Internationalen Glaziologischen Grönlandexpedition (EGIG).- Rekonstruktion und geodätische Neumessung-
GEOwissenschaften, Organ der Alfred-Wegener-Stiftung, H. 3, S. 80-82, März 1994.

OHMURA, A. et al.: ETH Greenland Expedition, Progress Report No. 1,
Department of Geography, ETH Zurich, March 1991.

SCHMID, B. : Numerische Untersuchungen zur Refraktion in Grönland.
Diplomarbeit an der FHT Stuttgart (unveröffentlicht) , 1994.

SECKEL, H. und STOBER, M.: Höhenänderungen des grönländischen Inlandeises 1959-1968.
Polarforschung, Bd. VI, Nr. 1/2, S. 215-221, 1968.

SECKEL, H.: Höhenänderungen im Grönländischen Inlandeis zwischen 1959 und 1968.
Medd. om Gronland, Bd. 187, Nr.4, Kopenhagen 1977.

STOBER, M.: The Geodetic Programme 1990/1991. ETH Greenland Expedition,
Progress Report No. 2, Department of Geography, ETH Zürich, 1992.

STOBER, M.: Investigations about refraction influences in trigonometric levelling on the Greenland ice surface. Report of the 4th workshop on Mass balance and related topics of the Greenland ice sheet. Geological Survey of Greenland, Open File Series 94/13, Copenhagen 1994.

ZWALLY, H.J: Growth of the Greenland Ice Sheet: Measurement/Interpretation.
Science, Vol.246, 1989.

THE GEOID OF GREENLAND - A REFERENCE SURFACE FOR REMOTE SENSING

Rene Forsberg
Geodetic Division, Kort og Matrikelstyrelsen
Rentemestervej 8, DK-2400 Copenhagen NV, Denmark
E-mail: rf@kms.min.dk

Abstract

This paper outlines the current status of the geoid in Greenland. The current best models are based on a mix of data from surface and airborne gravimetry, terrain models of land and ice, and long-wavelength satellite gravity field information.

Introduction

The geoid - the equipotential surface corresponding to average sea-level - is a basic reference surface of geodesy and remote sensing. The geoid height - N - is related to the heights above sea-level (orthometric heights, H) and heights above the reference ellipsoid (h) by

$$N = h - H \tag{1}$$

The ellipsoidal height h is the basic observable from satellite techniques (GPS positioning, satellite altimetry etc.), while H is the basic height obtained in levelling, and the height type required e.g. for glaciological flow models, or for general digital elevation models.

Determination of the geoid is a fundamental geodetic problem, which can be solved in many different ways. In the case of Greenland (and the Nordic area), the geoid models are determined by splitting the model in three parts

$$N = N_1 + N_2 + N_3 \tag{2}$$

where the first part of the model is the long wavelength part, based on a high-degree spherical harmonic expansion of form

$$N_1 = \frac{GM}{R\gamma}\sum_{n=0}^{N}\left(\frac{R}{r}\right)^n\sum_{m=0}^{n}\left(C_{nm}\cos m\lambda + S_{nm}\sin m\lambda\right)P_{nm}(\sin\phi) \tag{3}$$

with coefficients C_{nm} and S_{nm}, complete to degree and order 360 (OSU91A model, cf. Rapp and Pavlis, 1991). The second term N_2 is computed from the gravitational effects of digital terrain models (land surface heights and ice height/thickness models used in the case of Greenland) using rectangular prisms in a geophysical "forward" modelling process, and the third term N_3 modelled by conversion of residual gravity anomalies into geoid effects using

Fourier transform techniques, transforming residual gravity anomalies Δg_3 into geoid by

$$N_3 = \frac{1}{\gamma} \mathcal{F}^{-1}\left[\frac{1}{\sqrt{(k_x^2+k_y^2)}-2/R} \mathcal{F}(\Delta g_3)\right] \qquad (4)$$

where $\mathcal{F}$ is the two-dimensional Fourier transform, and k the wavenumber. The Fourier transform can be made virtually exact on a sphere by the multi-band FFT method. For details of the method, and an early version of the Greenland geoid, see Forsberg and Sideris (1993).

The current Greenland geoid model - GEOID94A

The computation of Greenland geoid models is ongoing, following advances in gravity data and terrain data acquisitions. An ongoing program of gravity measurements, and refinements of the Greenland digital elevation models, is currently being carried out at KMS.

Compared to the situation a few years back, the knowledge of gravity field variations are now much improved in Greenland thanks to a recent US-Danish cooperation project - the *Greenland Gravity Project* - carried out since 1991 (Forsberg, 1994). The goal of this project is to complete the gravity measurement coverage over Greenland, by high-resolution helicopter gravity surveys in the marginal ice-free areas around the coast, and by a now completed airborne gravity survey (Greenland Aerogeophysics Project - GAP) of the entire Greenland area, determining the longer wavelengths of the gravity field variations. The airborne project, carried out by the US Naval Research Laboratory in cooperation with several other US agencies (NAVO, NOAA, DMA) and KMS, is the first successful contiental-scale airborne gravity survey ever carried out (Brozena, 1991).

The Greenland Aerogeophysics Project was flown with a P-3 aircraft in two two-month field seasons 1991-92, resulting in more than 200000 line-km of airborne gravity data, in addition to aeromagnetic data and high-resolution radar elevation data over the ice sheet and land areas. The flight lines cover Greenland and adjoining ocean areas with E-W tracks of spacing 10-30 nm, with a number of N-S and parallel coast tie lines providing data checks and constraints for cross-over adjustments minimizing data errors.

The estimated accuracy of the GAP gravity data is 5 mgal at 20 km resolution (Brozena, pers.comm.; Forsberg and Kenyon, 1994). The impact of these data on the Greenland geoid models has been changes up to 7 m, compared to earlier models based on only a few scattered tracks of gravity data in the interior of Greenland (Forsberg, 1993).

The airborne gravity data has been merged with the surface gravity data in a process based on the optimal estimation method of least-squares collocation, taking into account the analytical downward continuation of airborne data from the flight elevation (4.1 km) to the terrain surface. This processing requires is very computer intensive, and requires the solution of a large number of linear equations in a number of blocks, for details see Forsberg and Kenyon (1994). The outcome of the process is a set of estimated gravity values and standard deviations gridded on a 5' grid.

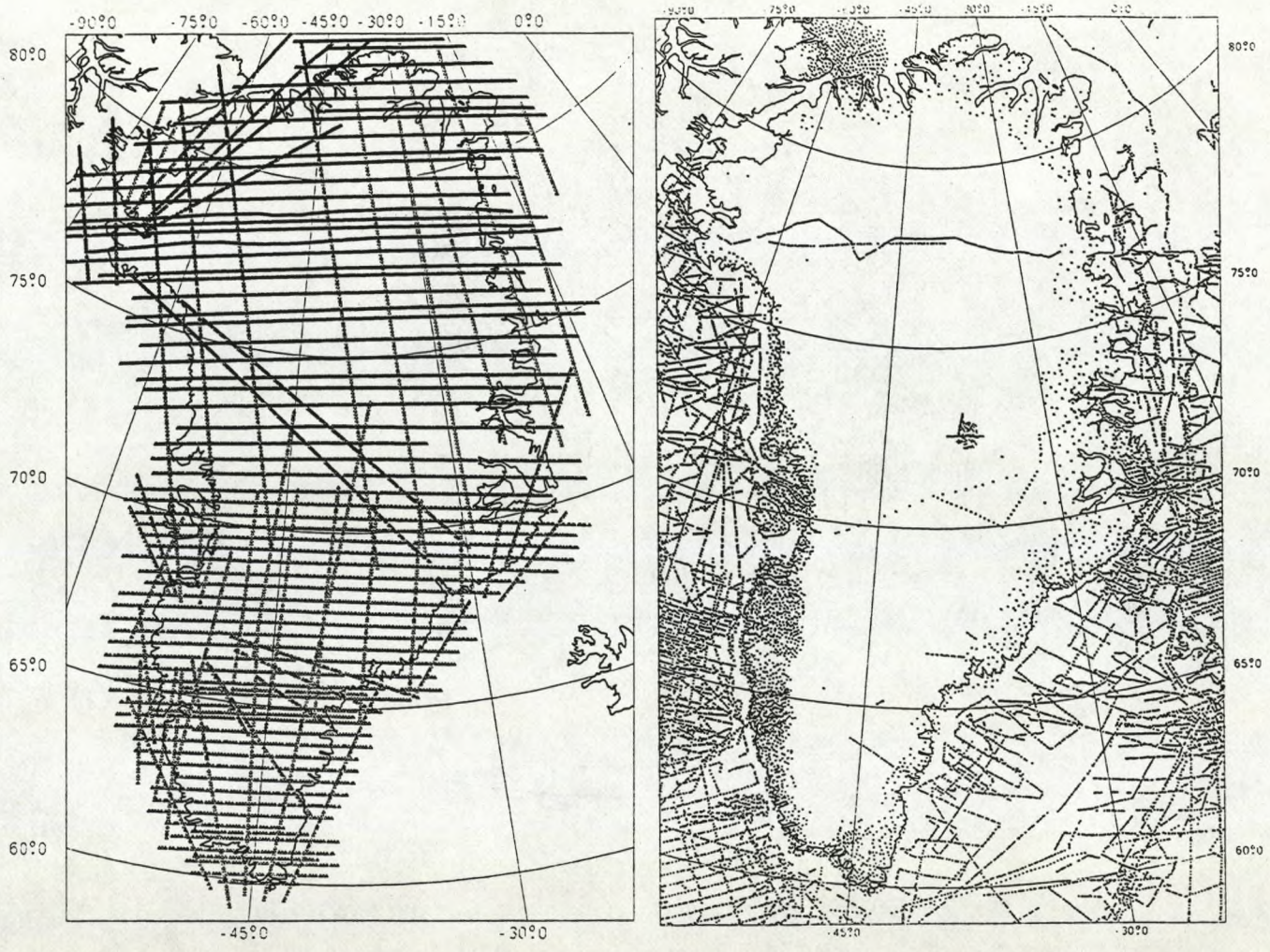

Fig. 1. Gravity data coverage underlying the GEOID94 model. Left: GAP 91-92 airborne data, right: surface gravimetry data (recent newly acquired data in northern Greenland not yet used).

The current available geoid model - GEOID 94A - is based on approximately 24000 surface gravity points, and 32000 selected airborne data points (Fig. 1). These data has been downward continued and merged onto a 5' geographical grid, covering all of Greenland and adjacent ocean areas. Terrain effects were computed from a 5-km resolution terrain models, based on a mix of scanned and manually read maps, and satellite and GAP airborne radar altimetry over the ice sheet (Ekholm, 1995).

The 5' grid was subsequently converted into a geoid effects by spherical FFT (4), using a 512 x 384 zero-padded transform grid, and the terrain and spherical harmonic reference effects restored to yield the final geoid model (Fig. 2). The geoid of Greenland changes from a low value of 10 m north of Thule to 62 m on the east coast. Locally the geoid contours are closely correlated with the local topographic features (Fig. 3).

The final geoid model is available to users as a geographical grid, with supporting interpolation software for enabling e.g. GPS users to easily recover geoid heights at a specific point.

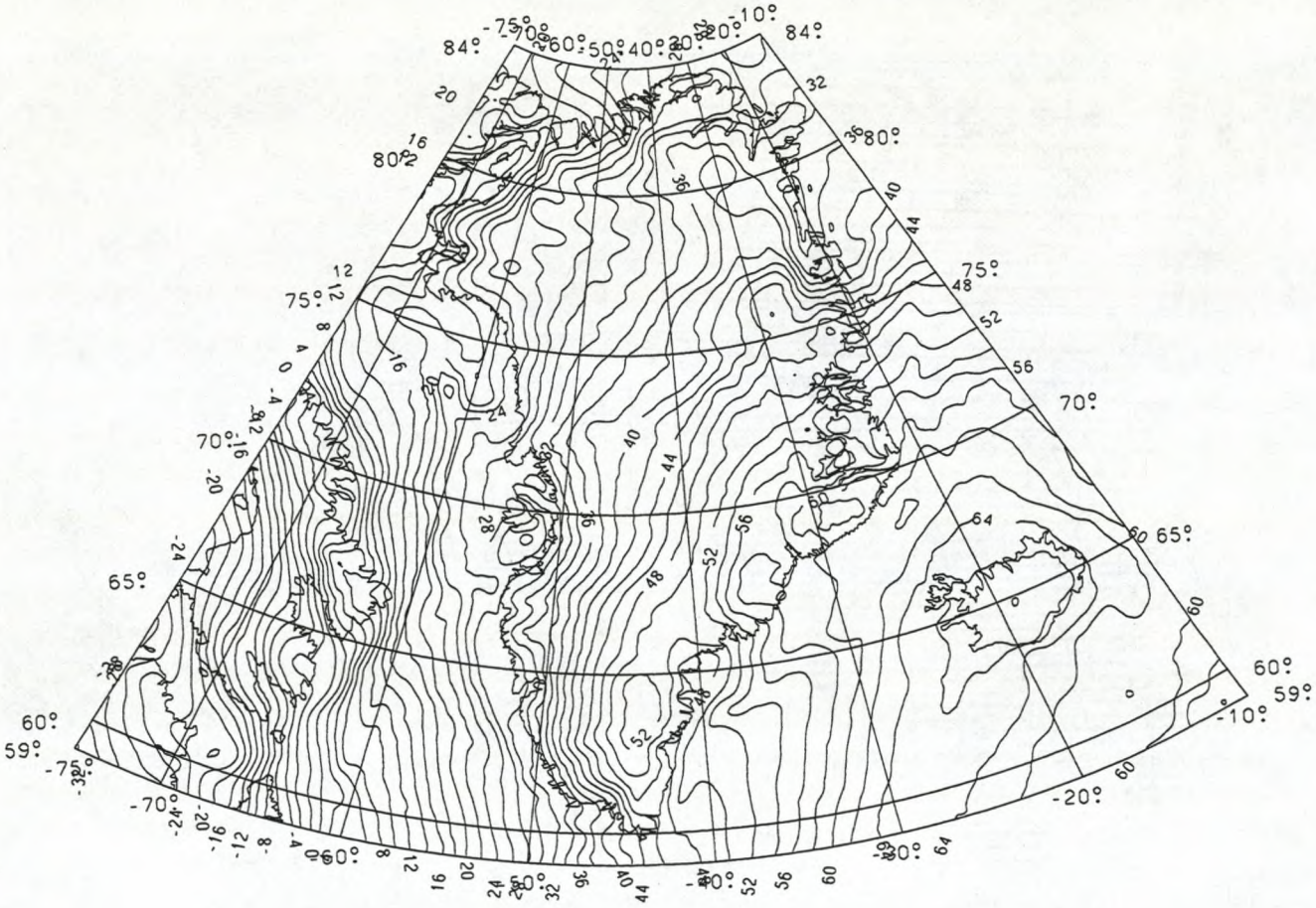

Fig. 2. GEOID94 geoid heights in Greenland. Contour interval 2 m.

The accuracy of the current geoid model is difficult to ascertain, but comparison of GPS surveys to levelled heights along the coastal regions indicate an absolute accuracy around 1 m, with local geoid height difference accuracies at the level of a few dm, dependent on the local roughness of the topography. Combinations of GPS and spirit levelling on the ice sheet in Western Greenland (along part of the NASA profile at 2000 m elevation) supports the local accuracy estimates (Roman, pers. comm.).

Conclusions

This short paper has outlined the background and references for the current Greenland geoid model - GEOID94. Since this model was computed, significant new gravity data has now been surveyed in the Thule area and the Nares Strait region, both on the Greenland and Ellesmere Island sides. Terrain models have also been improved with new high-resolution DEM data from several regions provided by KMS, GGU, and DMA (all of North Greenland is e.g. now covered with 500 m-resolution models). A new geoid model is therefore to be computed within the nearest future.

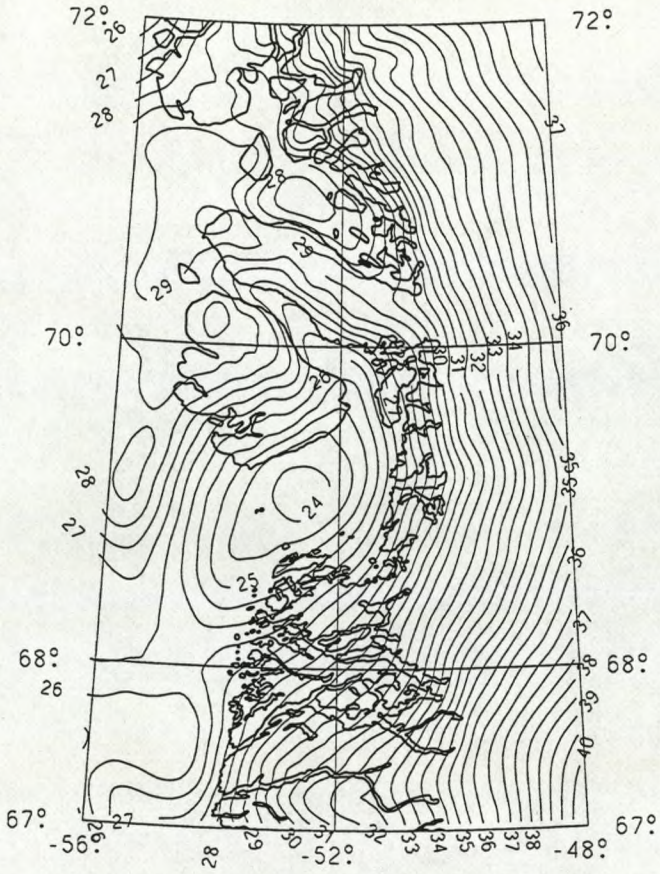

Fig. 3. Example of details of geoid model (Disko area), 0.5 m contour interval.

References

Brozena, J. M.: *The Greenland Aerogeophysics Project: Airborne gravity, topographic and magnetic mapping of an entire continent.* In: O. Colombo (Ed.): From Mars to Greenland, Proc. IAG Symposia 110, Vienna 1991, Springer Verlag 1992, pp. 203-214.

Ekholm, S.: *A full coverage, high-rsolution topographic model of Greenland, computed from a variety of digital elevation data.* Submitted to Journal of Geophysical Research, 1995.

Forsberg, R.: *Impact of airborne gravimetry on geoid determination - the Greenland example.* Bull. International Geoid Service, no. 2, pp. 32-43, Milano, 1993.

Forsberg, R.: *Gravity and GPS measurements in Greenland.* Proc. Nordic Geodetic Commission General Assembly, Ullensvang, Norway, 1994.

Forsberg, R. and S. Kenyon: *Evaluation and downward continuation of airborne gravity data - the Greenland example.* Proc. KIS-94 (Int. Symp. on Kinematic Systems in Geodesy, Geomatics and Navigation), Banff, Canada, Aug-Sep 1994

Forsberg, R. and M. G. Sideris: *Geoid computations by the multi-band spherical FFT approach.* Manuscripta Geodaetica, 18, 82-90, 1993.

Rapp, R.H. and N. Pavlis: *The development and analysis of geopotential coefficient models to spherical harmonic degree 360.* Journal of Geophysical Research, 95, 21885-21911, 1990.

SOME TURBULENCE CHARACTERISTICS IN THE STABLE BOUNDARY LAYER OVER THE GREENLAND ICE SHEET

J. Forrer and M.W. Rotach Swiss Federal Institute of Technology, Zürich

February 29, 1996

1 Introduction

This contribution contains a short discussion of the boundary layer structure, that especially refers to the conditions at the ETH-camp (69° 34' N, 49° 17' W, 1155 m a.s.l.), approximately 80 km from the west coast of Greenland on the inland ice. Compared to a typical mid-latitude nocturnal boundary layer, where most of the investigations concerning the stable boundary layer (SBL) were performed, this site offers some advantages in studying the SBL:

- A continuously stable stratification over prolonged periods.
- An almost ideally homogeneous surface.
- Relatively high wind speed. The mean wind speed for the field season 1991 measured at 2m a.g. was approximately 6m/s.

However, possible problems due to the choice of the site include:

- The possible occurrence of gravity waves and intermittent turbulence during the very stable conditions.
- The dynamics of the katabatic flow.

2 Measurements

The measurements and the data handling were already presented in a previous report (Forrer and Rotach, 1994). Therefore, only a short overview over the measurements is presented. Profiles of mean wind, temperature and specific humidity were measured on a 30m tower at eight levels (0.5,1,2,5,10,15,22,30m a.g.). In addition, three turbulence

units, including a Gill 3d-research probe and a Ly-α hygrometer, provided the fluctuating variables at variable heights. Turbulence runs were selected for analysis, if they could be considered stationary and the statistical uncertainty was less than 20%. Mean values were calculated by applying a running mean to filter low frequency variability.

3 Results

Under homogeneous and stationary conditions the turbulent fluxes of momentum, sensible and latent heat can be calculated within the surface layer from mean profiles using Monin-Obukhov similarity theory:

$$\frac{d\overline{x}}{dz}\frac{kz}{x_*} = \phi_x(z/L) \tag{3.1}$$

where x_* is a scaling variable, ϕ_x is the non-dimensional gradient for variable x and L is the Obukhov length. The ϕ-functions for wind speed (ϕ_m) and temperature (ϕ_h), calculated from the lowest level of turbulence observations (2m a.g.) are presented in Fig. 3.1. This level is sufficiently close to the surface ($\approx$2m a.g.) that it can safely be assumed that all measurements were taken within the surface layer (SL) an thus can be compared to standard SL expressions. The solid curves in Fig. 3.1 represent the linear expressions proposed by Högström (1988), ϕ_m^H and ϕ_h^H. The dashed curves were determined from the integrated forms of the non-dimensional gradients as proposed by Beljaars and Holtslag (1991), ϕ_m^B and ϕ_h^B:

$$\phi_m^H = 1 + 6\frac{z}{L} \tag{3.2}$$

$$\phi_h^H = 0.95 + 7.8\frac{z}{L} \tag{3.3}$$

$$\phi_m^B = 1 + a\frac{z}{L} + b\frac{z}{L}exp(-d\frac{z}{L}) - bd\frac{z}{L}(\frac{z}{L} - \frac{c}{d})exp(-d\frac{z}{L}) \tag{3.4}$$

$$\phi_h^B = 1 + a\frac{z}{L}(1 + \frac{2}{3}a\frac{z}{L}) + b\frac{z}{L}exp(-d\frac{z}{L}) - bd\frac{z}{L}(\frac{z}{L} - \frac{c}{d})exp(-d\frac{z}{L}) \tag{3.5}$$

with a=1, b=0.667, c=5 and d=0.35. In each panel of Fig. 3.1 average values together with the run-to-run variability (indicated by error bars) are given for certain ranges of stability.

For the stability range covered by the measurements, both ϕ_m-expressions give a fair overall fit to the experimental data. Expression (3.4) appears to be superior as stability increases. A linear regression, requiring that $\phi_m(0) = 1$ yields a factor 5.8 (+/- 0.2) which is very close to the value determined by Högström. However, expression (3.2) overestimates the present observations for stronger stability. The same plot for the non-dimensional temperature gradient (ϕ_h) shows much more scatter and there is no indication for ϕ_h to increase with increasing stability as predicted by standard surface layer expressions. The observations close to the surface seem to indicate that ϕ_h remains approximately constant at its near neutral value (or even slightly decreases) over the range $0 < z/L < 0.5$.

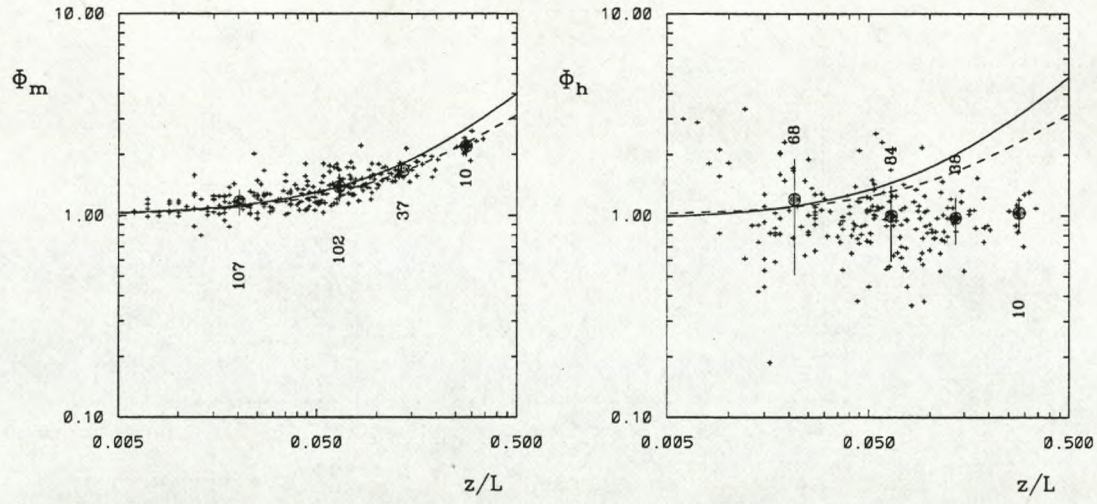

FIGURE 3.1: *Plot of ϕ_m and ϕ_h against z/L in log-log representation for stable stratification calculated from observations at 2 m a.g. The solid curves represent the expressions (3.2) and (3.3), the dashed curves refer to (3.4) and (3.5), respectively. The numbers correspond to the number of observations used to calculated the averages (large symbols) in a given stability range. The error bars indicate the standard deviation of the individual observations.*

Fig. 3.2 shows the averaged measured wind and temperature profile for the runs in which $z/L > 0.1$, i.e., the cases for which the difference between the two ϕ-functions is most pronounced. The stars are averaged observations with error bars indicating the standard deviation of the measurements. For wind speed, the function (3.1) was numerically integrated from 0.5m upwards using equation (3.2) (solid line) and (3.4) (dashed line). For temperature equations (3.3) and (3.5) were used respectively, to determine the profiles. The solid lines represent the so called log-linear profiles. Both calculated wind profiles are in good agreement with the data up to a height of 5-10m. However, under these stable conditions, with an average L of 15m, the log-linear form overestimates the present observations as height increases. It seems, that the surface layer is very shallow (< 10m) and that the surface fluxes are no longer appropriate scaling parameters. At the first sight, the excellent agreement in Fig. 3.2 of the calculated and measured wind profile when using eq.(3.4) contrasts with this finding because (3.4) is formally based on surface layer similarity since it is formulated in terms of the Obukhov length L based on surface fluxes (and not on its local counterpart, Λ). However, according to Beljaars and Holtslag (1991), the relationship between the local fluxes and the surface fluxes is incorporated in (3.4). Fig. 3.2 confirms the success of this approach on the basis of the present data.

In contrast to the profile of mean wind speed, the average temperature profile shows no log-linear region at all and both calculated profiles, overestimate the present observations even close to the surface (Fig. 3.2 right panel). The measured temperature profile exhibits a three-layer structure, with a near-neutral layer close to the ground, an almost logarith-

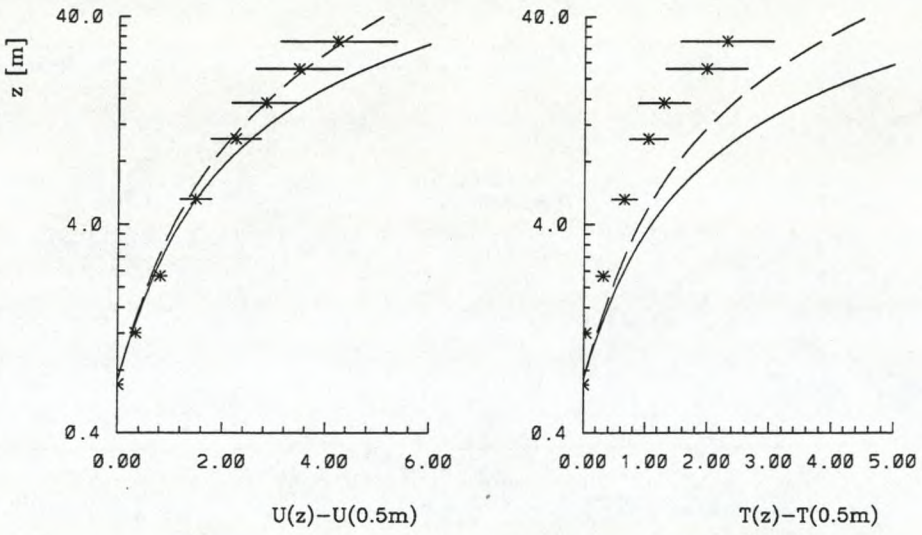

FIGURE 3.2: *The wind and temperature profiles determined numerically using eq.(3.1) and equations (3.4), (3.5) (dashed line) or (3.2), (3.3) (solid line) in comparison with the data (stars) for all the runs with* $z/L > 0.1$.

mic profile (indicated by a constant slope in the semi logarithmic presentation) up to $z \approx$ 15m and a more stable layer above.

Fig. 3.2 implies that the SL is probably lower than 10m under strongly stable conditions. In order to include all the available turbulence measurements into the analysis the data were therefore analyzed in terms of both, surface layer scaling and local scaling (Nieuwstadt, 1984).

Fig. 3.3 shows the ϕ_m-values as one example of the results in terms of both scaling approaches (left panel: SL-scaling right panel: local-scaling), where Λ is the local Obukhov length. The data from each measurement level (indicated by different symbols) are averaged over intervals of stability and only these averages are displayed (together with a typical run-to-run variability for each height, indicated by a vertical line). Note, that this way to present the data reflects the preliminary state of the analysis, in so far as the proper scaling approach would require the observations from different levels to become indistinguishable. Inspecting the right panel of Fig. 3.3, it becomes clear, that the average over the observations from all measurement heights would lead to an almost perfect correspondence between data and the dashed line (eq.3.4), while the observations at, e.g., the 30m and 10m levels exhibit a quite different behavior. In general the data expressed in the framework of local scaling have a smaller run-to-run variability for the individual stability ranges. Furthermore, the tendency with z/Λ seems to be smoother and corresponds better to (3.4) Clearly, both scaling approaches show ϕ_m to level off at large stability where expression (3.4) fits the data much better than (3.2). The linear form (3.2) is in good agreement with the observations for $z/L < 0.4$ (or $z/\Lambda < 0.4$, respectively).

It is concluded that at least some of the runs were performed under conditions such that the

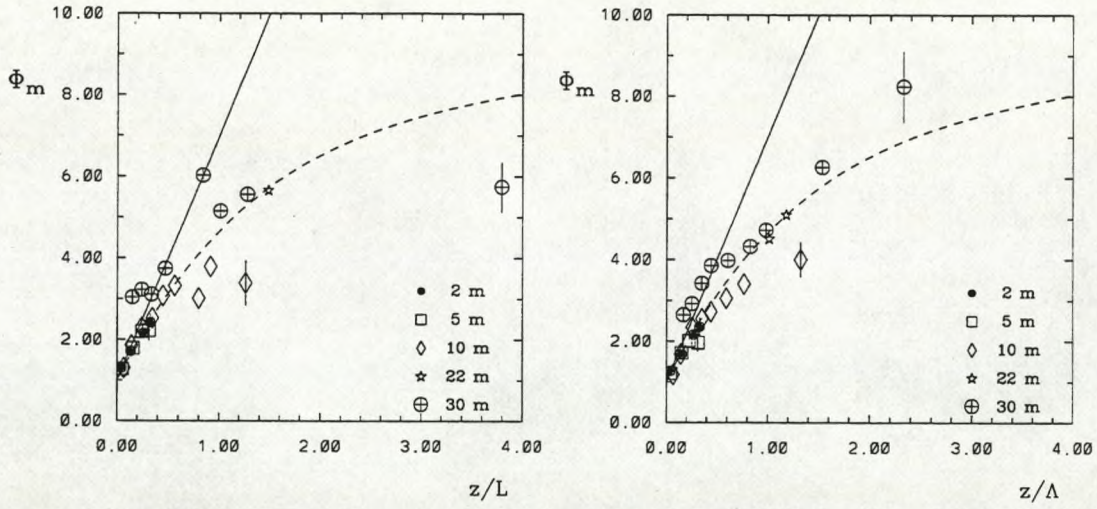

FIGURE 3.3: *Plot for ϕ_m against z/L (left panel) and z/Λ (right panel). The different symbols represent different measurement heights.*

surface layer height was smaller than 30m and the upper levels of turbulent measurements were above the SL. However the best correspondence to the data can be achieved when using the expression of Beljaars and Holtslag (1991) on the basis of local scaling, i.e., by substituting the local Obukhov length Λ for L in eq. (3.4). It should be noted, that these conclusions are drawn from data, that were obtained under conditions of predominant katabatic winds.

References

Beljaars, A. and Holtslag, A. (1991). Flux parameterization over land surfaces for atmospheric models. *J. Appl. Meteo.*, **30**, 327–341.

Forrer, J. and Rotach, M. (1994). Exchange of heat and momentum in a very stable boundary. In *Mass balance and releated topics of the Greenland ice sheet. Report of the 4th workshop*, volume 94/13 of *Open File Ser. Grønlands Geol. Unders.*

Högström, U. (1988). Non-dimensional wind and temperature profiles in the atmosphere surface layer: a re-evaluation. *Boundary-Layer Meteo.*, **42**, 55–78.

Nieuwstadt, F. (1984). The turbulence structure of the stable nocturnal boundary layer. *J.Atmos.Sci.*, pages 2202–2216.

KATABATIC WIND SYSTEMS OVER POLAR ICE SHEETS

Günther Heinemann, Meteorologisches Institut der Universität Bonn
Auf dem Hügel 20, D 53121 Bonn, FRG

1. Introduction

The katabatic wind system represents a key factor for the near-surface wind field of the Antarctic region and Greenland. Coastal zones in both regions reveal a strong topographic gradient and are associated with a wind regime dominated by katabatic forcing with wind speeds up to gale force (Ball, 1960; Wendler, 1990; Putnins, 1970). Strong winds with high temporal constancy are generally observed to be associated with confluence zones due to topographic structures (Schwerdtfeger, 1984). The goal of this paper is to investigate the 3D structure of the katabatic wind generated over the sloped ice surfaces and its transition when passing over the coast-line. For this purpose, different atmospheric situations and boundary conditions are investigated by idealized numerical simulations. This kind of simulations using idealized simulations with 3D meso-scale models under highly simpified boundary values for situations of an atmosphere being initially at rest is similar to the work presented by Bromwich und Du (1995) for Greenland and Parish (1992) and Bromwich et al. (1994) for the Antarctic.

The limited area model (LAM) used for this study is the operational DNMI (The Norwegian Meteorological Institute, Oslo) LAM (Grønås et al., 1987), which was adapted to the Antarctic region (Engels and Heinemann, 1996). The model is run with 121x97 horizontal grid points and 30 vertical sigma levels (about half of the sigma levels are located below 850 hPa, in order to achieve a high resolution of boundary layer phenomena). As with forecast runs in a nested mode, a first run is made for a 50 km grid (LAM50). The initial state is an atmosphere at rest with horizontally homogeneous fields of temperature and humidity. Vertical profiles of potential temperature are chosen being stably-stratified with a near-surface air temperature of 255 K, the profile of the relative humidity reveals a simple three-layered structure (see Heinemann, 1996a, for details) For the 25 km run (LAM25), forecasts of LAM50 are taken as initial fields (6 h forecast) and boundary conditions during the simulation.

2. Results

Antarctic (Weddell Sea region)

Fig.1 shows results for a simulation with complete sea ice coverage (WI case) for the subsection of LAM25 of the eastern Weddell Sea. The wind vector field after 24 h simulation time is displayed for the lowest sigma level (30 m above the surface, wind vectors every gridpoint, i.e. every 25 km). At that time the near-surface katabatic wind system has reached a quasi-stationary state. The turning of the wind direction to the left (relative to the gradient of the topography) clearly reflects the influence of the Coriolis force. Highest wind speeds (up to 14 m/s) are present over regions with increased gradients of the topography as well as in areas, where the katabatic flow is channeled due to topographic structures. In these areas of relatively strong katabatic winds turbulent surface fluxes of sensible heat (H_o) of about -30 W/m^2 are observed, resulting in an additional cooling by the vertical divergence of the sensible heat flux. Since no katabatic forcing due to topographic gradients is present over the sea ice, wind speeds decrease inside a narrow zone over the sea ice close to the coast-line.

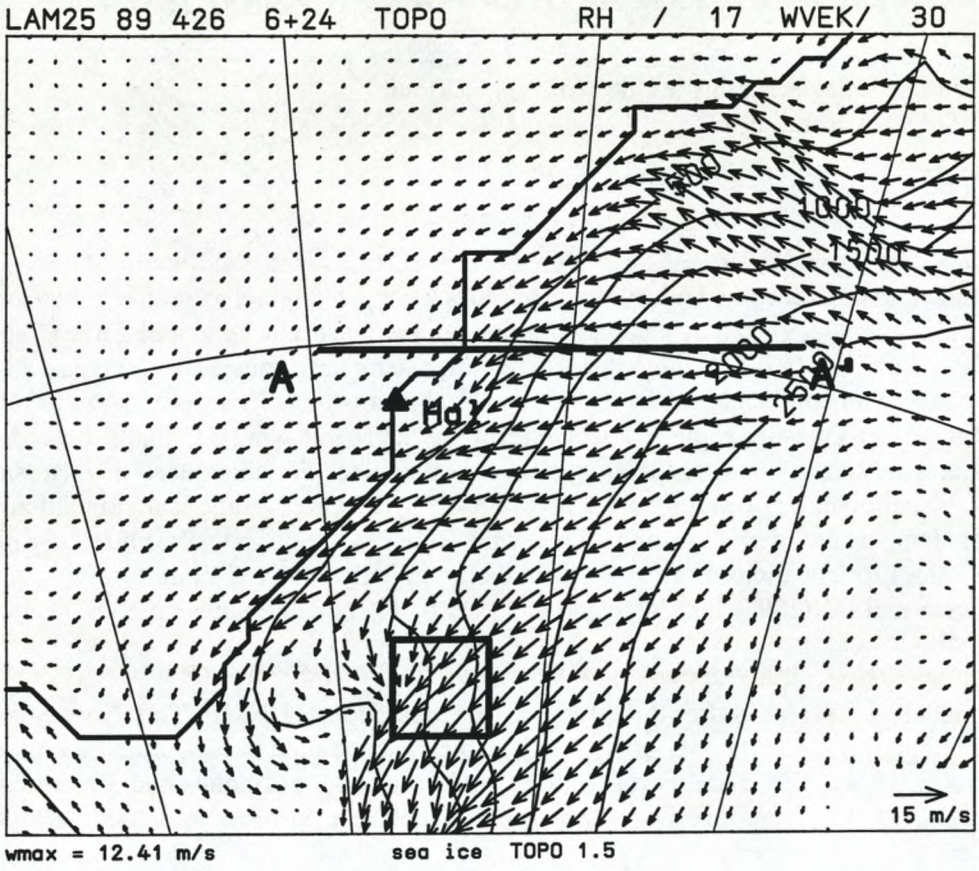

Fig.1: Topography (full lines, isolines every 500 m) and wind vectors at the lowest sigma level for a subarea of the 25 km domain after 24 h. A scaling vector is shown in the lower right corner. The triangle marks the station Halley (Hal), the cross-section A-A' is marked (see text).

Fig.2 shows tangential wind vectors and the potential temperature after 24 h simulation for the cross-section A-A' (approximately from west to east north of the station Halley, marked in Fig.1) and give insight into the vertical structure of the katabatic wind system. The katabatic flow over the continental slope is observed in strong stably-stratified conditions and is confined to the lowest 300 m above the surface. Tangential winds are small close to the coast-line, where the wind decreases and turns to directions parallel to the coast (Fig.1). Since there is no synoptic-scale forcing in this simulation, wind speeds are small at levels above the boundary layer.

A simulation with no sea ice coverage (WNI case) was performed in order to demonstrate the forcing of the baroclinicity in the coastal area caused by the air-sea interaction processes. From observations (e.g. Pettré et al., 1993) it is known that the horizontal differences of the surface energy fluxes result in a distinct forcing of the wind speed in the coastal areas of the Antarctic continent. The effects of the additional forcing resulting from the presence of the open water on the three-dimensional structure of the wind field are evident in Fig.3, which again shows the tangential wind vectors and the potential temperature after 24 h simulation for the cross-section A-A'. As for the WI case, the shallow katabatic wind regime can be seen over the continental slope. In contrast to Fig.2, a pronounced secondary circulation is present close to the coast. Upward wind velocities of about 3 cm/s are simulated above the low-level convergence zone over the water, which is associated with a cloud band of about 1 km thickness. Whereas in the WI case stable stratification is present over the sea ice, well-mixed conditions over the open water can be found in the lowest 1 km for the WNI case.

Greenland

The boundary conditions for the idealized simulation for Greenland correspond to those of March/April 1989. In contrast to the previous cases, a more realistic sea ice distribution was chosen

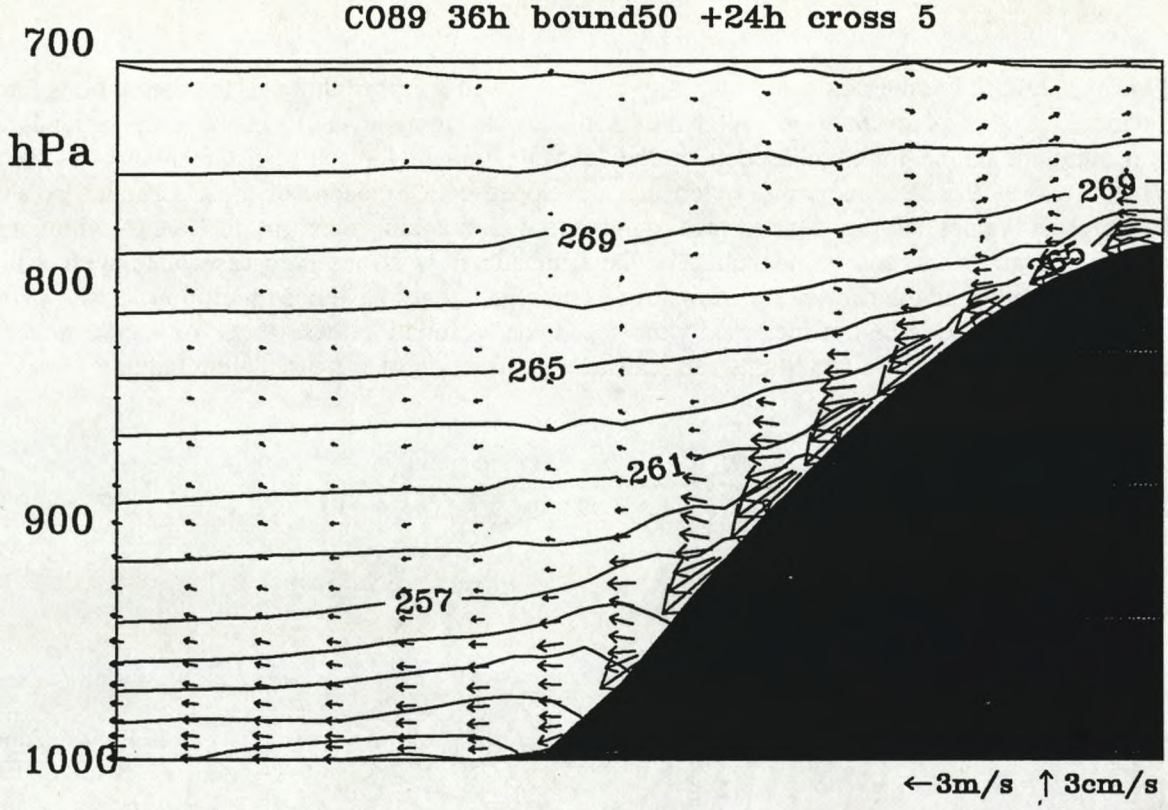

Fig.2: Cross-section for the potential temperature (solid isolines every 2 K) and tangential wind vectors (at a horizontal distance of 25 km) along line A-A' (see Fig.1, pressure in hPa) for the WI case after 24 h simulation time.

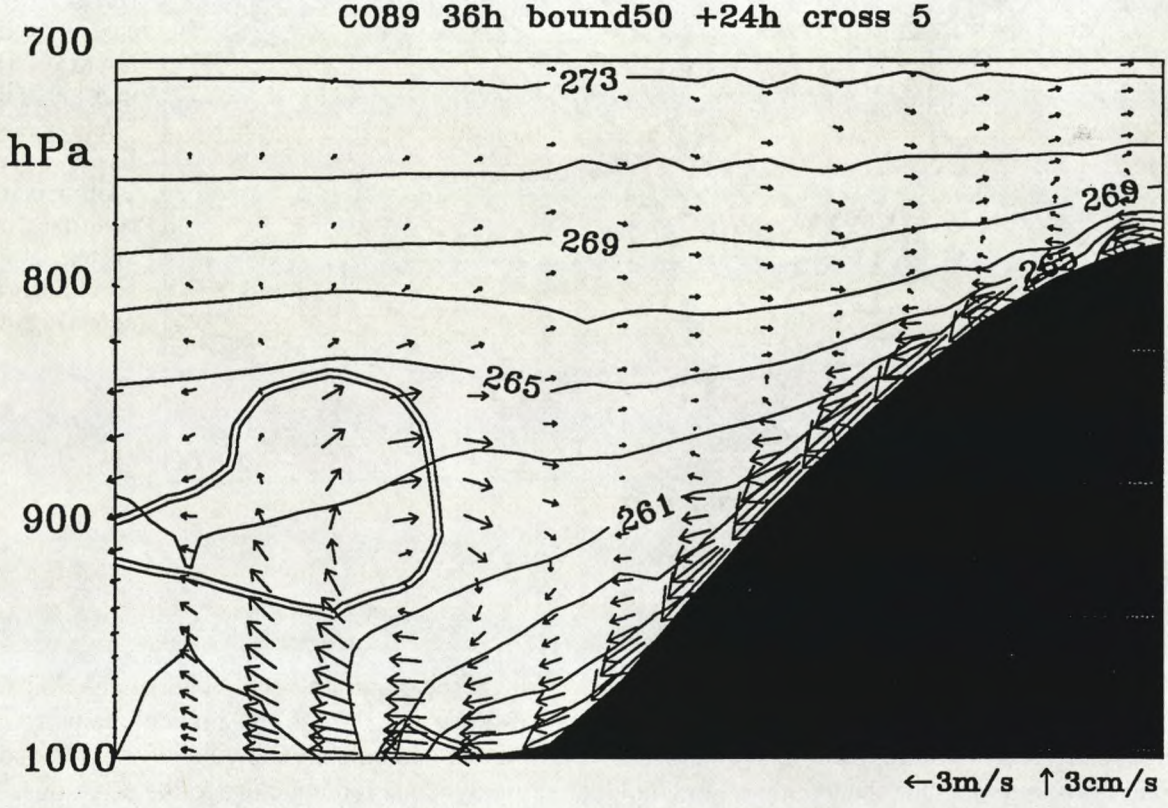

Fig.3: As Fig.2, but for the WNI case. The maximum of the relative humidity is indicated by the 90 % isoline (double line).

(Fig.4). The initial temperature and humidity profiles are identical to those of the simulations for the Antarctic. Fig.4 displays the wind vector field at the lowest sigma-level (30 m above the ground) after 24 h simulation time for a subsection of the LAM50 domain for southern Greenland. As for the WI/WNI cases, the katabatic wind system has developed over the slope of the Greenland ice sheet. The highest values of the near-surface wind speed are again found in the areas with largest topographic gradients, and a channeling of the katabatic flow is observed associated with valleys. Close to the coast and at the sea ice front strong baroclinic zones have been built up (not shown) and -as in the WNI case- a belt of increased wind speed can be found in these areas. As demonstrated by Heinemann (1996b), these conditions can lead to the formation of meso-scale circulations.

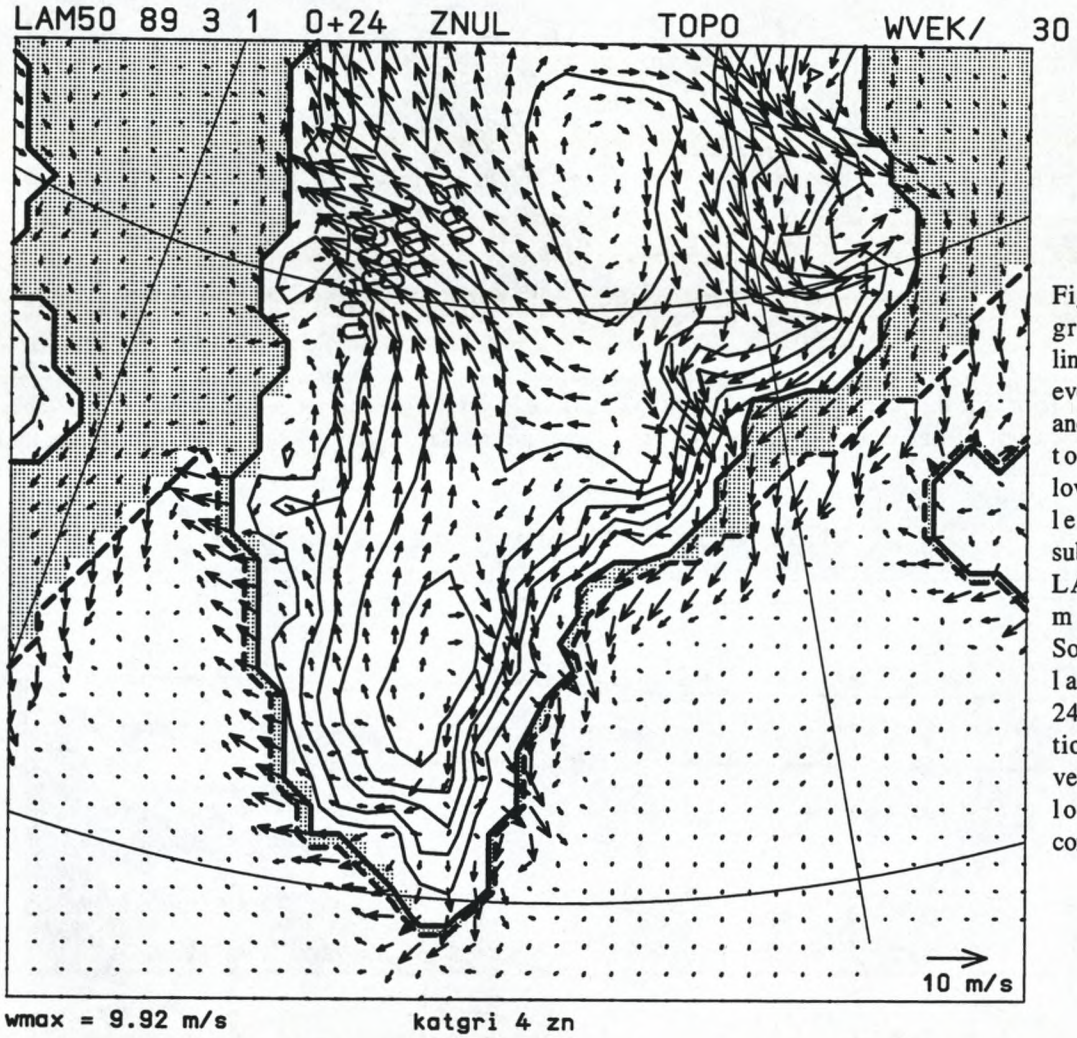

Fig.4: Topography (full lines, isolines every 500 m) and wind vectors at the lowest sigma level for a subarea of the LAM50 domain for South Greenland after 24 h simulation (scaling vector in the lower right corner).

3. Summary

The katabatic wind system represents a key factor for the near-surface wind field of the Antarctic region and Greenland. Idealized simulations with a three-dimensional meso-scale model are performed to investigate the development of the katabatic wind system and its sensitivity to physical boundary conditions, in particular channeling effects and the thermodynamic forcing close to the coast-line. The simulated cases represent wintertime cases with complete sea ice coverage and no sea ice (for the Antarctic) as well as a realistic wintertime situation for Greenland. The near-surface katabatic wind

system is simulated with highest wind speeds over regions with increased gradients of the topography as well as in areas, where the katabatic flow is channeled due to topographic structures. For the Antarctic situations, a large impact of the presence of open water on the three-dimensional structure of the wind field close to the coast can be shown, whereas the effects on the katabatic wind over the sloped ice sheet are relatively small.

Acknowledgements
This research was supported by the "Deutsche Forschungsgemeinschaft" under grant Kr228/16. The author thanks Norwegian Meteorological Institute (Oslo) for their support.

References

Ball, F.K., 1960: Winds on the ice slopes of Antarctica. *Antarctic Meteorology, Proceedings of the Symposium,* Pergamon Press, 9-16.

Bromwich, D.H., Du, Y., Parish, T.R., 1994: Numerical simulation of winter katabatic winds from West Antarctica crossing Siple Coast and the Ross Ice Shelf. *Mon. Wea. Rev. 122,* 1417-1435.

Bromwich, D.H., Du, Y., 1995: Wintertime surface winds over the Greenland ice sheet. *submitted to Mon. Wea. Rev.*

Engels, R., Heinemann, G., 1996: Three dimensional structures of summertime Antarctic meso-scale cyclones: Part II: Numerical simulations with a limited area model. *Global Atmosphere-Ocean System* 4, in print.

Grønås, S., Foss, A., Lystad, M., 1987: Numerical simulations of the polar lows in the Norwegian Sea. Tellus 39A, 334-353.

Heinemann, G., 1996a: Idealized simulations of the Antarctic katabatic wind system with a three-dimensional meso-scale model. In review by *J. of Geophys. Res.*

Heinemann, G., 1996b: On the development of wintertime meso-scale cyclones near the sea ice front in the Arctic and Antarctic. *Global Atmosphere-Ocean System* 4, in print.

Parish, T.R., 1992: On the interaction between Antarctic katabatic winds and tropospheric motions in high southern latitudes. *Aust. Met. Mag. 40,* 149-167.

Pettré, P., Payan, C., Parish, T.R., 1993: Interaction of katabatic flow with local thermal effects in a coastal region of Adelie Land, East Antarctica. *J. Geophys. Res. 98,* 10429-10440.

Putnins, P., 1970: The climate of Greenland. In: *Climates of the polar regions (Ed. S. Orvig), World Survey of Climatology 14,* 3-113.

Schwerdtfeger, W., 1984: Weather and climate of the Antarctic. Elsevier Science Publishers, 261pp.

Wendler, G., 1990: Strong gravity flow observed along the slope of eastern Antarctica. *Meteorol. Atmos. Phys. 43,* 127-135.

ON A FOEHN EVENT AT THE WESTERN MARGIN OF THE GREENLAND ICE SHEET

Friedrich Obleitner
Institut für Meteorologie und Geophysik, Universität Innsbruck

1. Introduction

Commonly „Foehn" is referred to as mesoscale meteorological phenomena occuring at the leeside of mountain ranges. Amongst the associated meteorological features are above all relatively clear skies (Ac. lent. in case), exceptionally high downslope velocities, high temperatures and low relative humidities of the air descending. In that sense it is known to occur wherever a major barrier is to be surpassed by synoptic scale air flow (Alps, Rocky Mountains, Caucasus...). But as expected, individual meteorological effects are highly dependent on regional topography and the relative constallation of the synoptic forcing resp., yielding a broad spectrum of relevant observations.
Early and impressive descriptions of „Foehn" events in Greenland were summarized e.g. by Putins (1970). Within recent literature less attention seemed to be given to Greenland Foehn events, whereas Foehn is still a major aspect of ongoing research within mesoscale alpine meteorology (e.g.Seibert 1990). This contribution is meant to document resp. analyse some aspects of a Greenland Foehn event by making use of alpine experience which hopefully stimulates further work on this subject too.

2. Observations

The following case study refers to observations within an ISLSCP project where measurements of the energy budget of dry Tundra at Isungua (67°N, 50°W, 480m a.s.l., 4km west of ice margin) were performed during summer 1988. Judging by climatology (Tab.1), Foehn events revealed themselves firstly by exceptional high temperatures despite of considerable cloudiness.

		global radiation (Wm^{-2})	temperature (°C)	vapour pressure (hPa)	wind speed (m/s)
5	19 1988	312.0	1.8 | 5.5	3.7 | 4.4	3.0 | 6.4
5	20 1988	331.1	3.0 | 7.2	3.9 | 4.3	3.8 | 5.8
5	21 1988	313.1	3.0 | 6.8	4.9 | 5.8	3.8 | 7.1
5	22 1988	303.9	4.8 | 8.5	4.8 | 5.9	3.4 | 6.1
5	23 1988	328.3	7.3 | 11.9	4.7 | 6.4	5.2 | 9.7
5	24 1988	309.6	8.7 | 13.0	5.0 | 6.7	4.6 | 9.9
5	25 1988	275.8	10.9 | 13.7	5.6 | 6.4	5.6 | 9.3
5	26 1988	290.9	7.0 | 12.2	5.1 | 6.9	4.4 | 9.9
5	27 1988	297.6	5.7 | 10.9	5.6 | 6.9	2.7 | 6.1
5	28 1988	276.1	5.5 | 9.2	5.4 | 7.1	3.0 | 7.2
5	29 1988	314.4	5.9 | 8.8	5.2 | 6.2	4.2 | 6.3
5	30 1988	330.1	7.8 | 11.5	5.2 | 6.0	4.0 | 6.5
5	31 1988	259.8	4.7 | 10.7	5.5 | 6.2	2.3 | 4.6
6	1 1988	314.4	5.5 | 9.7	5.4 | 6.7	3.7 | 5.4
6	2 1988	269.0	5.0 | 8.0	5.4 | 6.1	3.1 | 5.6
6	3 1988	137.2	4.0 | 7.8	5.3 | 6.5	3.1 | 5.8
6	4 1988	172.0	1.0 | 3.2	5.8 | 6.7	2.7 | 6.1
6	5 1988	183.3	1.9 | 4.6	4.5 | 5.5	2.6 | 4.3
6	6 1988	151.1	2.1 | 4.5	5.4 | 6.8	4.3 | 7.9
6	7 1988	294.4	5.3 | 10.0	3.7 | 6.1	3.8 | 6.4
6	8 1988	232.1	8.8 | 11.8	6.5 | 7.5	3.7 | 5.6
6	9 1988	167.2	9.8 | 18.5	7.3 | 9.0	4.5 | 9.9
6	10 1988	219.9	6.9 | 10.0	6.7 | 8.8	3.4 | 5.4
6	11 1988	230.4	8.2 | 11.6	5.6 | 6.4	4.6 | 9.2
6	12 1988	115.8	6.3 | 10.8	6.8 | 8.6	3.3 | 8.6

Tab. 1: Daily mean | maximum values of meteorological parameters as observed at Isungua

Thus the absolute maximum temperature was observed to be about 18°C during a day with Foehn (June 9), which should be compared with about 11°C typical for a clear day just 1 week earlier (May 30).
Maximum wind speeds reached about 10m/s which significantly stand out against the average too. Though still coming down the ice, these Foehn winds were clearly found to occur from a more southeasterly direction than the usual katabatic winds. The typical gustiness of wind direction and speed was observed additionally. Vapour pressure increased due to advection of corresponding air masses, whereas relative humidity significantly decreased below 50% as commonly associated with Foehn. Cloudiness was considerable (8/10), preferrably as Ci. and Ac. lent. and Fc., which initially were arranged in wave like streets of SW-NE orientation, tending to „chaotic sky" later on.
Generally air pressure decreased during the Foehn phases, whereas it recovered with the passage of a cold front which terminated the Foehn at the same time.
Concerning the energy budget of the Tundra near the ice margin, an overall decrease of turnover of energy seems to be noteable during mature Foehn, i.e. a relatively low radiation budget was accompanied by decreased turbulent fluxes of sensible and latent heat.

Within the observational period at Isungua (May 19 to June 13, 1988), 2 days were clearly dominated by the occurence Foehn, though some less developed intermediate Foehn phases were observed on 2 additional days too. The following analysis focusses on the most pronounced event during June 9, 1988.

3. Synoptic analysis

is based on routine meteorological observations within the area of interest, i.e. primary information is available at the 850, 700, 500, 300hpa level (00UTC) and at the surface (00/12UTC) respectively. Most relevant information comes from rawinsoundings at Ivigtut, Agmagssalik, Umanak and Thule, whereas information above the ice is generally sparse.
Concerning the Foehn event during June 9, 1988 the following could be shortly summarized:
at the *upper level* (500hPa) a low pressure system moves into the southern Davies Street which progressively induced a southeasterly air flow from the southeastern coast of Greenland across the ice sheet towards the mid-western coast (Isungua). At the same time warm air swept the eastern slopes of the Greenland Ice towards northeast, which was followed by a body of cold air approaching Cape Farvel. Upper level southeasterly flow remained throughout the Foehn period.
At the *surface level* the synoptic development in southern Greenland was governed by a frontal system crossing the ice sheet towards northwest as the center of the corresponding depression moves towards Baffin Bay.
Summarizing the breakthrough of Foehn in Isungua was clearly associated with increasing pressure gradients (mainly due to advection of cold air in the south) and southeasterly flow across the southern ice sheet at all levels. Breakdown coincides with the passage of the cold front.

4. Thermodynamics

During the discussed event the air arriving at Isungua was obviously crossing the southern ice sheet in a SE-NW direction. Thus the TEMP at Ivigtut might be fairly representative of the thermo-dynamical state of the air mass arriving Greenland from the southern seas. The corresponding thermodynamical diagram (Fig.1) reveals moist adiabatic lapse rates up to about 700 hPa (which roughly corresponds to regional crest height of the ice sheet) and more stable air aloft.
This indicates intense lifting of stably stratified and relatively cold air masses which were forced to ascend the southern margin of the Greenland Ice Sheet by corresponding synoptic scale flow. At the other hand maximum temperatures reaching 18°C occured during Foehn at Isungua which is located at the leeside i.e. downstreams of the ice divide. Starting at summit level, these high leeside temperatures associated with Foehn at Isungua could be nicely explained by assuming dry adiabatic warming during descent of the air. In that sense the investigated event seems to meet very nicely the ideal thermodynamic view of Foehn. This is not to be expected a priori as a number of objections exist against a plain thermodynamical view of Foehn.

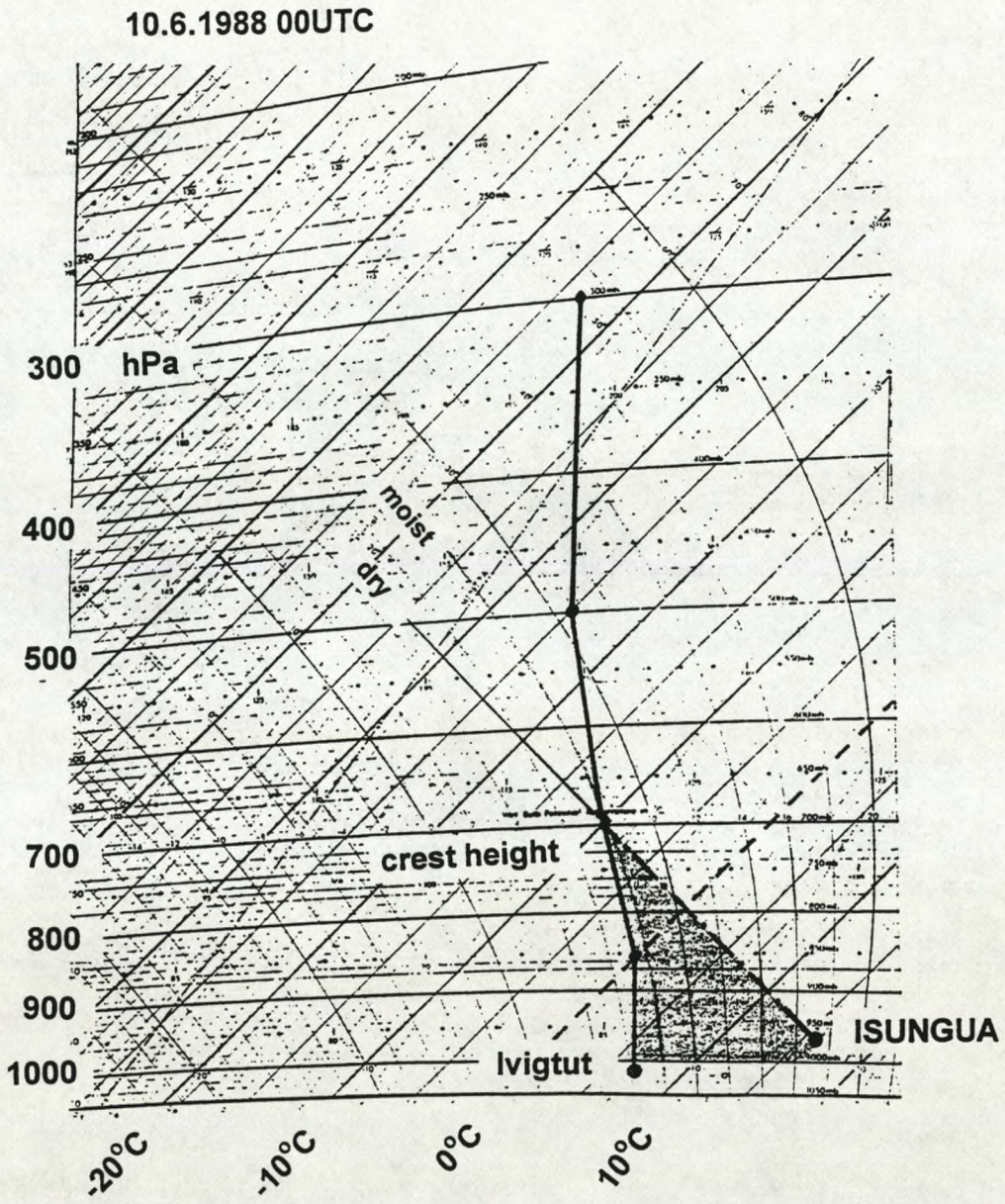

Fig.1: Tephigram for Ivigtut, 10.6.1988 00UTC (———) during Foehn at Isungua.
Dry adiabatic descent from crest height towards Isungua is entered as well (— · — · —).

5. Isentropic analysis

Assuming quasistatic, adiabatic motion the atmospheric flow is basically governed by pressure gradients at isentropic surfaces. Applications of this basic concept to Alpine Foehn events have been proven to be valuable tools (Seibert, 1990), an attempt of extension towards the Greenland Ice Sheet is presented by the following vertical cross sections of potential temperature. The proposed SE-NW transect across the southern Greenland Ice Sheet follows the mean direction of the air flow during Foehn at Isungua (IS) and is mainly based on atmospheric soundings at Ivigtut (IV), Sondrestrom/Sisimiut, Umanak/Jakobshavn (UM) and Thule (TH, Fig. 2, insert). Intermediate information e.g. above the ice and the sea resp.was taken from ordinary weather maps too.

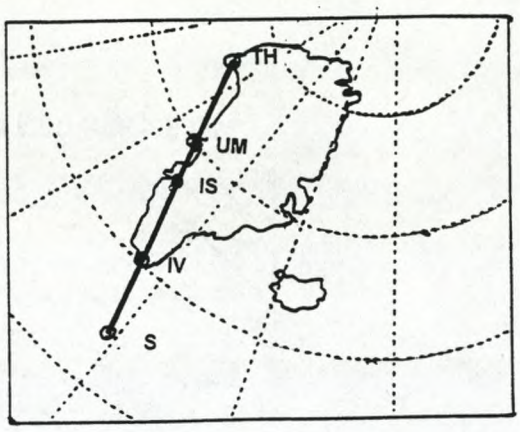

a)

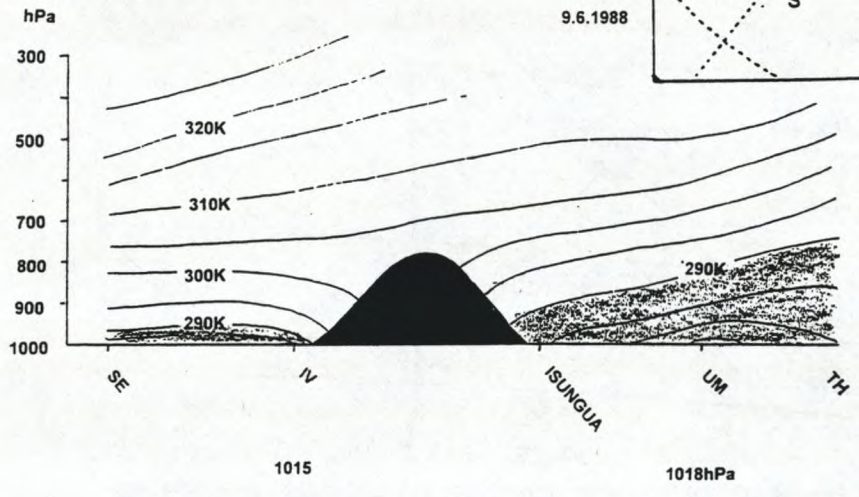

b)

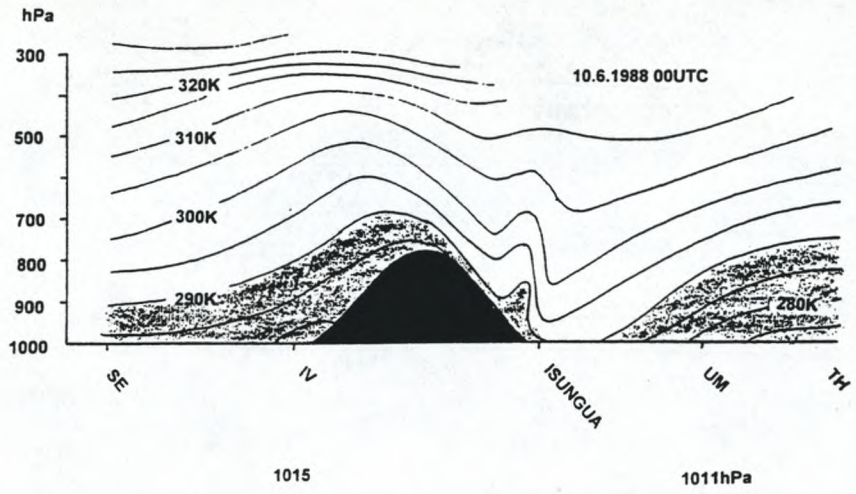

c)

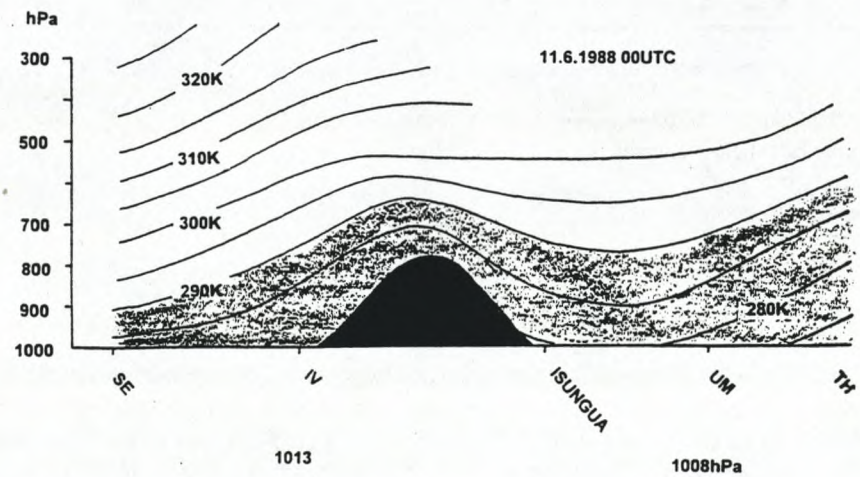

Fig.2: SE-NW vertical cross section of potential temperature for :

a) the day before
b) during
c) the day after Foehn at Isungua

As indicated by the shaded areas <290K, a body of cold and stably stratified air initially approaches the southern coast of Greenland whereas another pool of arctic air covers the mid western coast and Baffin Bay area respectively (Fig. 2a). Both are clearly blocked by the barrier of the Greenland Ice Sheet.
Until Foehn develops at Isungua during the next day (Fig. 2b), ongoing advection substantially increases the depth of the southern body of cold air. Due to stable stratification this air mass is partly blocked, resp. deflected by Greenland topography, whereas at upper levels the unblocked air is lifted above the crest of the Ice Sheet. Corresponding horizontal pressure gradients developed and accelerated downflow leewards of the ice divide pushed the front of arctic air even farther north. Unfortunately relevant information above the ice is sparse, thus mesoscale details of the analysis have to be judged critically. Nevertheless, a leewave admittedly analysed by one measurement point only, would perfectly fit the known features of atmospheric flow during Foehn.
Until the day after Foehn at Isungua, a mighty body of potentially cold air swept the whole transect which corresponds to the observed northward migration of the associated frontal system (Fig.2c).

Summarizing, the investigated Foehn event seems to reflect very nicely the alpine experience, both - from the thermodynamic and dynamic point of view respectively. This is more than a priori to be expected in front of this preliminary analysis and the extreme regional and temporal variability inherent with Foehn.

6. Implications on the mass- and energy budget of the Greenland Ice Sheet

No doubt any mesoscale atmospheric feature principally might be of relevance at least for the *regional* energy- and mass budget of an ice sheet too. This might be imagined e.g. by distortion of the katabatic regime, channeling /pass effects, enhanced drifting snow activity and enhanced luv/lee effects on cloudiness, precipitation and accumulation generally. Let´s examplify a basic temperature effect of Foehn at the ice sheet too: during Foehn in Isungua with maximum temperatures about 18°C , the melting zone with temperatures above 0°C might be expected to have reached 1700m a.s.l. instead of 1100m a.s.l. as estimated for a clear day within the observational period.. An area of some 500× 500km^2 might have been concerned in that sense for about half a day. Let´s remember in this context too that for Greenland coastal stations *January* maximum temperatures of +12°C have been reported, more than +25°C during *June*, which both were likely to be due to Foehn events.
At the other hand it is to be mentioned of course, that mature Foehn does not occur every day. In fact its frequency of occurence within the different sectors of the Greenland Ice Sheet is amongst the wealth of relevant questions left for future work.

References:

Putins P., 1970: The Climate of Greenland, in: World Survey of Climatology, Vol.14, ed.: S. Orvig, 370p.

Seibert, P., 1990: South Foehn Studies during the ALPEX Experiment, Meteor. Atmos. Phys. 43, 91-103.

KATABATIC WIND OVER GREENLAND: COMPARISON OF MODEL RESULTS WITH OBSERVATIONS

Gunthard **Niederbäumer**
Department of Geography,
Swiss Federal Institute of Technology
Zürich, Switzerland

Results from a two dimensional mesoscale hydrostatic katabatic wind model are compared with field observations from the ETH Greenland Expedition (Ohmura et al., 1991, 1992).

1 Model description

The model is based on a Antarctic katabatic wind model used and described by Waight (1987) and Parish and Waight (1987). Major modifications for the situation in Greenland, in particular, changes in parts of the surface energy flux parameterization were necessary. For the short wave radiation, the formula from Konzelmann et al. (1994) is used:

$$S = 0.84\ S_0 \exp(-0.027\tau_L m_r)\frac{1-\alpha_s}{1-\alpha_s\alpha_a}, \tag{1.1}$$

where α_a is the albedo of the atmosphere, α_s is the surface albedo, the relative optical air mass is m_r, S_0 the solar radiation on the top of the atmosphere and τ_L is the Linke turbidity factor. This parameterization was developed with data from Greenland (Konzelmann et al., 1994), and it is the best available at present. For the sensible heat flux a parameterization from Beljaars and Holtslag (1991) gives good results for the situation in Greenland. The sensible heat flux Q_H is

$$Q_H = \frac{-u^* k\,(\theta_1 - \theta_s)\,c_p\rho}{\ln\left(\frac{z}{z_{0H}}\right) - \Psi_H\left(\frac{z}{L}\right)}, \tag{1.2}$$

where θ_1 is the potential temperature at the first σ-level, θ_s is the potential surface temperature, c_p the specific heat, ρ the density of the air, z is the height, L the Obukhov length, z_{0H} the surface roughness length for heat and Ψ_H the dimension-less stability function for heat:

$$-\Psi_H = \left(1 + \frac{2}{3}\frac{z}{L}\right)^{\frac{3}{2}} + b\left(\frac{z}{L} - \frac{c}{d}\right) exp\left(-d\frac{z}{L}\right) + \frac{bc}{d} - 1, \tag{1.3}$$

with $b = 0,667$, $c = 5$ and $d = 0.35$.

2 Field data

An early spring situation in 1991 with high albedo and cold snow surface, the 48-hour period from 11.May 1991 00:00 UTC to 13.May 1991 00:00 UTC has been chosen for comparison with model results. This period was a very nice weather situation without

low level clouds. The weather maps of the German Weather service show a very weak pressure gradient at the surface level. The synoptic observations at the ETH Camp report only some high cirrus clouds. The solid lines in Figure 2.1 show the observed wind speed and wind direction in 10 m height, the screen level temperature and the net short wave radiation. In Figure 2.2 the solid lines shows the up- and downward long wave radiation and the net long wave radiation.

The temperature reaches a maximum of -7 °C in early afternoon and a minimum of -22 °C at night. The wind speed is strongly correlated with the temperature. Highest wind speeds occur shortly after the early morning temperature minimum. The wind direction during night points down slope and turns almost to cross slope direction during morning. The short wave radiation reaches a maximum of 120 Wm^2. The incoming long wave radiation at the surface is stable around 190 Wm^2 and the outgoing long wave radiation follows the surface temperature with a maximum of -260 Wm^2 and a minimum of -220 Wm^2. This gives a net long wave radiation between -30 and -70 Wm^2. The measurements for the turbulent heat flux started later in the season.

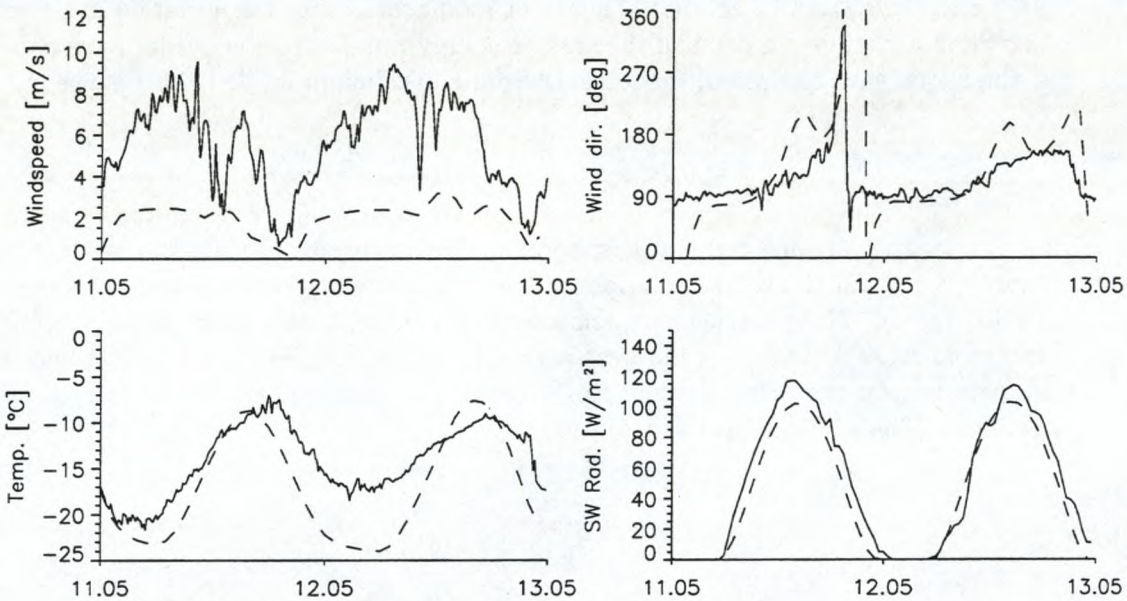

Figure 2.1: *The solid lines shows measured wind speed at 10m (top left), wind direction at 10m (top right), screen level temperature (bottom left) and short wave radiation (bottom right) for the time period from 11.5.1991 to 13.5.1991 at the ETH Camp. The dashed lines shows the model results for the grid point representing the position of the camp.*

3 Comparison

A run with the two dimensional model is compared with the measured data. A profile from the summit along the 72th meridian to the coast and about 200 km into the open ocean. The grid has 160 points with a distance of 5.52 km in the horizontal and 15 levels in the vertical distance. The top of the model is fixed at 250 hPa. The albedo is taken constant over the 48-hours simulation and the snow density and subsurface temperature is taken constant in time and space. The result shown in Figure 2.1 underestimate the wind speed. The measured and observed daily cycle are corresponding in phase, but

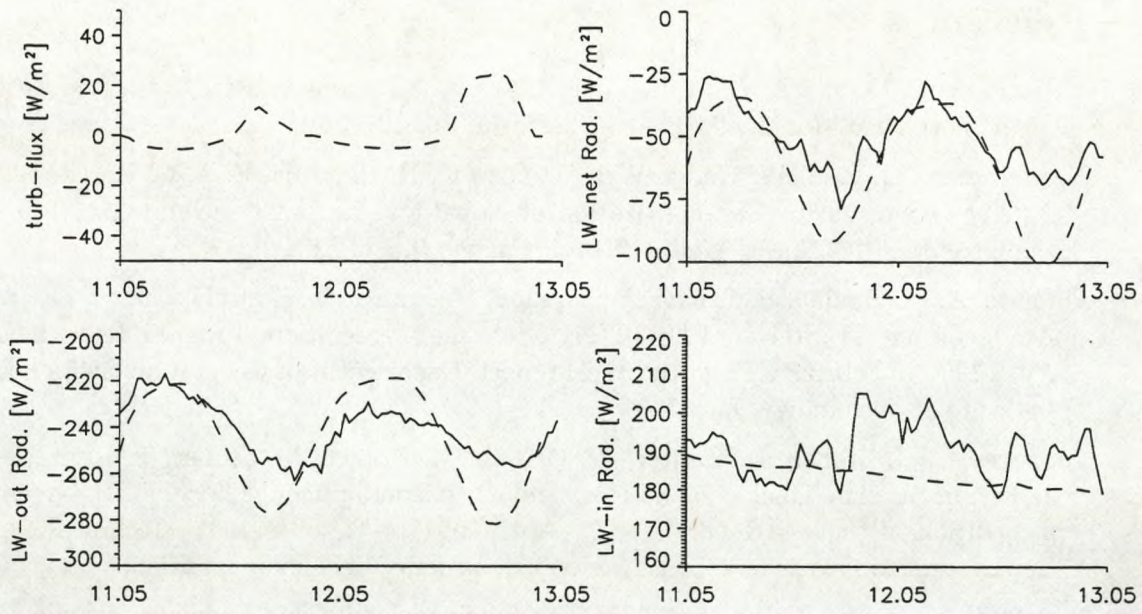

Figure 2.2: *The solid lines shows measured net radiation (top right), outgoing long wave radiation (bottom left) and incoming long wave radiation (bottom right) for the time period from 11.5.1991 to 13.5.1991 at the ETH Camp. The dashed lines shows the model results for the grid point representing the position of the camp with the turbulent heat flux in addition (top left). For this time period are no measurements for the turbulent heat flux available.*

the computed wind maximum is about 6 m/s too low. One possible reason is the weak synoptic pressure gradient pointing west-northwest, but this cannot explain the entire difference. The wind direction corresponds to the observation. In the model the minimum temperature is about 5 °C too low but the maximum temperature comes close to the measured values. The short wave radiation is in accordance with the measurements. The long wave radiation correspond well during night and early morning, but ist too low in the afternoon. The variaton in the measured incoming long wave radiation might be the result of different air masses moving over the ETH Camp. With a two dimensional model it is not possibel to simulate this kind of perturbations. The turbulent sensible heat flux is negative during night and positive during the day.

4 Conclusion

The model is able to simulate dry and cold snow situations in a satisfactory way. Most of the processes are well represented in the model. The results are best for dry snow conditions. With melting and freezing processes at the surface, we need additional parameterization of these processes. The reason for the too low wind speed has also to be investigated in more detail. Despite these drawback, the model has become a useful tool to study single processes in the surface layer above the Greenland ice sheet.

References

Beljaars, A. C. M. and A. A. M. Holtslag, 1991: Flux Parametrisation over Land Surfaces for Atmospheric Models. *J. of Appl. Meteoro.* **30**, 327–341.

Konzelmann, T., R. S. W. van de Wal, W. Greuell, R. Bintanja, E. A. C. Henneken, and A. Abe-Ouchi, 1994: Parametrization of global and longwave incoming radiation for the Greenland Ice Sheet. *Global Planet. Change* **9**, 143–164.

Ohmura, A., K. Steffen, H. Blatter, W. Greuell, M. Rotach, T. Konzelmann, M. Laternser, A. Ouchi, and D. Steiger, 1991: ETH Greenland Expedition: Progress Report No. 1: April 1990 to February 1991 Technical report, Department of Geography, Swiss Federal Institute of Technology, Zurich.

Ohmura, A., K. Steffen, H. Blatter, W. Greuell, M. Rotach, M. Stober, T. Konzelmann, J. Forrer, A. Abe-Ouchi, D. Steiger, and G. Niederbäumer, 1992: ETH Greenland Expedition: Progress Report No. 2: April 1991 to October 1992 Technical report, Department of Geography, Swiss Federal Institute of Technology, Zurich.

Parish, T. R. and K. T. Waight, 1987: The Forcing of Antarctic Katabatic Winds. *Mon. Wea. Rev.* **115**, 2214–2226.

Waight, K. T., 1987: *The Dynamics of Antarctic Katabatic Winds* Ph. D. thesis, Department of Atmospheric Science, University of Wyoming, Laramie, WY, USA.

TURBULENT EXCHANGE: RESULTS OF THE GIMEX-VU CAMP

Anton Meesters
Vrije Universiteit, Amsterdam

The GIMEX-VU camp was located at 67°02'N, 48°12'W, in west Greenland, 90 km from the ice margin. The measurements were performed in July 1991. Two eddy correlation systems, at heights of 4 m and 13 m, were used to measure turbulent exchange. Each system consisted of a sonic anemometer, a thermocouple and a Lyman-α moisture fluctuation sensor. Profiles of wind speed, temperature and moisture were measured at six to eight levels using a mast with a height of 30 m.

The sensible heat flux was almost always directed downward, whereas the vapour flux was upward. Sensible heat fluxes were determined from vertical velocity fluctuations and temperature fluctuations; the latter were determined either by the sonic anemometers or by the thermocouples. It appeared that if the thermocouples were used, the resulting sensible heat flux was markedly reduced compared to the case with sonic anemometer temperatures. It is likely that the former results are erroneous since they cannot be matched well with the profile measurements. The most probable error source seems to be a spurious temperature fluctuation of the thermocouples by the combined effect of insolation and fluctuating (ventilating) wind speed. This effect is absolutely small and has been almost entirely neglected in the literature, but it can be relatively large in the present case because the actual fluxes are very small. As a consequence, the vertical gradients of temperature and moisture content are also small, and it took some time to overcome the associated difficulties.

The investigation has concentrated upon daytime measurements for which the surface was melting, so that surface values for temperature and moisture content were accurately known. A set with 165 cases of half an hour duration has been selected. They have been classified into four groups: "neutral", "stable", "windy neutral" and "windy stable", the 8 m wind speed being less than 6 m/s for the former two and more than 6 m/s for the latter two.

Comparison of the observed turbulent fluxes to profile measurements close to the surface yielded (preliminary) roughness lengths of $z_0 = 6 \times 10^{-4}$ m, $z_T = 2 \times 10^{-6}$ m, and $z_q = 8 \times 10^{-4}$ m. These values do not depend significantly on the weather conditions, but z_0 is increasing somewhat in the course of the measurement campaign, as the surface was roughened by ablation.

For each of the four classes, the observed profiles were averaged. Theoretical profiles were also calculated for each case, using

$$\frac{v_h}{u_*} = \frac{1}{k}\left(\ln\frac{h}{z_0} + 6\frac{h}{L}\right) ;$$

$$\frac{\theta_h - \theta_{surf}}{\theta_*} = \frac{1}{k}\left(\ln\frac{h}{z_T} + 8\frac{h}{L}\right) ;$$

and a similar equation for moisture. The resulting profiles were also averaged over each class.

Figure 1 compares the results for the wind speed, and figure 2 for the potential temperature. It is seen that in general, reasonable accordance is found (horizontal shifts are caused by the use of constant roughness lengths for the calculations, and are not significant). For class S, there are discrepancies which can be explained from the existence of a shallow katabatic layer for this case. Katabatic effects are believed to play a role also for the other classes, but there the layer is too thick to cause significant distortions below mast height.

It is concluded that in spite of the katabatic wind that develops over the ice sheet, it is well possible to infer fluxes from profile measurements close to the surface. However, because of the weak fluxes and small gradients, it should be made sure that the instruments are able to resolve the gradients well. In particular, it is recommended to use aspirated instruments for measuring temperature, which has not been done in the present investigation.

reference:

Meesters, Henneken, Bink, Vugts and Cannemeijer : "Estimating turbulent fluxes from simple meteorological measurements for smooth melting ice (S.W. Greenland, July 1991)". To be submitted to Boundary-Layer Meteorology (?).

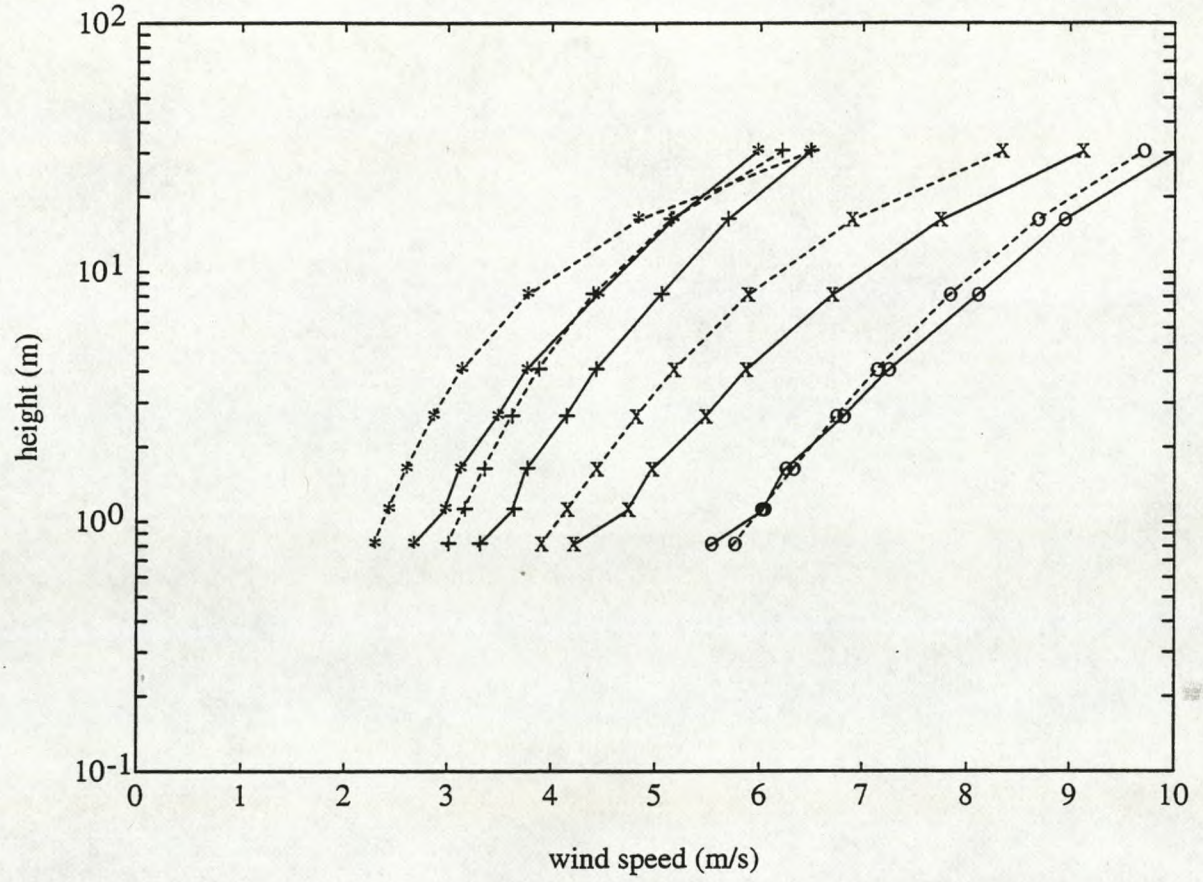

figure 1. Average profiles of wind speed, observed (solid lines) and calculated from the fluxes (dashed lines). The following classes are discerned: "neutral" (+), "stable" (*), "windy neutral" (o) and "windy stable" (x).

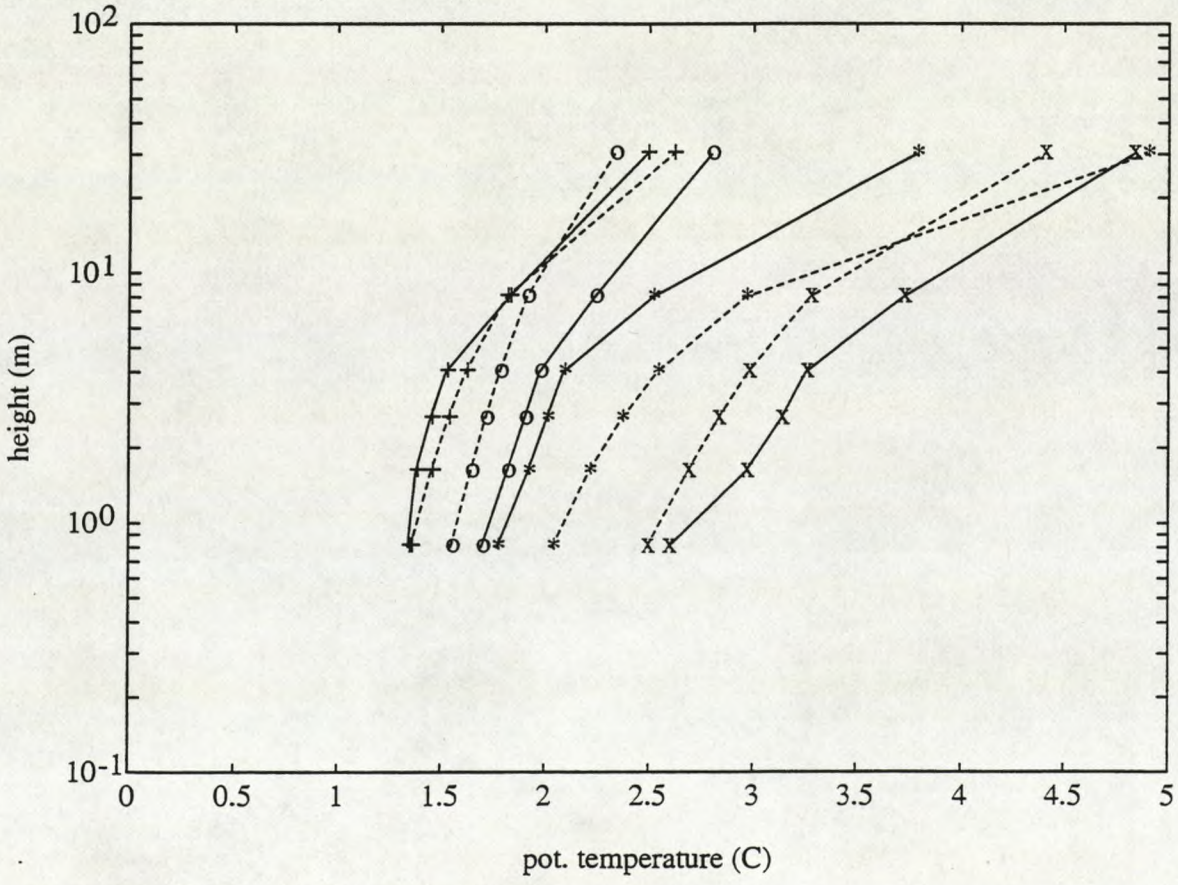

figure 2. The same, but for potential temperature.

GLACIOMETEOROLOGICAL, ISOTOPICAL AND CHEMICAL STUDIES ALONG THE NORTH GREENLAND TRAVERSES 1993-95: IMPLICATIONS FOR THE POSITION OF NORTH GRIP

H. Fischer and D. Wagenbach

Institut für Umweltphysik, Universität Heidelberg, Im Neuenheimer Feld 366, D-69120 Heidelberg

Background

Anthropogenically induced changes in climate and atmospheric chemistry have focussed interest on deep ice core studies from polar regions (GRIP, GISP, EPICA) as reliable, conservative archives of past climatic and atmospheric conditions. The interpretation of e.g. isotopic ice core records, however, is dependend on the validity of the $\delta^{18}O$/temperature-relationship assumed for the area investigated and its sensitivity on temporal changes. The interpretation of chemical ice core records in terms of atmospheric conditions is crucially dependend on the knowledge, how changing glaciometeorological parameters (snow accumulation, temperature) control the deposition process of aerosols and water reactive trace gases. Ground truthing of such relationships may be accomplished by ice core studies covering a wide range of glaciometeorological conditions prevailing at various geographical regimes on the ice sheets.

Thus, reestablishing of the EGIG-line by the Geodätisches Institut, Braunschweig, in 1990-92 enabled us to carry out a glaciological surface study along a longitudinal traverse through central Greenland (Anklin et al, 1994, Fischer et al., 1995, Fischer and Wagenbach, 1995). In the following summers 1993-95, three glaciological traverses were performed in the vast region of the northern Greenland Ice Sheet in a cooperation of the Alfred-Wegener-Institut, Bremerhaven, and the Institut für Umweltphysik. Along these traverses 13 deeper ice cores were drilled covering a time span of 500-1000 years and an extensive surface study (shallow ice cores, pit studies, firn temperature measurements) was performed (see Fig. 1).

Up to know, 3 deeper ice cores and 8 shallow firn cores together with various snow pits along the meridional subsection GRIP-B21 of the North Greenland Traverses (NGT), were analysed in Heidelberg for their isotopic ($\delta^{18}O$, δD, *d*) content as well as for ion concentrations (F^-, MSA^-, Cl^-, NO_3^-, SO_4^{2-}, Na^+, NH_4^+, K^+, Mg^{2+}, Ca^{2+}). Here we present first results of the glaciometeorological, isotopical and chemical surface study along this meridional subsection, which, together with our findings along the EGIG-line, are discussed with respect to the position of the new deep drilling site North GRIP.

Results

Dating of shallow cores and snow pits was accomplished by counting annual layers in the firn (i.e. δD, $\delta^{18}O$, mineral dust species). The outcome of the derived average snow accumulation rates *A* over the last 10 years (see Fig. 2a) revealed a distinct low accumulation area north of 74°N, with *A* (≈10 cm w.e /a) being up to 50% lower than previous values comprised by Ohmura and Reeh (1991).

The geographical distribution of δD (based on 20 snow pits covering 3-5 years) in Fig.2c shows a strong decline from Crête to B16 and following a weak northward increase to B21. Unfortunately temperature measurements along the NGT are not finally evaluated, however,

applying the δD/temperature-relationship of the EGIG-line east of the ice divide ($\delta D = 4.6T - 123.4$; Fischer et al., 1995) indicates a temperature minimum around -40°C along the NGT at 74°N. The deuterium excess *d* north of the EGIG-line (see Fig.2d) remains constant up to 76°N, followed by a 3-4‰ decline further north, indicating water vapour advection from cooler ocean source areas being more important in this high latitude region.

To illustrate the findings concerning the chemical components the geographical distribution of sulfate, a species whose natural contributions (sea salt, biogenic emissions etc.) are nowadays dominated by anthropogenic fuel combustion, is exemplarily plotted in Fig.2b. A continous northward increase in recent sulfate concentrations is observed, which may partly be attributed to the accompanying decrease in annual snow accumulation. The northernmost positions B18, NGT18 and B21 show significantly higher concentrations than expected from their local snow accumulation rate, possibly due to higher influence of anthropogenically polluted air masses advected over the pole region during winter/spring. Also plotted in Fig.2d are preindustrial background levels at B16, B18 and B21 together with respective values at Summit (Whitlow et al., 1992) and Site A (Laj, 1992). Preindustrial sulfate concentrations amount only to ~1/3 of recent values but reveal as well a clear northward increase governed by the concurrent decline in snow accumulation.

Implications

Due to the unexpectedly low accumulation rates around 74°N a new deep drilling in this area is expected to succeed in covering the Eem interglacial well above bedrock, thus, reducing potential disturbances, which impair the interpretation of the isotopic records at GRIP and GISP, significantly. Choice of the new drill site on top of the main ice divide reduces modelling efforts significantly, however, assignment of this site to the different isotopic regimes east and west of the ice divide, as derived along the EGIG-line (Fischer et al., 1995), is not straightforward and possibly variable due to temporal changes in the position of the ice divide. Also temporal variations in snow accumulation due to changing ice divide position are more likely to occur in the west (Fischer et al., 1995), thus resulting in significant variations in ionic background levels which are not caused by temporal changes in atmospheric concentrations.

References

Anklin, M., Stauffer, B., Geis, K. and Wagenbach D. (1994). Pattern of annual snow accumulation along a West Greenland flow line: no significant change observed during recent decades. *Tellus*, **46B**, 4, pp. 441-444.

Fischer, H., Wagenbach, D., Laternser, M. and Haeberli W. (1995). Glacio-meteorological and isotopic studies along the EGIG-line, central Greenland. *J. of Glaciology*, **41**, 139, pp. 515-527.

Fischer, H. and Wagenbach, D. (1995). Large scale spatial trends in recent firn chemistry along an east-west transect through central Greenland. Submitted to *Atm. Env.*.

Laj, O., Palais, J.M. and Sigurdsson H. (1992). Changing sources of impurities to the Greenland Ice Sheet over the last 250 years. *Atm. Env.*, **14**, pp. 2627-2640.

Ohmura, A. and Reeh, N. (1991). New precipitation and accumulation maps for Greenland. *J. of Glaciology*, **37**, 125, pp. 140-148.

Whitlow, S., Mayewski, P.A. and Dibb, J.E. (1992). A comparison of major chemical species seasonal concentration and accumulation at the South Pole and Summit, Greenland. *Atm. Env.*, **26**, 11, pp. 2045-2054.

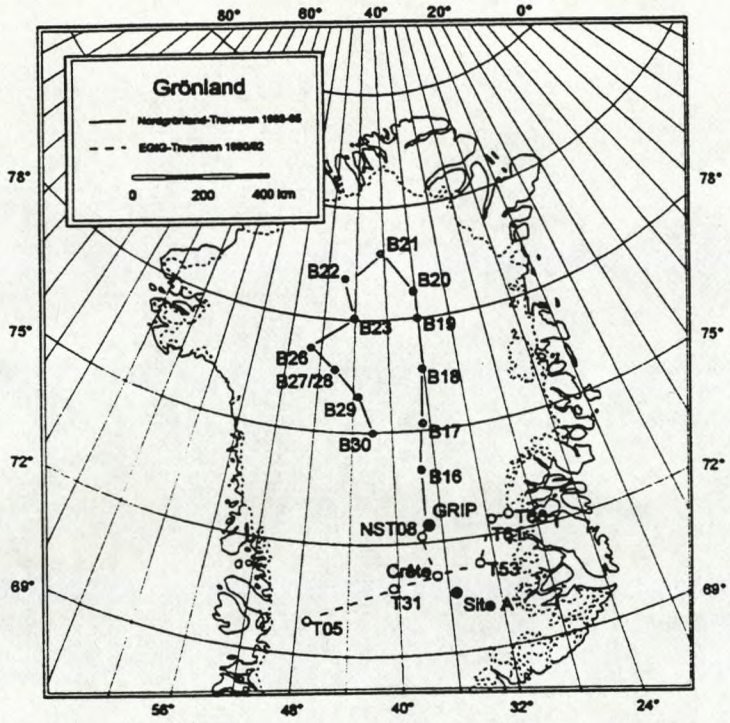

Fig. 1: Map of northern Greenland showing some of the shallow firn core sites along the EGIG-traverses 1990-92 (dashed line) and the deeper ice core sites along the North Greenland Traverses 1993-95 (solid line). Results in the text concern the meridional line from Crête over GRIP, B16, B18 to B21.

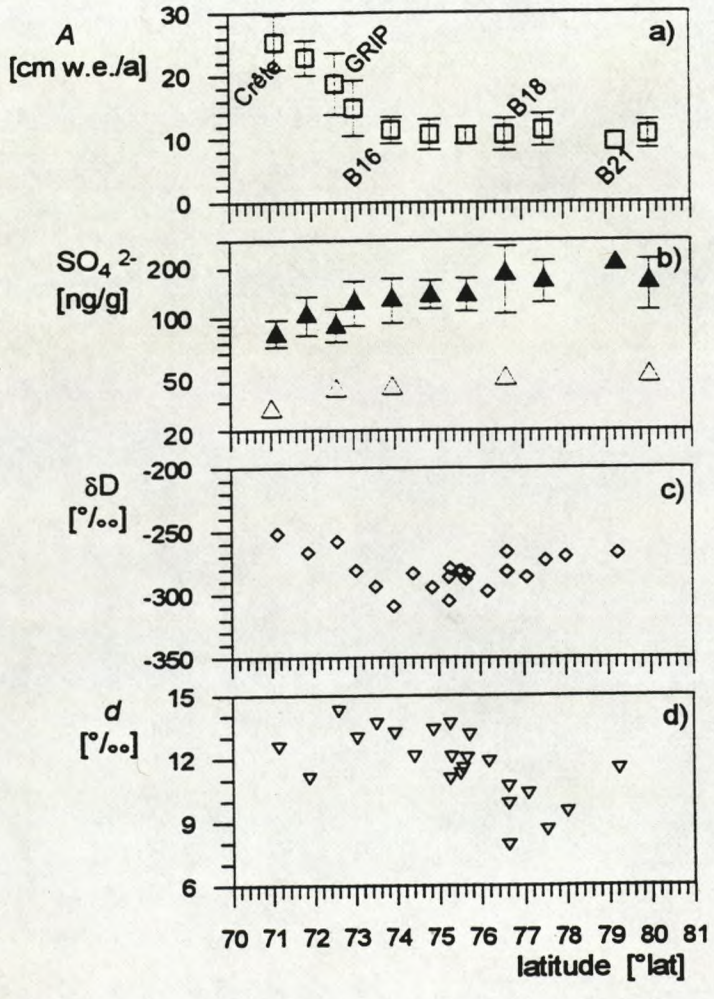

Fig. 2: Latitudinal distribution of various firn parameters along the meridional line Crête-B21: a) Average annual snow accumulation at 10 shallow firn core sites covering the last 10 years together with their standard deviations. b) Average annual water weighted mean of recent sulfate concentration in the firn cores together with their standard deviation (full symbols) and preindustrial sulfate concentrations (open symbols) at B16, B18, B21, Summit (values given by Whitlow et al., 1992 for the time span 1259-1900) and Site A (values given by Laj et al., 1992, time span: 1811-1820). c) Average annual water weighted δD of 20 snow pits covering approximately 2-5 years. d) Average water weighted deuterium excess (d=δD-8δ^{18}O) in the snow pits.

THE AWI NORTH GREENLAND TRAVERSE 1993-1995

Matthias Schwager[1], **Sepp Kipfstuhl, Thorsteinn Thorsteinsson,**
Frank Wilhelms & Heinz Miller
Alfred-Wegener-Institut für Polar- und Meeresforschung
Postfach 120161, 27575 Bremerhaven, Germany

Hubertus Fischer[2] **& Dietmar Wagenbach**
Institut für Umweltphysik, Universität Heidelberg, Germany

Stefan Sommer[3]
Physikalisches Institut, Universität Bern, Switzerland

Introduction

Little is known about the distribution of precipitation and about the isotopic signature and the impurity content in snow and ice of Northern Greenland. There is special interest in the temporal variation of these parameters prior and during the present time of anthropogenic influence (the last 250 years). After the deep drilling activities of GRIP and GISP2 as well as the German traverse work along the EGIG line were finished the AWI North Greenland Traverse was realized during the summer seasons 1993-1995.

Field program

At 12 sites ice cores 100-175 m in length were drilled. The distance between two ice core drilling sites was 100-150 km. Every 50 km firn cores were drilled to 15 m depth. From these we are able to sample firn from the last decades and get a higher spatial resolution between the ice cores. At each drilling site a snow pit was dug for high resolution sampling of snow for chemical and isotopical analysis. For detailed description of the visual stratigraphy we used backlight profiles (only in the 1995 field season). Temperature measurements in each borehole were made down to 15 m. The position of each drilling site was measured by GPS. At the ice core drilling sites strain nets were set up to measure the deformation rate of the ice sheet. En route gravity measurements were made every 2-5 km. In the seasons 1993 and 1994 ice radar profiles were taken along the route. Figure 1 shows the route of the AWI North Greenland Traverse. Table 1 lists all drilling positions measured by GPS.

[1] e-mail: mschwage@awi-bremerhaven.de
[2] e-mail: fi@uphys1.uphys.uni-heidelberg.de
[3] e-mail:sommer@climate.unibe.ch

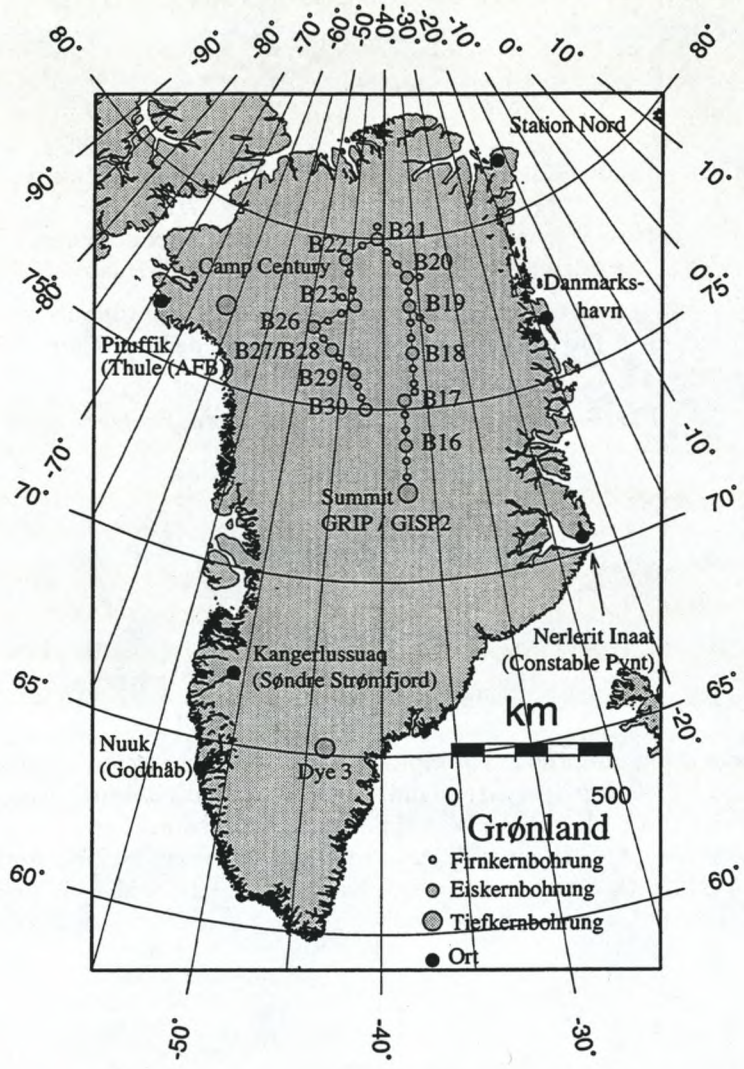

Fig. 1: Route of the AWI North Greenland Traverse. Big circles show ice core drilling sites; small circles show firn core drilling sites.

Results

Figure 2 compares the record of $\delta^{18}O$ with the visual stratigraphy in snow pit NGT 42 (76°N, 43°30' W; 2870 m WGS 84). We see the typical seasonal signals in $\delta^{18}O$. The average $\delta^{18}O$ is -35.8 ‰. The record covers a time span of nearly 5 years. The average accumulation is about 45 cm of snow per year. Assuming a density of 0.35 g/cm^3, we estimate an average accumulation rate of approximately 160 mm w.e. a^{-1} for the last 4 years. This is in good agreement with the accumulation rate we obtain from ice core B 29. The stratigraphy indicates the different layers identified by grain size and hardness. The $\delta^{18}O$ record shows high values where depth hoar layers appear in the stratigraphy.

In Figure 3, the $\delta^{18}O$ record for different sections of ice core B 21 (80°N, 41°W) is plotted. In the first meter we see the annual layers, as expected. With increasing depth the period increases to 3-6 years. The other ice cores of the traverse show similar profiles.

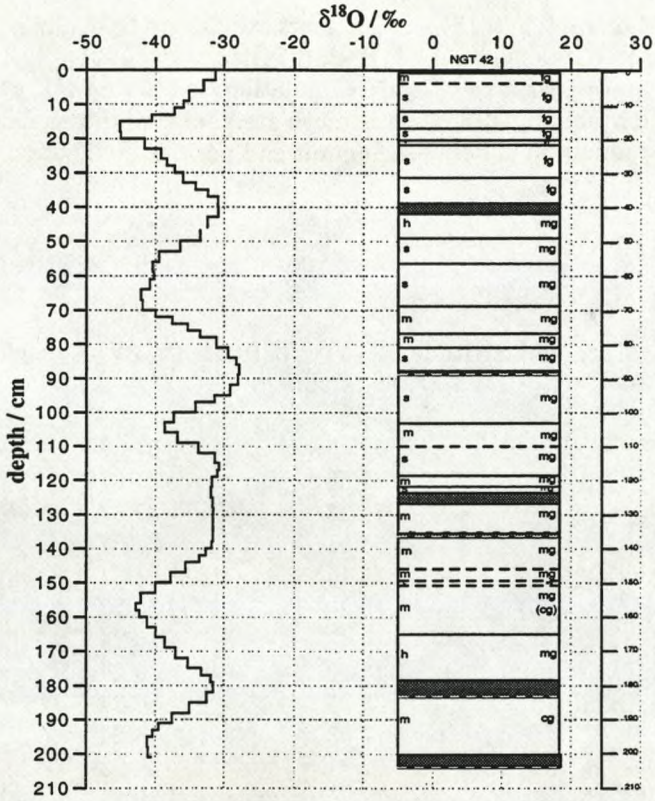

Fig. 2: $\delta^{18}O$ profile (left) and visible stratigraphy (right) in snow pit at NGT 42. Layers determined by grain size (fine grained = **fg**, medium grained = **mg** and coarse grained = **cg**) and hardness (soft, **m**edium, **h**ard). Solid lines indicate crusts; dashed lines indicate boundary between firn layers. Shaded areas represent depth hoar layers.

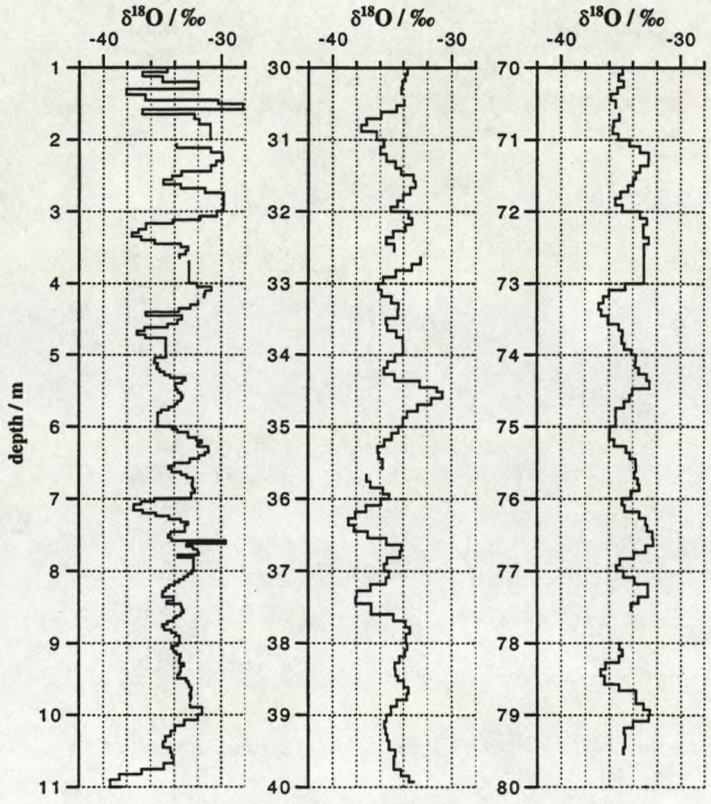

Fig. 3: $\delta^{18}O$ profile of core B 21 (80°N, 41°W, 2185 m WGS 84).

Preliminary accumulation rates over the last 200 years are derived from all ice core positions. Our results confirm the precipitation data of Ohmura & Reeh (J. Glaciol, 37, 1991, 140-148) in the western part of the traversed area. However, the area of low accumulation (< 150 mm w.e. a^{-1}) is much larger and the gradient towards the low accumulation area is much steeper. Within the short distance of 150 km the accumulation drops by about 30 % between Summit and position NGT 03 (73° 56' N, 37° 37' W, 3040 m WGS84).

Site	Core	Longitude (° ' N)	Latitude (° ' W)	Height (m WGS 84)
NGT 01		73 01	37 38	3279
NGT 02		73 30	37 39	3137
NGT 03	B16	73 56	37 37	3040
NGT 04		74 23	37 37	2963
NGT 05		74 51	37 37	2873
NGT 06	B17	75 15	37 37	2820
NGT 09		75 29	36 23	2713
NGT 12		75 43	36 24	2671
NGT 13		76 10	36 24	2591
NGT 14	B18	76 37	36 24	2508
NGT 17		77 03	36 24	2415
NGT 18		77 31	36 23	2319
NGT 19	B19	78 00	36 23	2234
NGT 20		77 17	33 50	2173
NGT 21		77 38	35 04	-
NGT 22		78 25	36 26	-
NGT 23	B20	78 50	36 30	2147
NGT 24		78 49	34 39	-
NGT 25		79 13	37 57	-
NGT 26		79 37	39 30	-
NGT 27	B21	79 59	41 08	2185
NGT 28		80 21	41 07	-
NGT 29		79 47	43 30	-
NGT 30	B22	79 20	45 54	-
NGT 31		78 56	45 16	-
NGT 32		78 26	44 33	-
NGT 33	B23	78 00	44 00	2543
NGT 34		78 13	45 53	-
NGT 35		77 45	45 46	2615
NGT 36		77 29	47 28	2625
NGT 37	B26	77 15	49 13	2598
NGT 38		76 57	47 44	2666
NGT 39	B27/28	76 39	46 29	2733
NGT 40		76 27	45 27	2814
NGT 41		76 14	44 29	2858
NGT 42	B29	76 00	43 29	2874
NGT 43		75 40	42 57	2921
NGT 44		75 20	42 28	3017
NGT 45	B30	75 00	42 00	2947

Table 1: Drilling sites of the North Greenland Traverse measured by GPS (no post processing applied).

GLACIER BASIN INVESTIGATIONS 1995 ON HANS TAUSEN ISKAPPE, NORTH GREENLAND

Henrik Højmark Thomsen[1], Niels Reeh[2], Ole B. Olesen[1] and Peter Jonsson[3]

1) Geological Survey of Denmark and Greenland (GEUS), Denmark
2) Danish Polar Center (DPC), Denmark
3) Lund University of Technology (LUT), Sweden

A glaciological project has been carried out from 1993 to 1995 on Hans Tausen Iskappe, a local ice cap in North Greenland (Fig.1). The project was funded by the Nordic Environmental Research Programme 1993-1997 launched by Nordic Council of Ministers. The project is a collaboration between 6 institutions from Denmark, Iceland, Norway and Sweden.

The main goal of the project is to investigate the present and past climate and glacier dynamics of North Greenland by means of ice-core records, ice margin studies, mass balance and climate studies and glacial geological studies on and around Hans Tausen Iskappe. The three years of work has mainly been field activities, with planning and reconnaissance in 1993 and an increasing level of field activities during the summer 1994 and 1995. The field work was mainly performed at two locations: 1) The southern dome and 2) an outlet glacier basin including the northern dome in the north-eastern part of the ice cap (Fig. 1). The main activity in the southern dome region was ice core drilling to bedrock and associated ice thickness, strain-rate and velocity measurements. The work at the outlet glacier basin constituted glacier-climate and mass balance studies, collection of ice and snow samples from the surface, measurements of ice thickness, ice velocity and englacial temperatures. In addition glacial geological investigations were made in Nordpasset and Adolf Jensen Fjord north and west of the ice cap respectively (Fig. 1). Since the main part of data and material was obtained during the 1995 field season only very preliminary analyses and data processing has been undertaken. This contribution deals mainly with the glacier basin activities during the summer 1995 and other activities are only described briefly.

Hans Tausen Iskappe

Hans Tausen Iskappe is a local ice cap located in western Peary Land (Fig.1). The north-south extension of the ice cap is about 75 km and the east-west extension is about 50 km. The ice cap has several domes (outflow centres) reaching elevations of 1200 to 1300 m a.s.l. and several outflow glaciers drain the ice cap to the west, north and east. They often terminates in elevations of a few hundred metres with some reaching sea level with a calving front. The southern margin can be characterised as a "quit" sector often covered by snow drifts which survives the summer melt period.

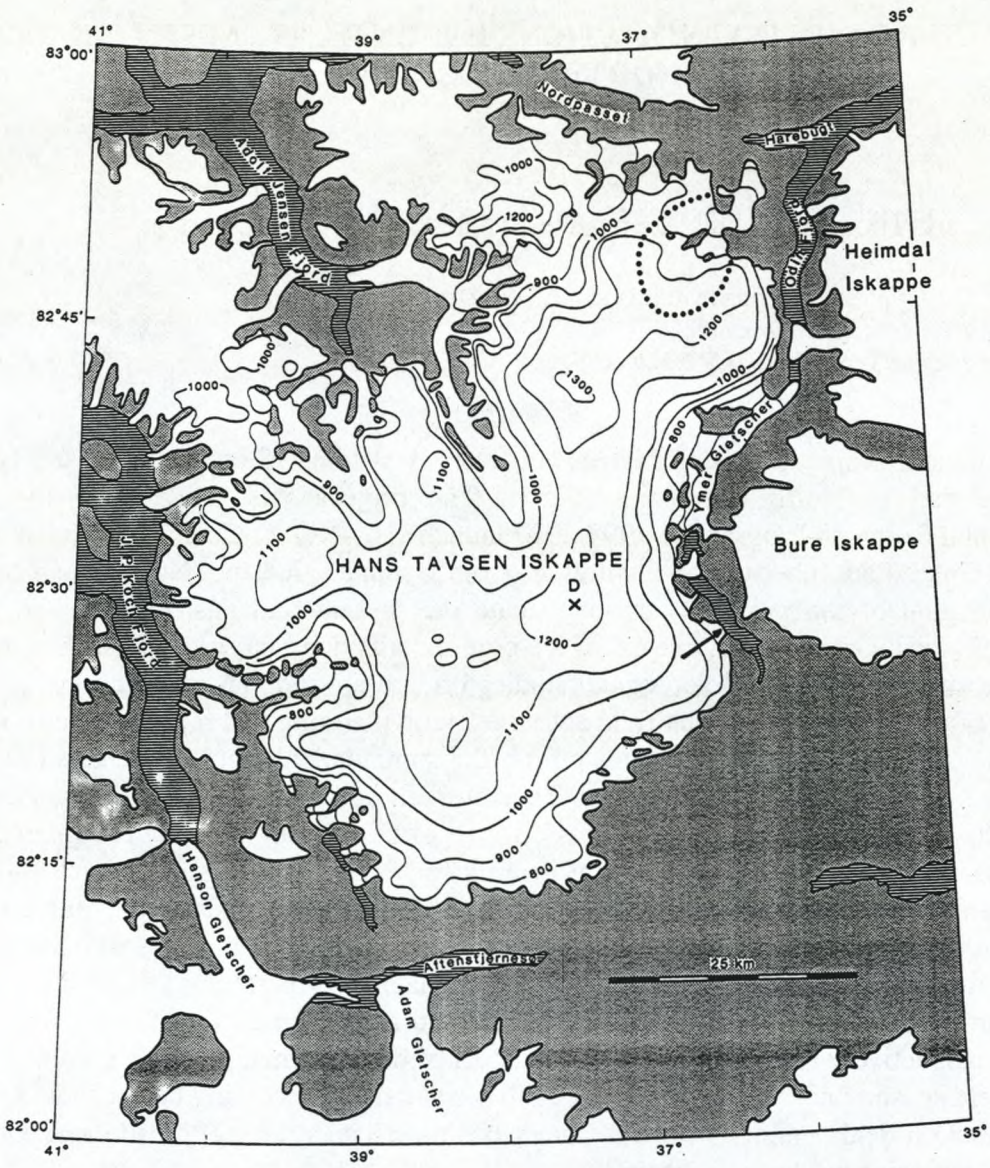

Fig. 1. Hans Tausen Iskappe. Map based on data from the National Survey and Cadastre (KMS), the Geological Survey of Denmark and Greenland (GEUS) and the Geophysical Department of the University of Copenhagen. D: Site of ice core drilling. Dotted line: Limit of ice cap sector for glacier basin investigations. Enlarged map of this ice cap sector is shown in Fig. 2. Arrow: Location of surface ice sampling at an outlet glacier south-east of the southern dome.

Glacier basin activities 1995

Ice-thickness measurements

Ice-thickness measurements by radio-echo soundings were made in June, covering the entire glacier basin (Fig. 2) using snow scooters to drag the radar system. The data will serve as input for ice flow modelling.

A total of approximately 70 line kilometres of data were collected. This includes a long profile following the central flow line from the ice tongue to the northern dome (Fig. 2) and two profiles parallel with the central flow line but approximately 1 km to each side.

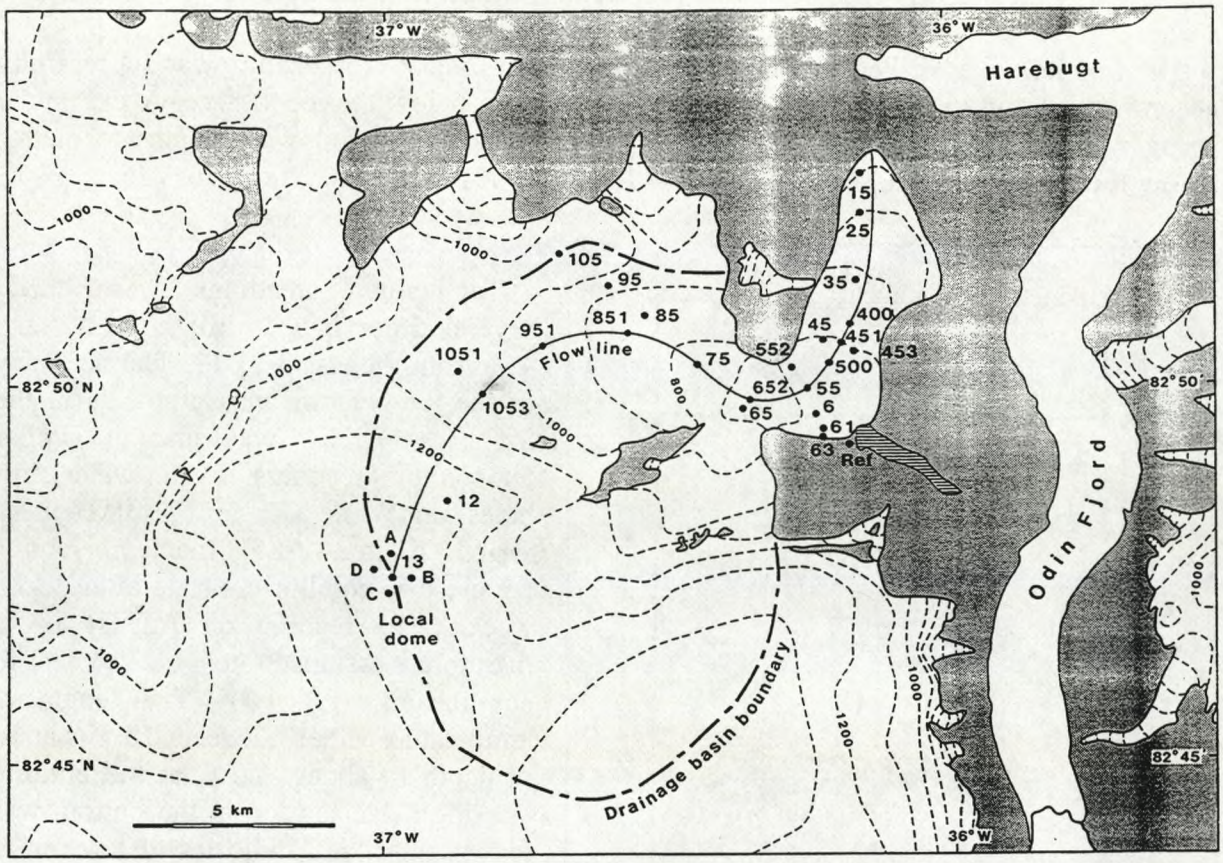

Fig. 2. North-eastern part of Hans Tausen Iskappe showing ice cap sector for glacier basin investigations. The ice cap sector is also shown on Fig. 1. Stakes for mass balance and ice velocity measurements are shown together with the central ice flow line from the northern dome to the glacier terminus.

Furthermore several cross profiles perpendicular to the central flow line were made together with a dense net of lines on the northern dome (Jonsson, 1995). The data awaits further processing and combination with the GPS tracking data. However a comparison of ice-thickness data from the radio-echo sounding and hot water drilling around stake 451 (see later) shows that good quality data can be expected. The radio-echo sounding data show maximum ice-thicknesses of up to 350 m i the glacier basin, whereas the ice-thickness along the centre line of the glacier tongue is generally between 250 m and 300 m. The ice-thickness at the northern dome is around 250 m.

Hot water drilling for ice temperature measurements

Thermistors strings, to measure englacial temperatures from the ice surface to the bottom of the ice, were planned to be installed at the two strain-net sites at stake 13 on the northern dome, at stake 451 on the glacier tongue and around the equilibrium line near stake 75, (Fig. 2). The englacial temperature data will serve as input for ice flow model studies. The holes were drilled with a hot water drill developed by Geological Survey of Denmark and Greenland (Olesen, 1989). Due to very unfavourable drilling conditions, including development of deep

slush fields, rock debris in the ice and the break down of a generator, only the thermistor string at stake 451 was successfully installed.

The first hole was drilled at stake 451 on the glacier tongue. The drilling was successfully accomplished and bedrock reached at a depth of 288 m below the ice surface. A thermistor string was placed in the hole with thermistors mounted at the following depths in metres below the surface: 16, 26, 46, 71, 96, 121, 146, 176, 201, 226, 246, 266, 276, 286.

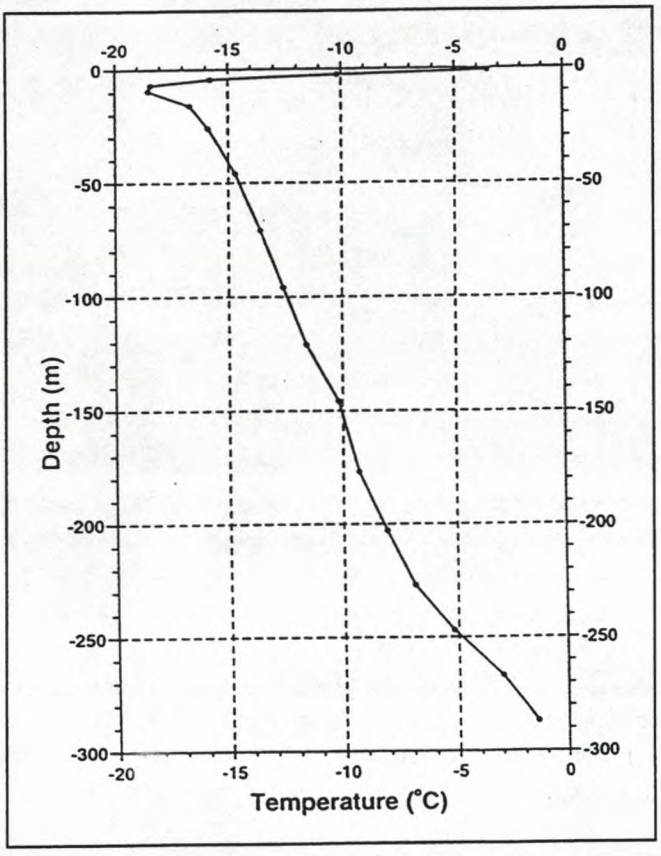

Fig. 3. Temperature-depth profile on the glacier tongue at stake 451. The glacier bottom is at a depth of 288 m.

Temperature readings were made several times in the drill hole at stake 451 from August 3 to 19. The accuracy of the temperature measurements in the ice is ± 0.2°C. According to similar temperature readings in hot water drill holes on White Glacier, Axel Heiberg Island (Blatter, 1985), the temperatures are close to equilibrium state after 2 to 3 weeks. The reading on August 19 is therefore assumed to be close to equilibrium (Fig. 3). The englacial temperature varies between -18.5°C at 10 m depth to about -1.5°C at the bottom. The high temperature at the bottom was unexpected, but indicates that even a moderate climatic warming at the surface may after some time bring the basal temperature in the marginal zone to the pressure melting point resulting in increasing ice flow velocities.

Mass balance 1994/1995

The stakes established in June 1994 between the northern dome at an elevation of about 1320 m and the terminus of the outlet glacier tongue at an elevation of about 220 m were visited at several occasions in June and August 1995 to measure the transit balance for the winter period 1994/95 and the summer period 1995 respectively. In the ablation area stake readings and snow soundings at the stakes were made. In the accumulation area stake readings were made to record the magnitude of snow accumulation and melt. Furthermore density profiles in the top few metres of the snow and firn were made in June and August to compare the profiles and detect effects of summer melting and refreezing. Simultaneously snow and firn samples for $\delta^{18}O$ analysis were selected to elucidate possible fractionation in the accumulation area in connection with refreezing and formation of superimposed ice. The snow and firn densities were measured in June to a reference level which was assumed to be below

the depth of maximum percolation. In August these measurements were repeated to the same reference level and the mass change was computed. Experience from the Devon Island ice cap in arctic Canada show that the depth of maximum percolation is less than 2 m (Koerner, 1970). A depth of 2 m was therefore chosen. The density measurements were made in snow pits and samples were taken from the walls of the pit.

The mass change measurements in the accumulation area show that all melting refreezes in the snow and firn together with small amounts of summer precipitation, but the exact values of the area mass change are questionable, because the measurements only represents one point at each location. However the general trend for all measured locations in the accumulation area show that it is reasonable to assume, on a conservative basis, that the transient balance for the summer period is close to zero. The mass balance study also showed that slush several tens of centimetres thick, develops late in the melt season over vast areas of the glacier basin. The measurements indicate that most of the slush refreezes to form ice layers in the snow and firn or superimposed ice, causing local warming of the surface near layer of the glacier. Measurements of ice temperatures down to 10 metres of depth at several locations in the glacier basin reveals variations of the temperature at ten metres of depth between –20° and –17°C which seems to be related to this warming mechanism.

To elucidate the melting and refreezing processes, further work is needed including modelling of the temperature in the snow and firn based on the recorded surface near temperature data. This also includes the analysis of snow and firn $\delta^{18}O$ values to study possible seep-away of summer snow with high δ-value and fractionation in connection with refreezing of melt water. The preliminary annual balance values varies from ablation of more than 1.5 m of ice per year at an elevation of 200 m via balance around 750 m to accumulation of about 0.3 m ice equivalent at an elevation of about 1300 m.

Ice velocity and deformation measurements

Ice flow velocities were measured by repeated relative GPS surveys at all the stakes covering the glacier basin (Fig. 2). The data will serve as input for ice dynamic modelling. The stakes which were established and positioned in 1994, were positioned twice in 1995; once in June and once in August. Strain rates have been determined in three strain nets, one at the northern dome, one just below the equilibrium line of about 700 m a.s.l. and one at a location on the central part of the glacier tongue at an elevation of about 500 m a.s.l. All data have been processed to give preliminary summer, winter and annual values of vertical and horizontal velocities as well as flow directions. The data reveals that horizontal surface ice velocities on the glacier tongue range from about 5 m/yr near the terminus to about 50 m/yr near the equilibrium line at an elevation of about 750 m a.s.l. (Fig. 4) In the accumulation area, velocities are typically a few metre per year.

Stable isotope studies

Collection of surface ice, snow and firn samples for $\delta^{18}O$ analysis along the stakes in the glacier basin was started in 1994 to be compared with the $\delta^{18}O$ record from the ice core at the southern dome. Preliminary analysis of the samples from the glacier basin show large unexpected variations and trends (Fig. 5). In order to make a meaningful comparison of the $\delta^{18}O$ record from the surface of the ablation area in the glacier basin with the deep drilling

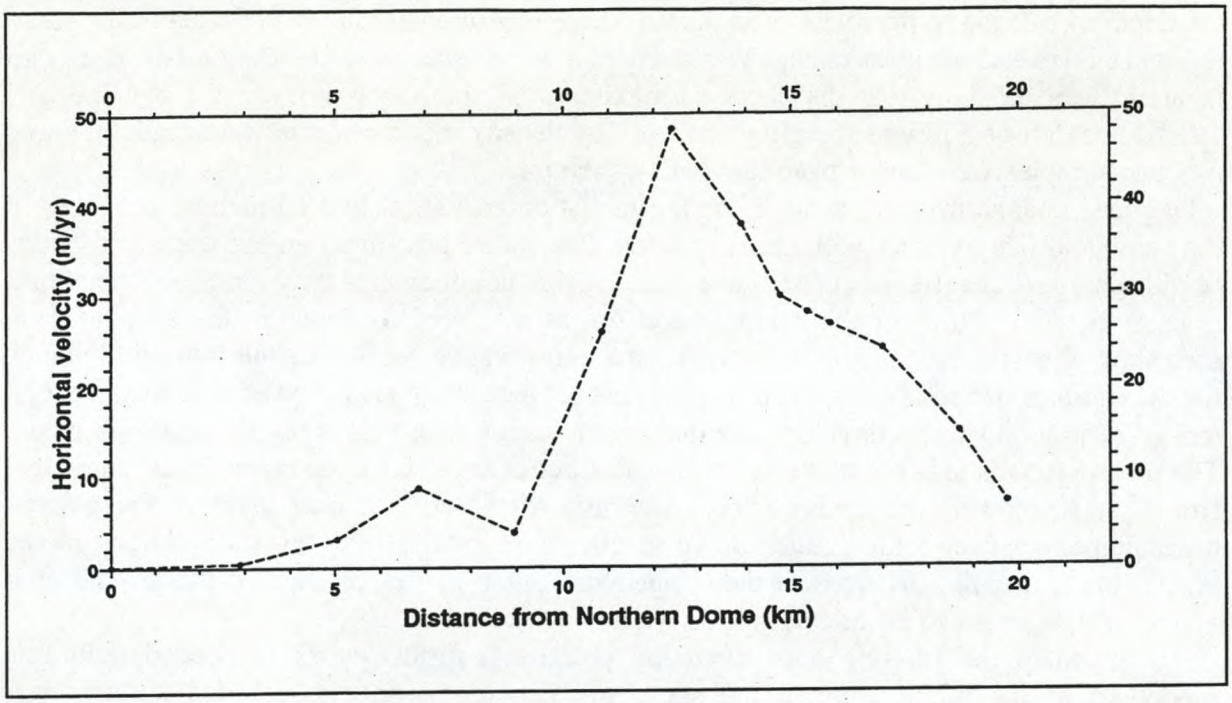

Fig. 4. Variation of horizontal ice surface velocity along the central ice flow line in the north-eastern glacier basin of Hans Tausen Iskappe. For location of central ice flow line see Fig. 2.

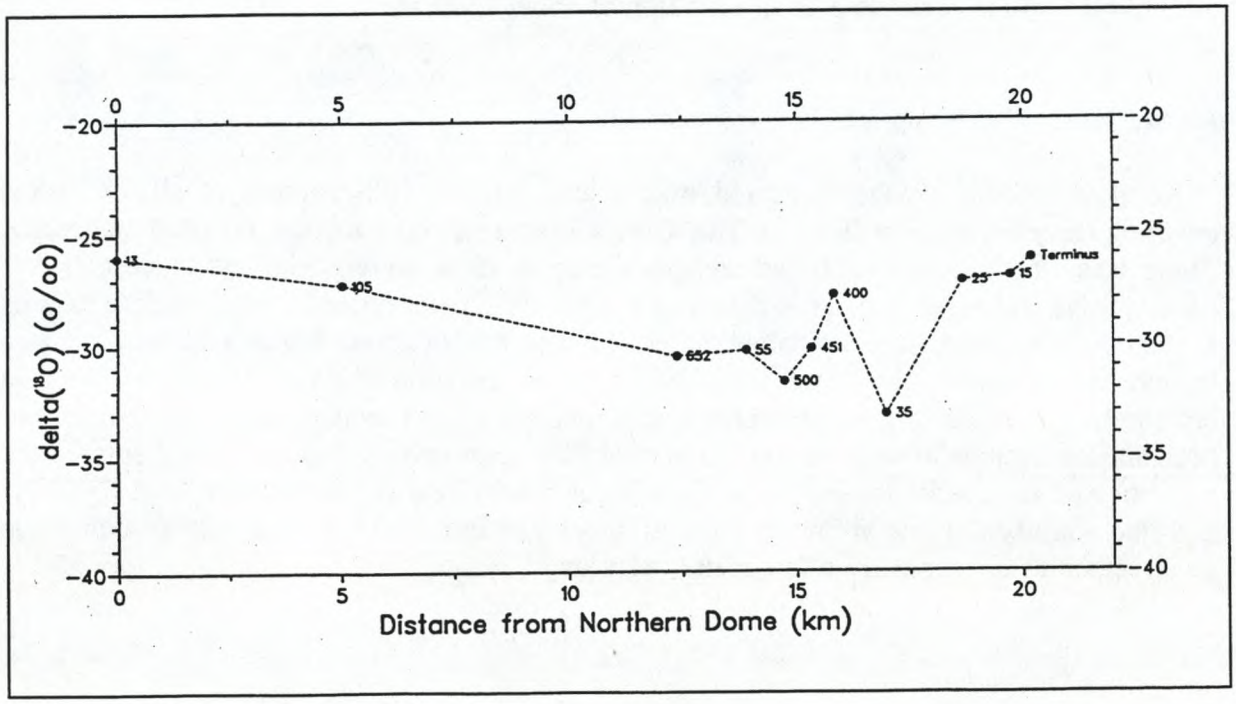

Fig. 5. $\delta^{18}O$ variation along the central ice flow line in the north-eastern glacier basin of Hans Tausen Iskappe based on sampling in 1994. For location of central ice flow line see Fig. 2. The equilibrium line is about 11 km from the northern dome. The "reverse" $\delta^{18}O$ trend in the accumulation basin (0-11 km) is confirmed by additional samples collected in June 1995.

record, the surface $\delta^{18}O$ record must be corrected for variations in the $\delta^{18}O$ content of the ice in the accumulation area of the glacier basin. Samples from snow pits and SIPRE corings in the accumulation area of the glacier basin show a pronounced "reverse" relationship of $\delta^{18}O$ with elevation. As shown in Fig. 5, a 4.5‰ increase of $\delta^{18}O$ for a 550 m increase of elevation is present in the accumulation area of the glacier basin. In order to elucidate these variations in $\delta^{18}O$ a more detailed sampling programme was carried out in August 1995. Samples were taken at all the stakes from stake 25 to 652 and at locations in between the stakes. The positions of the in between stake locations were recorded with a hand-held GPS. A total of 290 ice samples were taken from the glacier tongue area with 10 samples collected at each location. Furthermore about 60 samples of snow and firn were taken in August from the accumulation area during pit work and SIPRE coring. This sampling covered collection of snow, firn and superimposed ice at stake 13, 1053, 951, 851 and 75.

This repeated sampling confirmed the above mentioned results from the 1994 sampling programme.

A similar "reverse" $\delta^{18}O$ trend is found in the ice core drilled at the southern dome (Hammer, 1995) showing $\delta^{18}O$ values, 1.5‰ lower at the bottom 100 m, which have no counterpart in other Arctic moderately large ice cap cores. Both the above described reverse relationships could be due to heavy summer melting causing the summer snow with high δ-value not only to melt but even to seep away through the snow pack. This explanation is supported by the observation of extended slush fields developed in the summer period up to elevations of more than 1000 m in the accumulation of the ice cap.

Furthermore surface ice samples collected in 1994 near the terminus of the glacier tongue and on a glacier tongue south-east of the ice core drilling location on the southern dome (Fig. 1) indicate that ice from the last ice age is not present at the margin of Hans Tausen Iskappe. To confirm this observation additional ice samples were collected on the glacier tongue near the ice core drilling location. Here a total of 300 samples were collected along a two kilometres profile covering the outermost part of the ice tongue with a sampling interval of 5 m for the outermost first kilometre and 10 m for the rest of the profile. This additional sampling confirmed the observation that ice from the last ice age is not present suggesting that the ice cap might have melted away completely during the Holocene climatic optimum. The $\delta^{18}O$ record from the ice core drilled to bedrock at the southern dome of Hans Tausen Iskappe in Spring 1995 supports this hypothesis, showing Holocene $\delta^{18}O$ values right to the bottom (Hammer, 1995).

Preliminary results

The surface ice sampling programme for $\delta^{18}O$ analysis indicates that ice from the ice age is not present at the margin of Hans Tausen Iskappe which is supported by the results from the ice core drilling at the southern dome (Hammer, 1995). This suggests that the ice cap have melted away completely during the Holocene climatic optimum. Glacial geological studies to the north of the ice cap carried out in 1994 (Landvik & Hansen, 1994) and earlier investigations to the south and west of the ice cap (Weidick, personal communication) shows that the area adjacent to the present ice cap margin became ice-free after the last ice age about 6000-7000 years ago. Combined with the result that no ice is present from the ice age, this suggest that Hans Tausen Iskappe became extinct some time after 6000 BP and that the present ice cap started to build up in the mid-Holocene. This is in contrast to the Canadian Arctic ice caps at similar high northern latitudes which survived the Holocene climatic

optimum, thus indicating that the eastern North Greenland is highly sensitive to climate change.

The present results from mass balance and englacial temperature studies and studies of $\delta^{18}O$ variations indicate the presence of an efficient warming mechanism probably due to the development and refreezing of extended slush fields on the ice cap. This heat wave may propagate to the bottom of the ice and warm up the basal layers of the glacier with the effect of increasing ice flow velocities and thus enhance the tendency for ice cap deterioration. Similar but even more pronounced conditions is likely to have occurred during the Holocene climatic optimum leading to the disintegration of the ice cap.

However, to quantify this conclusion in terms of modelling, the varied processes involved will require a large effort as regards data analysis, compilation and interpretation as well as developing and running models for glacier mass balance and thermodynamics.

Acknowledgement:

The GPS positioning was performed by means of Trimble Receivers which was kindly lent to us by the Department of Geophysics, Niels Bohr Institute, University of Copenhagen and the National Survey and Cadastre, Copenhagen.

References

Blatter, H. 1985: On the thermal regime of Arctic valley glaciers; a study of the White Glacier, Axel Heiberg Island, and the Laika Glacier, Coburg Island, N.W.T., Canada. Zürich: Eidgenössische Technische Hochschule, Geographisches Institut. *Züricher Geographische Schriften* **22**, 107pp.

Braithwaite, R. J., Marty, C. & Olesen, O. B. 1995: Ablation and energy balance on Hans Tausen Ice Cap, Summer 1994. *In* Reeh, N. (ed) Report on activities and results 1993-1995 for Hans Tavsen Ice Cap Project - Glacier and Climate Change Research, North Greenland. NMR (Nordisk Minister Råd) Miljøforskningsprogram - klimaforskning, 16-28.

Hammer, C. U. 1995: Ice core drilling. *In* Reeh, N. (ed) Report on activities and results 1993-1995 for Hans Tavsen Ice Cap Project - Glacier and Climate Change Research, North Greenland. NMR (Nordisk Minister Råd) Miljøforskningsprogram - klimaforskning, 16-28.

Jonsson, P. 1995: Mission Report on an Impulse Radar Experiment at NE Greenland. Lund University, Dept of Engineering Geology Report no ISRN: LUTVDG/TVTG-3047-SE, 8 pp.

Koerner, R.M. 1970: The mass balance of the Devon Island ice cap, Northwest Territories, Canada, 1961-66. *J. Glaciol.* **9(57)**, 325-336.

Landvik, J. Y. & Hansen, A. 1994: The glacial history along the northern margin of the Hans Tavsen Ice Cap, North Greenland. *In* Henriksen, N. (ed.) Express Report Eastern North Greenland 1994. Grønlands geol. Unders., 115-119.

Olesen, O. B. 1989: A Danish contribution to the family of hot-water glacier drills. *In* Rado, C. & Beaudoing, D. (ed.) Ice core drilling. *Proc. Third Internat. Workshop on Ice Drilling Technology, Grenoble, France, 10-14 Oct. 1988*, 140-148.

RECENT TRENDS IN MASS BALANCE OF GLACIERS IN SCANDINAVIA AND SVALBARD

by

Jon Ove Hagen
Department of Physical Geography, University of Oslo, P.O.Box 1042 Blindern, N-0316, Oslo, Norway.

Abstract

Mass balance measurements of glaciers in the subarctic areas of Scandinavia show a different trend than the glaciers of the high arctic area of Svalbard, European Arctic. Mass balance investigations have been conducted for longer and shorter periods in a transect from south Norway to Svalbard, from 61°N to 80°N in a sector between 10 °E to 25 °E (Fig.1). The longest continuous mass balance time series in Norway is from 1948. Since 1963 six glaciers have been monitored continuously in a profile from west to east in South Norway (61 - 62 °N). Both winter and summer balance have been measured every year. The results show a different trend on the western, maritime glaciers than on the more continental glaciers 200 km inland during the period 1962 - 1988. In the west the glaciers have been increasing in volume, while in the east the glaciers had a decreasing trend up to 1988. In the period from 1989 up till now the conditions have changed towards more positive net balance for all glaciers. Nigardsbreen (48 km^2, 61.5 °N, 7 °E) will be used as an example of the glaciers in south Norway (Fig. 2). The increase of net balance is mainly because of higher winter balance with snow precipitation up to 50 % more than the average value. The volume growth has resulted in a glacier front advance of several outlets from ice caps in western South Norway.

The main trend for the glaciers in Northern Scandinavia is towards a more positive net mass balance in the area between 66 °N to 68 °N, mainly due to higher winter precipitation, a similar tend to what has been observed also in Southern Norway. On Storglaciären(68 °N, 18.5 °E) in northern Sweden, winter, summer and net balance have been measured annually since 1947 (Fig. 3). During this nearly 50 years period 1947 - 1994 the average annual winter precipitation has shown a clear positive trend and increased about 0.5 m of water equivalents while the summer ablation has shown a negative trend and decresed about the same amount, resulting in a change in net balance from negative to positive value. The recent increase of winter precipitation as observed in Southern Norway after 1988 can also be seen on Storglaciären. However, further north, on Langfjordjökulen at 70 °N, there is no sign of changing trend in the precipitatation during the last years.

One of the longest continuous mass balance observation series in the Arctic is from Svalbard archipelago where mass balance measurements were started in 1967 on Brøggerbreen in the north-western part of the island Spitsbergen (79° N 12°E). In general no dramatic changes have occured in Svalbard during the

last 28 years (Fig. 4). The winter accumulation is stable or slightly increasing with small annual variations. The mean summer ablation is stable with no significant trend, but with large annual variations. The net balance depends on area/altitude distribution. Low altitude glaciers are steadily shrinking but with slightly less negative net balance than 28 years ago. Glaciers with high altitude accumulation area are close to equilibrium. There is no sign of increased melting during the observation period.

This abstract is published as a full paper with references in:
Hagen, J. O. 1996. Recent Trends in Mass Balance of Glaciers in Scandinavia and Svalbard. *Proceedings:* International Symposium on Environmental Research in the Arctic, July 1995, NIPR Tokyo. Special Issue, *Memoirs of National Institute of Polar Research*, in print.

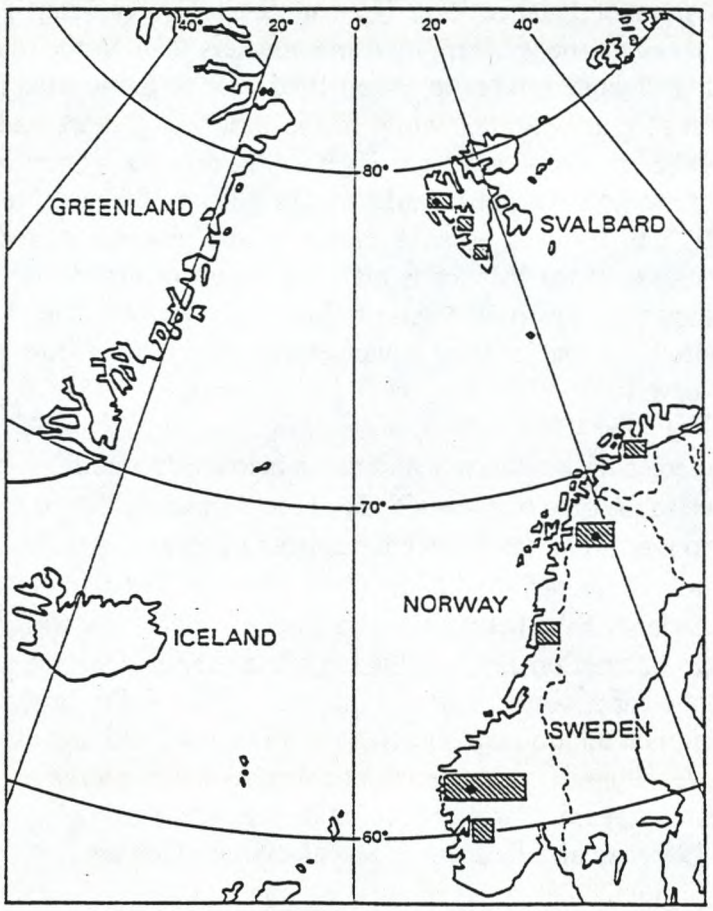

Fig. 1. Shaded areas showing main glaciated areas in Scandinavia and Svalbard where mass balance data exist. The black dots show the location of the three glaciers used in Figs. 2,3 and 4,

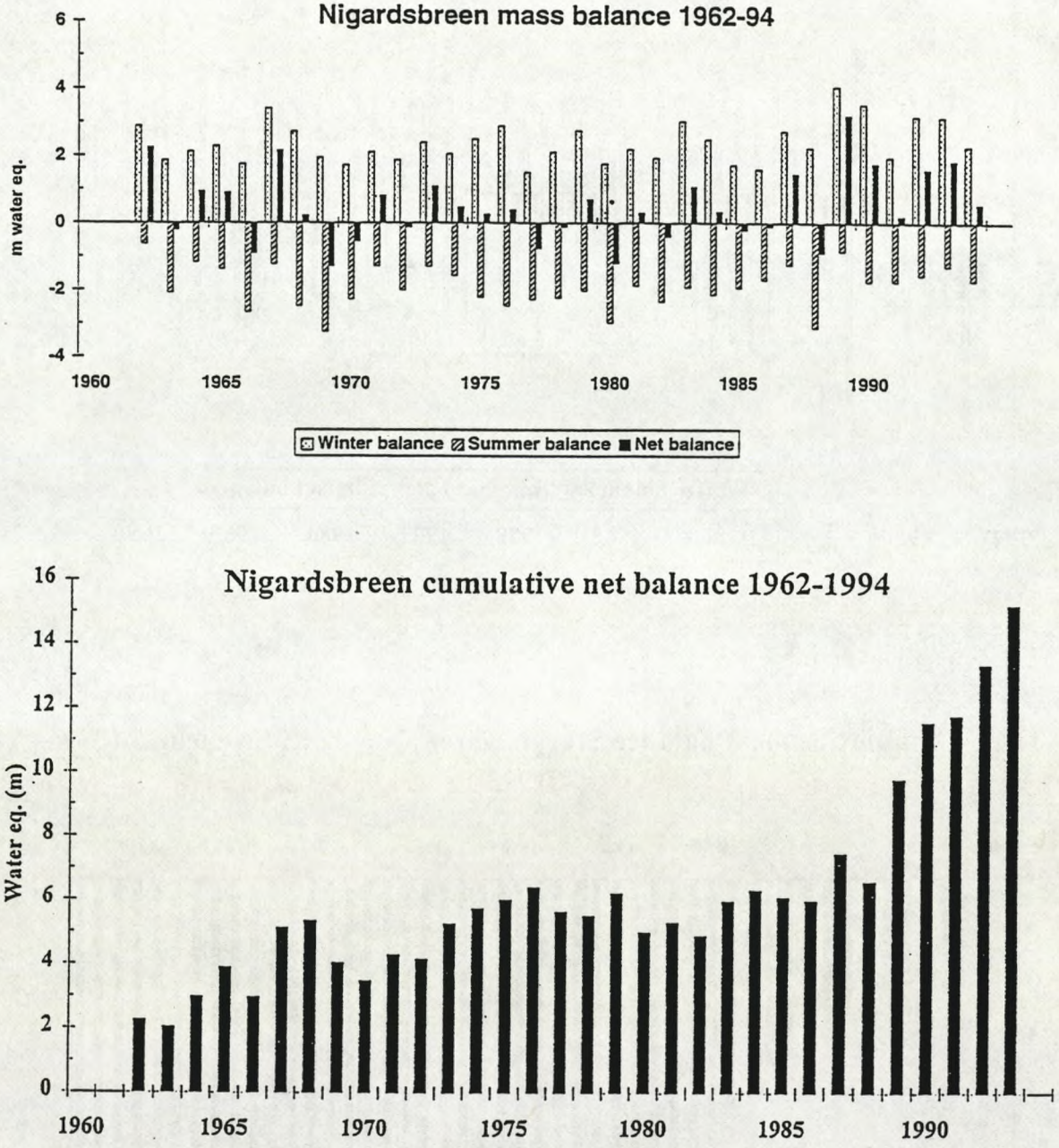

Fig. 2. Annual mass balance results from Nigardsbreen (48 km^2, 61.5 °N, 7 °E) in South Norway given in specific values (upper) and cumulative net mass balance (lower) showing the increasing trend since 1989 typical for glaciers in South Norway.

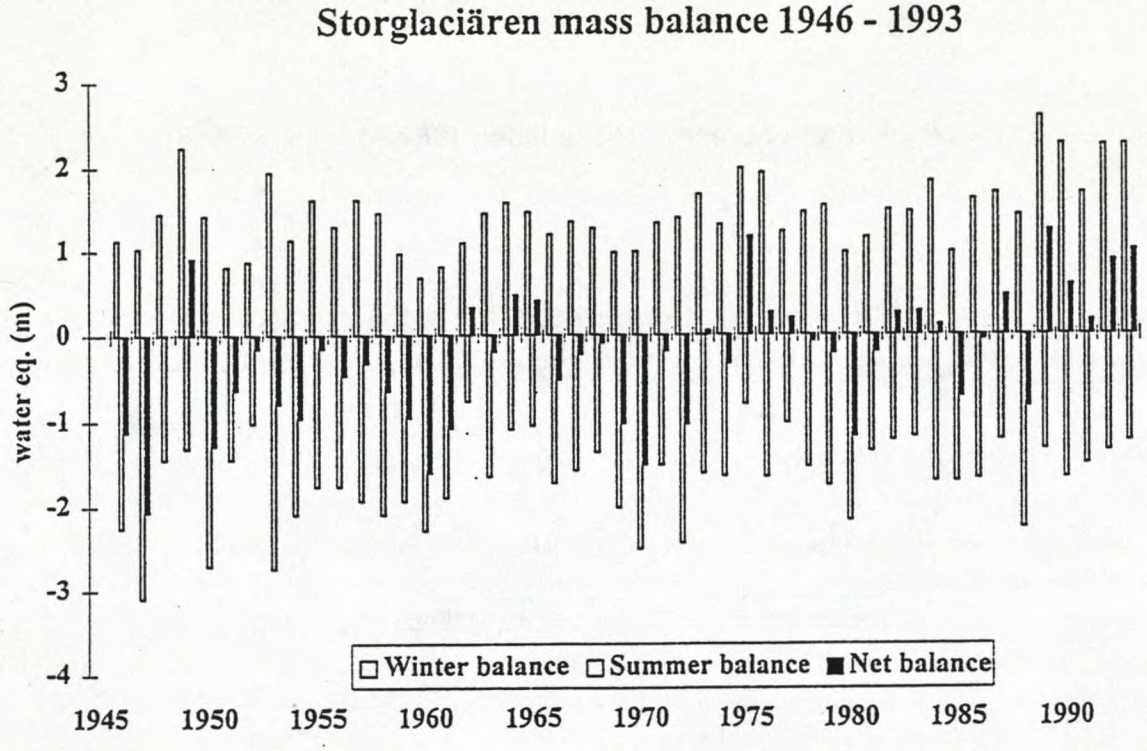

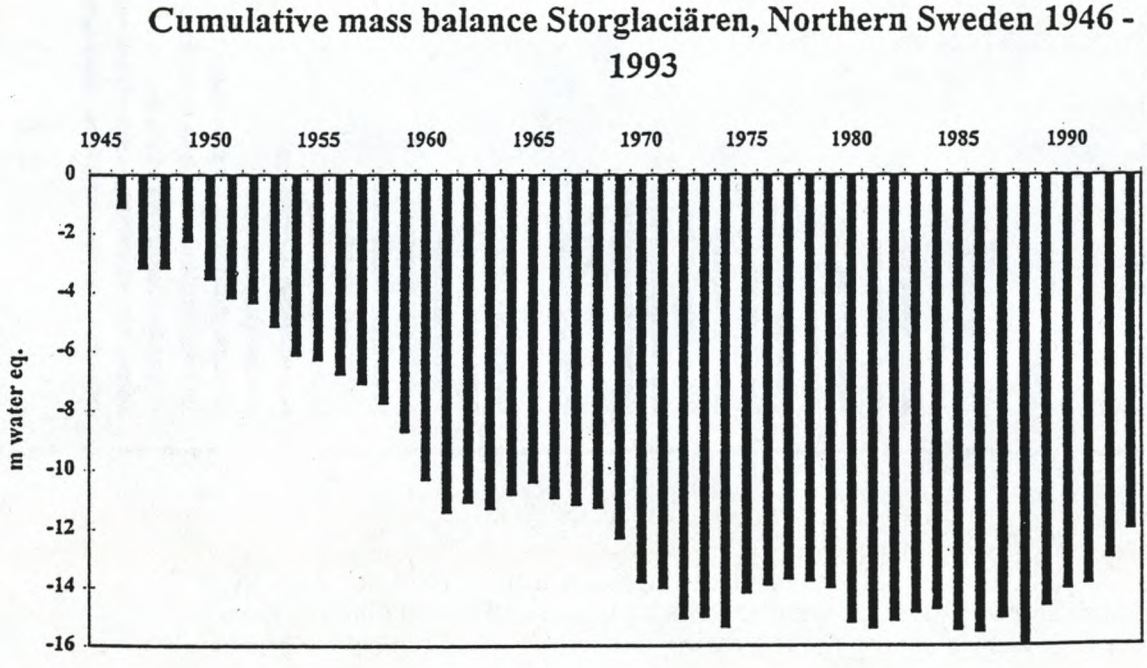

Fig. 3. Annual (upper) and cumulative (lower) mass balance results from Storglaciären (3.1 km^2, 67.9° N 18.6°E), in northern Sweden showing the change from a stable decreasing glacier to a less decrease and then an increasing trend since 1989.

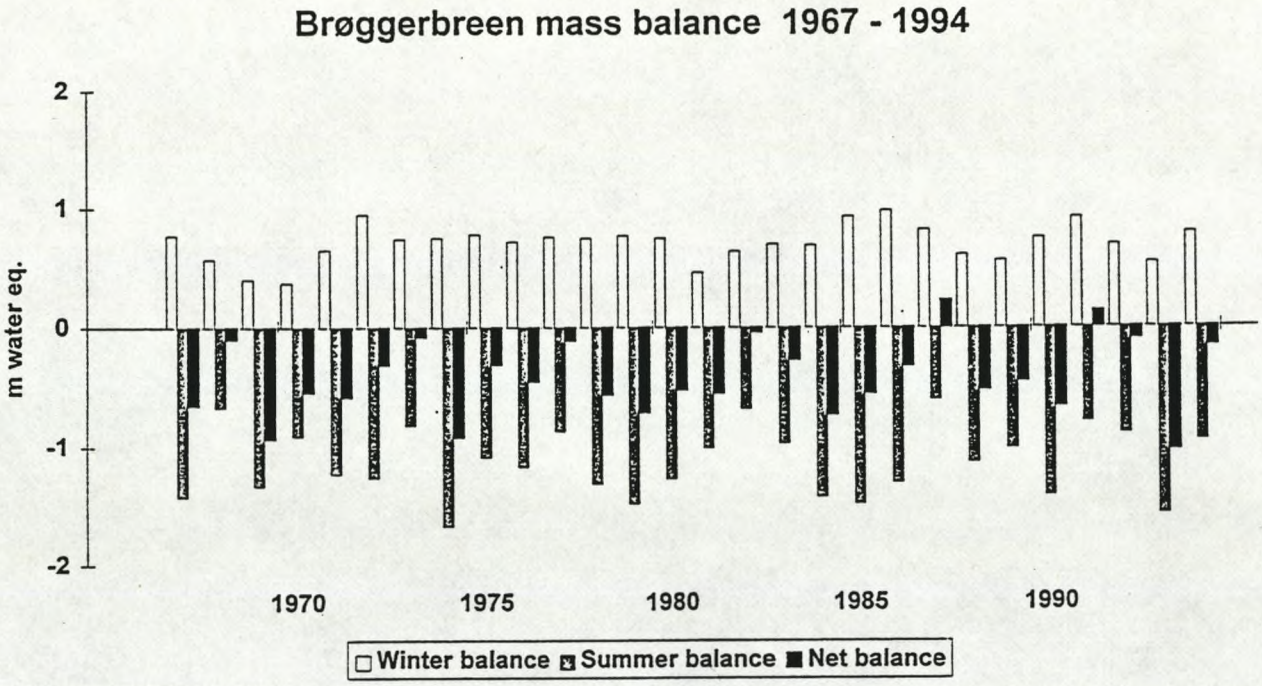

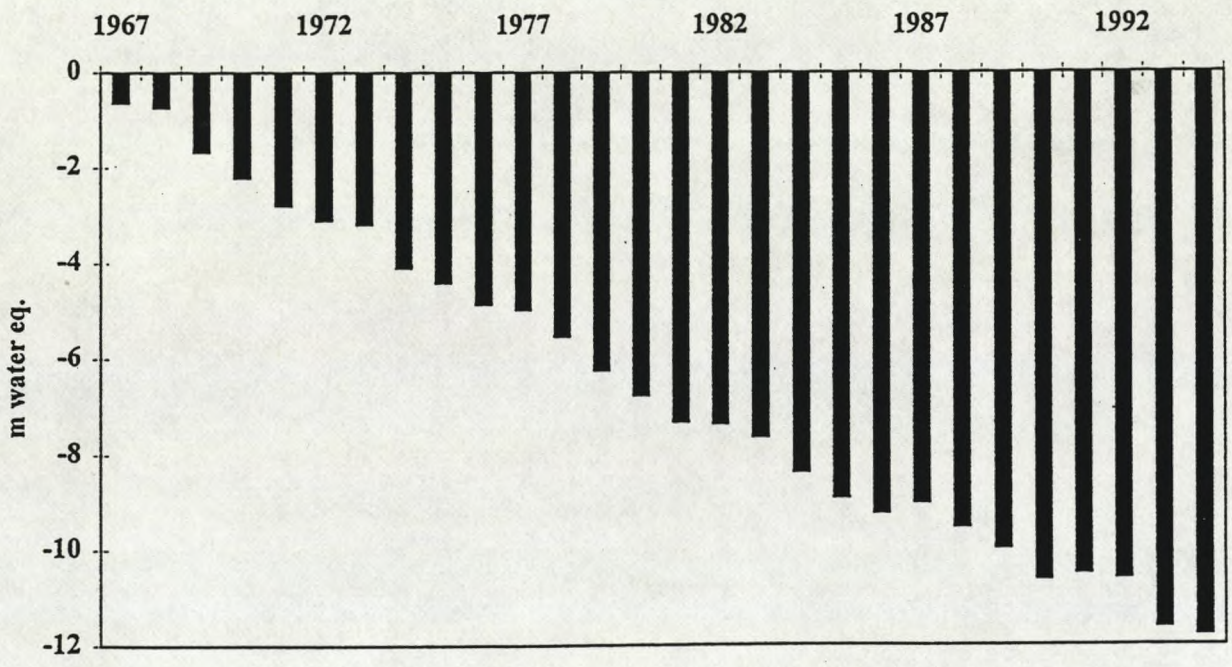

Fig. 4. Annual (upper) and cumulative (lower) mass balance results from Brøggerbreen (6.1 km^2, 79° N 12°E), Svalbard showing a stable decreasing ice mass with no significant change during the last years.

LATE GLACIAL LAURENTIDE ADVANCE OF ICE ACROSS HUDSON STRAIT AT YOUNGER DRYAS TIME: NUMERICAL MODELING OF ADVANCE OF A CALVING GLACIER TERMINUS

W. T. Pfeffer; J. Dwyer; C. Sassolas; M. Dyurgerov; M. Kaplan; A. Jennings. Institute of Arctic and Alpine Research and Department of Geological Sciences, University of Colorado, Boulder CO, 80309-0450, USA.

The discharge of large quantities of glacier ice into the North Atlantic has been suggested as possibly forcing the cessation of North Atlantic Deep Water formation, and consequently blocking the release of oceanic heat to the atmosphere in the Atlantic region. Heinrich event H-0 in the North Atlantic and detritus carbonate event DC-0 in the Labrador Sea are broadly contemporaneous with Younger Dryas climatic cooling at ca. 11 - 10 ka BP (Andrews et al, 1995). Terrestrial glacial geological investigations on Southern Baffin Island have clearly delineated the spatial and temporal structure of two advances of ice across Hudson Strait from Labrador onto Southern Baffin Island between 9.9 and 8.4 ka BP (Kaufman et al, 1993; Manley, 1995). The purpose of the modeling described here is to determine whether the pattern of advance, retreat, and calving inferred from the terrestrial and marine geologic records can be reproduced in a numerical model which allows for fairly realistic treatment of ice flow dynamics, basal sliding, flotation and calving, terrestrial topography, ice geometry, and mass balance. We use the flux-based 'quasi three-dimensional' finite element model developed by Fastook (1989), modified by us to include longitudinal coupling of stresses, floating ice, and calving. The calculation solves for the time-varying ice height at nodal points in a two-dimensional horizontal map space.

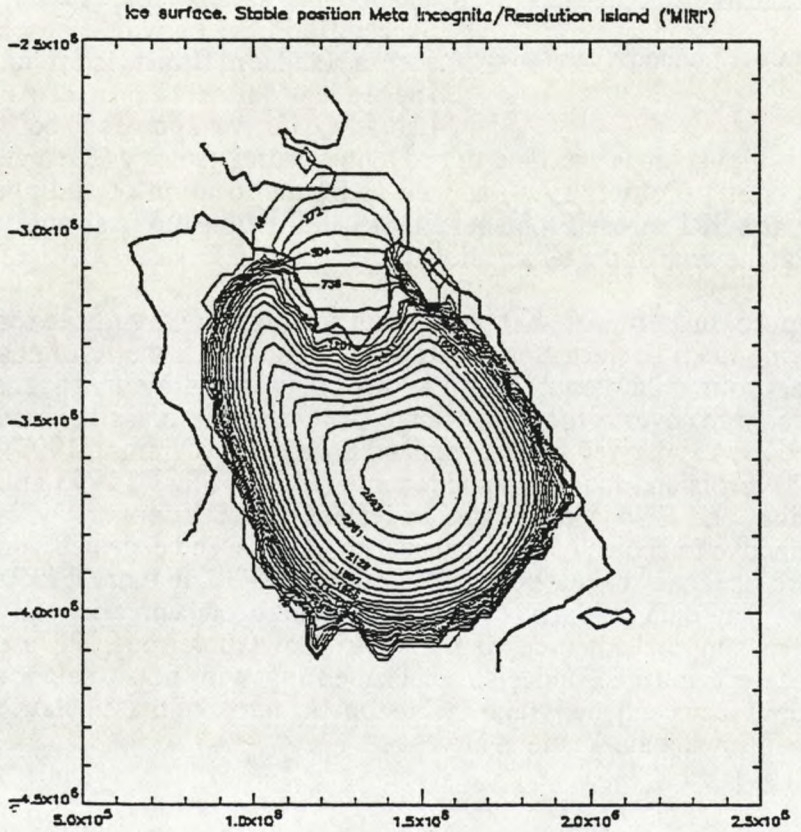

Figure 1. Stable advanced position grounded at MIRI after 400 years model time. Contours show ice surface elevation in meters above modern sea level.

Mass balance is determined parametrically and can be made to vary with time, elevation, and position. The present model differs from earlier versions in having higher spatial and temporal resolution and by allowing floating ice and a wider range of calving behavior. In addition to confirming the extent and timing of glacier advance and retreat, the model output provides calving fluxes over time, which can be compared to ice and water fluxes believed to be necessary to affect North Atlantic circulation.

Model simulations are conducted in two phases: 1) initial advance from a position on Ungava/Labrador across to Meta Incognita Peninsula - Resolution Island (MIRI), and the sill separating the Eastern and Hatton Basins (Figure 1); and 2) advance from MIRI to Hall Peninsula (Figure 2). We propose that the onset of Phase 1 advance

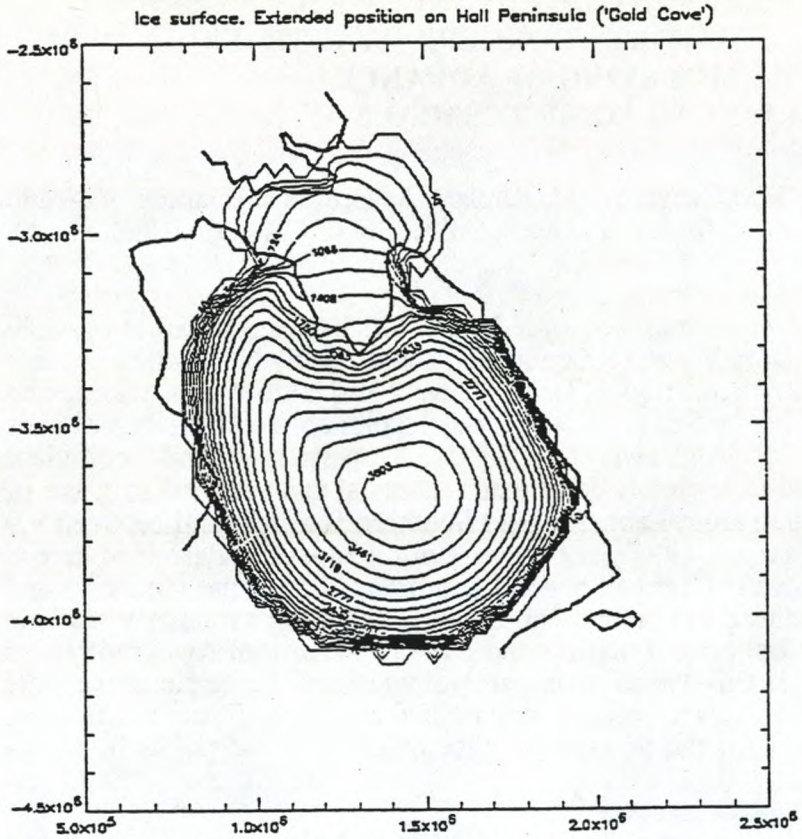

Figure 2. Unstable extended position at Gold Cove maximum past stable MIRI position.

corresponds to onset of the Younger Dryas, starting shortly before 11 ± 0.1 ^{14}C ka, and that Phase 1 concludes after the arrival of the ice margin at the stable position at MIRI. Abrupt increases in temperature and precipitation at the termination of the Younger Dryas drive the onset of Phase 2 advance. We propose that Phase 2 advance begins near 10.2 ^{14}C ka, and that the ELA rises and mass balance elevation gradient increases at this time. Rapid initial advance is driven by increased accumulation in the extended lobe over Hudson Strait. Rapid retreat after the maximum Gold Cove position occurs as upstream thinning in response to advance lowers a large fraction of the surface of the extended lobe below the ELA, abruptly exposing most or all of the lobe to ablation and forcing rapid retreat. Successful Phase 1 advance of ice across Hudson Strait from an initial position on Labrador/Ungava appears to be determined primarily by the choice of initial geometry as determined by terrestrial geology (Kleman et al, 1994) and isostatic rebound modeling (Peltier, 1994) as well as by the location of sliding, while advance from a stable position at MIRI across Frobisher Bay to Hall Peninsula is strongly dependent on mass balance conditions at the time of the termination of the Younger Dryas.

Phase 1 advance to MIRI occurs in approximately 300-400 years, with the highest calving fluxes (0.0057 Sv) occurring as ice crosses the deep Eastern Basin. After reaching MIRI, the terminus stabilizes in shallow water and appears to maintain equilibrium at this position (with consequent changes in thickness and calving discharge) over a moderate range of reasonable mass balance values. Phase 1 accumulation above the ELA is derived from Greenland EGIG data (Ohmura, 1993), while ablation data is derived from Devon Island mass balance records (IAHS(ICSCI), 1993 and previous years); accumulation, ablation, and ELA are adjusted to reflect colder Younger Dyras conditions. Phase 2 advance is very sensitive to choice of mass balance conditions, and especially on the position of the ELA. At present we use mass balance curves based on EGIG line data, GISP2 core data (Alley, 1993) and Devon Ice Cap data, but arrive at ELAs which appear unrealistically high, and consequently too warm to support advance to the Gold Cove position. We are investigating alternative mass balance constraints, and also experimenting with mass balance adjustments which allow advance to Gold Cove and are within the reasonable range of mass balance which may have occurred immediately following the Younger Dryas.

Calving flux (Figure 3) attains a maximum value of 0.0057 Sv (10^6 m^3 sec^{-1}) water equivalent as ice leaves the Ungava platform and enters the Eastern Basin. Experiments with a rule which gives a higher calving flux for a given floating ice thickness yields fluxes (calving plus ablation runoff) of 0.011 Sv, but also prevents ice from crossing Hudson Strait. Rahmstorf (1995) proposes that 0.015 Sv directed in the Labrador Sea can shut down Labrador Sea convection. While further experiments with a wider range of calving rules will increase the reliability of the modeled calving fluxes, we do not see that any reasonable rule will produce fluxes as large as 0.06 Sv, proposed by Rahmstorf as sufficient to halt North Atlantic thermohaline circulation. Nevertheless, the modeled advance from Labrador/Ungava can provide at the right time a significant fraction of the proposed 'critical' meltwater/ice flux required to affect thermohaline circulation, and may have been sufficient, taken in combination with other calving and runoff fluxes in the Atlantic Arctic, to have triggered the Younger Dryas.

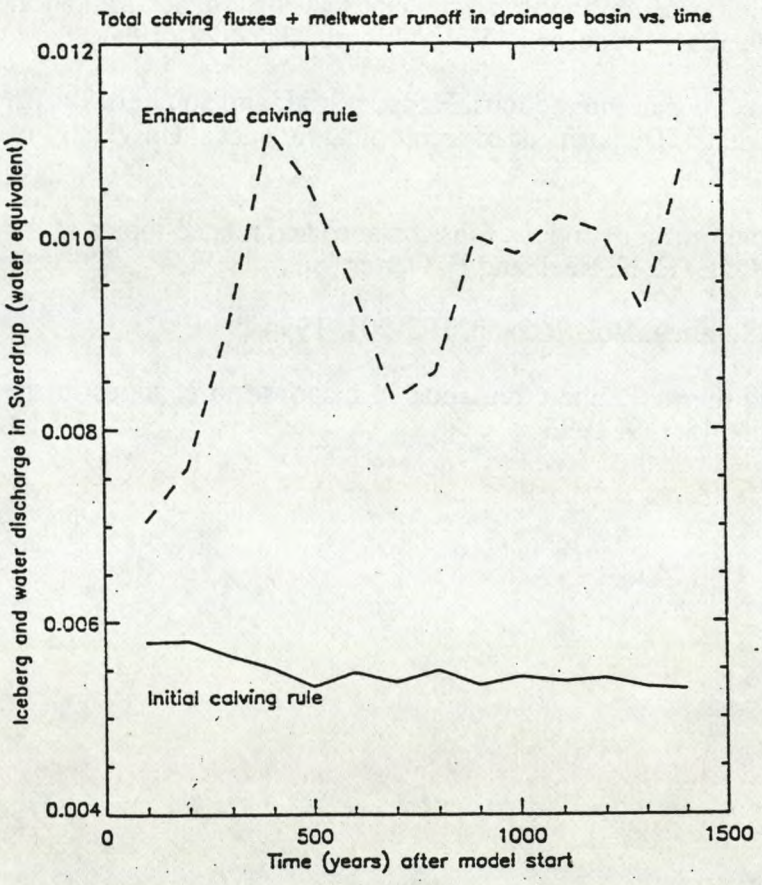

Figure 3. Calving flux plus runoff from marine based ice in Hudson Strait for times following onset of advance into Hudson Strait.

References:

Alley, R.B. Abrupt increase in Greenland snow accumulation at the end of the Younger Dryas event. **Nature**, Vol. 362, No. 8, pp. 527-529

Andrews, J.T.; A.E. Jennings; M. Kerwin; M. Kirby; W. Manley; and G.H. Miller. A Heinrich-like event, H-0 (DC-0): Source(s) for detrital carbonate in the North Atlantic during the Younger Dryas chronozone. **Paleoceanography**, Vol. 10, No. 5, pp. 943-952, October, 1995.

Fastook, J. and J.E. Chapman. A map-plane finite element model: three modeling experiments. **Journal of Glaciology**, Vol. 35, No. 119, pp. 48-52. 1989.

IAHS(ICSI)-UNESCO, Fluctuations of Glaciers, W. Haeberli and M. Hoelzle (Eds). 1993

Kaufman, D.S.; G.H. Miller; J.A. Stravers; J.T. Andrews. An abrupt early Holocene (9.9-9.6 kyr BP) ice stream advance at the mouth of Hudson Strait, Arctic Canada. **Geology**, Vol. 21, pp. 1063-1066. 1993

Kleman, J; I. Borgström; C. Hättestrand, Evidence for a relict glacial landscape in Quebec-Labrador. **Palaeogeography, Palaeoclimatology, Palaeoecology**, Vol. 111, pp. 217-228. 1994

Manley, W. Late-glacial record of ice sheet/ocean interactions, Hudson Strait and southern Baffin Island, Eastern Canadian Arctic. [PhD Thesis], Department of Geological Sciences, University of Colorado, 1995

Ohmura, A. ETH Greenland Ice Sheet Program: an overview. Mass balance and related topics of the Greenland Ice Sheet. Open File Series 93/5, ETH. N. Reeh and H. Oerter (Eds). 1993

Peltier, W. R. Ice-age paleotopography. **Science**, Vol. 265, pp. 195-201. 1994

Ramstorf, S. Bifurcations of the Atlantic thermohaline circulation in response to changes in the hydrological cycle. **Nature**, Vol. 378, pp. 145-149. 1995

SPATIAL RESOLUTION OF ICE-SHEET TOPOGRAPHY: INFLUENCE ON GREENLAND MASS-BALANCE MODELLING

Niels Reeh and Wolfgang Starzer

Dansk Polarcenter / Danmarks og Grønlands Geologiske Undersøgelse

INTRODUCTION

Both degree-day and energy-balance models for predicting the surface mass balance of ice sheets are strongly dependent on surface elevation. For example, in the degree-day model developed by Reeh (1991), melt rates are calculated from parameterizations of mean annual and mean July temperatures expressed in terms of latitude and surface elevation. Hence melt-rate estimates depend on the accuracy of the topographical model of the ice sheet surface as well as on the resolution (the grid-spacing) applied in the calculation. The higher the resolution, the more details - e.g narrow, low elevated areas with relatively high melt rates - will be represented in the model. Therefore, by using a low-resolution topographical model of the ice sheet surface, the surface mass balance will be overestimated, because ice melt tends to be underestimated. The calculation of accumulation is less affected by the resolution, because the generally smoother topography of the accumulation area is sufficiently well represented even in a low-resolution topographical model.

Another source of error in connection with estimating ice-sheet mass balance is related to the fact that grid-cell areas are often measured in a plane map. However, map projections are in general not area true. This means that e.g. a 20 by 20 kilometre grid cell in the map represents an area of the globe which is different from 400 square kilometres (20 times 20 equals 400).

In this paper, the errors introduced in surface mass balance calculations caused by the discrete representation of the ice-sheet surface topography and the map projection will be discussed. It is shown that the errors may be up to 20% for recently applied models of the Greenland ice sheet (e.g. Huybrechts et al. 1991, van de Wal and Ekholm, in press). Errors of this order of magnitude are probably still small as compared to errors arising from the uncertainty of the parameters used to describe model physics (e.g. degree-day factors in degree-day models and albedo in energy balance models). However, this does not justify errors that can be avoided.

MAP PROJECTION

In the topographical model of the Greenland ice sheet used by Huybrechts et al., 1991, the ice-sheet surface was given on a 20 km by 20 km grid spread over a

polar-stereographic map projection with standard parallel at 71°N, see figure 1. It appears from the figure that north of the standard parallel, areas in the projection are smaller than the corresponding areas on the Earth, whereas south of the standard parallel areas in the projection are larger than the corresponding areas on the Earth.

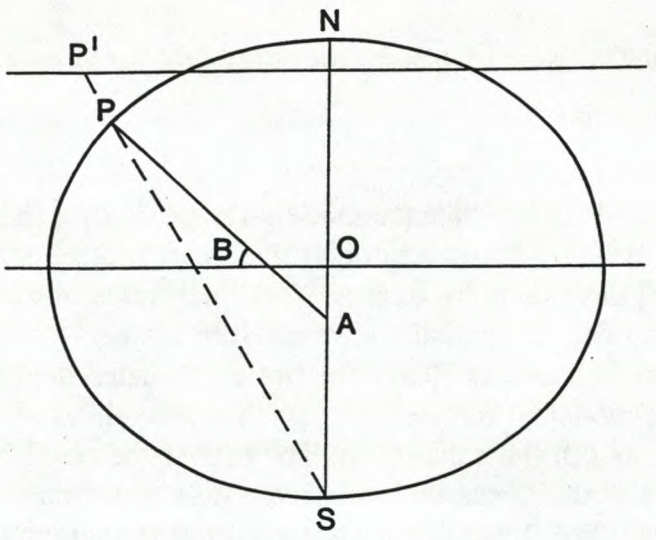

Figure 1. Polar-stereographic projection.

Using a spherical representation of the Earth with radius R, map coordinates (east-west coordinate x and south-north coordinate y) are calculated as follows:

$$x = 2\ R\ k_o\ \tan(45 - 0.5B)\ \sin(L - L_o) \qquad (1)$$

and

$$y = -2\ R\ k_o\ \tan(45 - 0.5B)\ \cos(L - L_o) \qquad (2)$$

where $k_o = 0.5\ (1 + \sin(B_{st}))$, B = latitude, L = longitude.

Huybrechts et al. (1991) used R = 6371.225 km, $B_{st} = 71°$ and $L_o = -44°E$.

Area elements in the map projection, respectively on the sphere, are:

$$\text{Projection:} \quad dA_p = dx\ dy$$
$$\text{Sphere:} \quad dA_s = R^2\ dB\ dL\ \cos(B) \qquad (3)$$

By means of the equations of projection (1) and (2), the area factor $F_s = dA_s/Da_p$ is determined as

$$F_s = \cos(B)\ (1 + \sin(B))^{3/2}\ /\ (4\ k_o^2\ (1 - \sin(B))^{1/2}). \qquad (4)$$

Consequently, the contribution to the surface mass balance ΔM from a rectangular grid cell in the map with side lengths dx and dy and specific mean mass balance m_b is

$$\Delta M = F_s \, dx \, dy \, m_b \, .$$

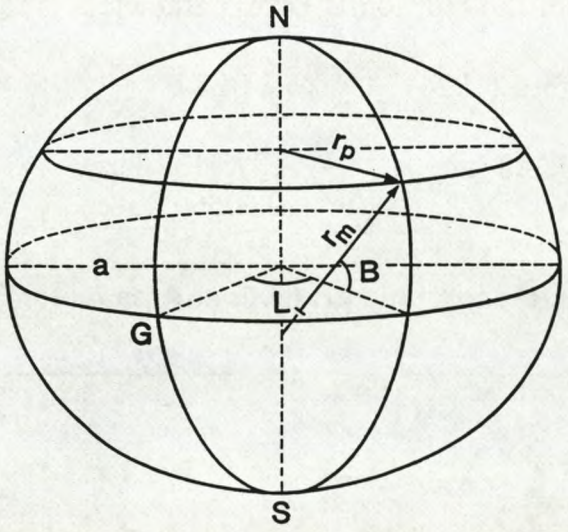

Figure 2. Ellipsoidal Earth model.

A better approximation is to use an ellipsoid in stead of a sphere to represent the shape of the Earth (figure 2). For this Earth model, the radii of curvature of a parallel and a meridian are given by the expressions

$$r_p = a \cos(B)/(1 - (e \sin(B))^2)^{1/2} \qquad (5)$$

$$r_m = a \, (1-e^2)/(1 - (e \sin(B))^2)^{3/2} \qquad (6)$$

where a is the half major axis of the ellipsoid (see figure 2) and e is the eccentricity.

An area element of the ellipsoidal Earth is given by

$$Da_e = r_m \, r_p \, Db \, Dl \, ,$$

which, by means of equation (3), can be rewritten as

$$Da_e = Da_s \, r_m \, r_p/(R^2 \cos(B)) \, .$$

By means of equations (4), (5), and (6), the area factor $F_e = Da_e/Da_p$ for the ellipsoidal Earth can therefore be written

$$F_e = (a/(2\ R\ k_o))^2\ (\cos(B)\ (1 + \sin(B))^{3/2}\ /\ (1 - \sin(B))^{1/2}\ )\ ((1-e^2)/(1 - (e \sin(B))^2)^2) \qquad (7)$$

Examples of values of the ellipsoidal Earth parameters are given below:

	Hayford (1924)	WGS84
a	6378.388 km	6378.137 km
e^2	0.00672 267	0.00669 438

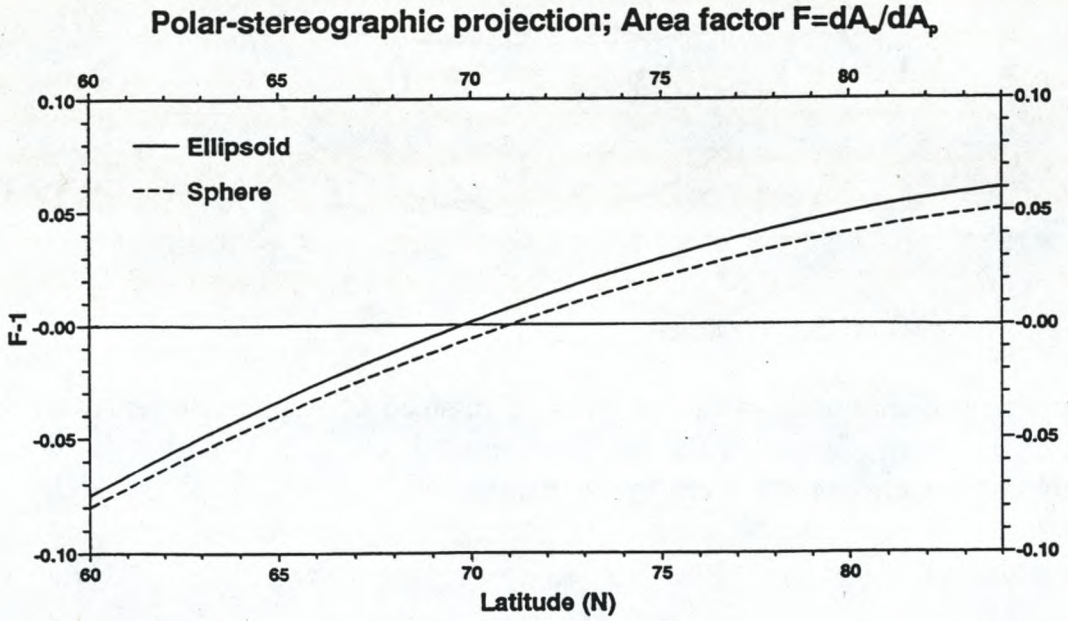

Figure 3. Area factor for conversion of areas measured in a polar-stereographic map projection.

Figure 3 shows the area factors of the spherical and ellipsoidal Earth representations versus latitude for areas measured in the polarstereographic map projection given by equations (1) and (2). For the ellipsoidal Earth representation, Hayfords values of the Earth parameters are used. However, using WGS94 values will not change the area factor significantly. It appears, that for the latitude range of Greenland (60°N - 84°N), the error introduced by using map areas instead of areas on the Earth ranges from an overestimation of 7 - 8% at 60°N to an underestimation of 5 - 6% at 84°N. These values apply to the specific map projection given by equations (1) and (2). A different map projection, will require area correction factors different from those shown in figure 3.

ICE-SHEET TOPOGRAPHY

The influence of ice-sheet topography and its resolution on Greenland mass-balance calculations is studied by comparing the results of surface mass-balance calculations using different representations of the surface topography. The mass-balance model used is based on the degree-day model developed by Reeh (1991). Accumulation rates are based on the digitization on a 20 kilometre grid (Huybrechts et al., 1991) of the map published by Ohmura and Reeh (1990). In calculations with a finer grid spacing than 20 kilometres, accumulation rates are interpolated from this dataset. As noticed by van de Wal (in press), slightly different temperature parameterizations and sets of model parameters were used in the melt-rate calculations by Reeh (1991) and Huybrechts et al. (1991). For all calculations presented in the following, the temperature parameterizations and the choice of model parameters are identical to what is used by Huybrechts et al. (1991), i.e. all calculations are performed with the same mass-balance model.

Three different topographical bases of the ice sheet are compared:

1) The EMI model as presented by Letréguilly et al. (1991) on a 20 by 20 kilometre grid laid out over the polarstereographic map projection given by equations (1) and (2) above. The surface elevations have been determined from data obtained by radio-echo sounding flights undertaken by Electromagnetic Institute (EMI), Technical University of Denmark.

2) The KMS1 model as compiled by S. Ekholm, Kort- og Matrikelstyrelsen (KMS), Denmark (Tscherning et al., 1993) given on a grid in geographical coordinates with a resolution of 5' and 10' in latitude and longitude directions, respectively, which corresponds to a grid resolution of approximately 10 km in north-south and 3 to 9 km in east-west directions. The model basis is GEOSAT satellite radar altimetry data, airborne radar altimetry and photogrammetric and manual map scanning.

3) The KMS2 model also compiled by S. Ekholm (Ekholm, in press) given on a grid in geographical coordinates with a resolution of 1.2' and 3' in latitude and longitude directions, respectively, which corresponds to a grid resolution of approximately 2.5 km in north-south and 1 to 3 km in east-west directions. The model basis is the same as for KMS1 but supplemented with ERS1 satellite radar-altimetry and airborne laser-altimetry data.

The mean accuracy of the ice sheet elevations of the KMS2 model is estimated to be 12-13 m (Ekholm, in press). For the KMS1-model, errors in the marginal zone of the ice sheet are probably of the order of 75-100m (van de Wal and Ekholm, in press), whereas the errors of the EMI model in general could be as high as 100-200 metre.

The results of surface mass balance calculations for the total Greenland ice sheets with the different topographical models are compared in Table 1:

Table 1. Area (km^2) and mass balance (km^3 of ice/year) of the Greenland ice sheet.

Column number	1	2	3	4	5	6
Topography model	KMS2	KMS2	KMS2	KMS2	KMS1	EMI(XY)
Resolution (data)	1.2'*3'	1.2'*3'	1.2'*3'	1.2'*3'	5'*10'	20km*20km
Resolution (applied)	1.2'*3'	1.2'*3'	3.6*3.6km	3.6*3.6km	3.2*3.2km	20km*20km
Planet reference	WGS84	Hayford	Hayford			
Map projection	Sanson-Flamsteed		Pol. St.	Pol. St.	Pol. St.	Pol. St.
Area correction			yes	no	no	no
Ice sheet area	1 707 038	1 707 291	1 707 404	1 685 589	1 698 435	1 670 000
Accumulation		601.8	602.1	603.2	614.6	599.3
Runoff		304.1	304.1	304.3	263.9	309.2
Surface balance		297.7	298.0	298.9	350.7	290.1
Reference	(1)	(2)	(2)	(2)	(3)	(4)

1. Weng (1995), 2. Ekholm (in press), 3. Tscherning et al. (1993), 4. Létreguilly et al. (1991)

Column 6 displays the results obtained by using the EMI model which is "born" on a polarstereographic map projection using a 20 by 20 km resolution. This results in an ice sheet area of 1,670,000 km^2, an accumulation of 599.3 km^3 of ice/year, a runoff of 309.2 km^3 of ice/year, and consequently a surface balance of 290.1 km^3 of ice/year, which on the assumption of a balanced ice-sheet budget corresponds to the loss by iceberg calving. These numbers differ from the results obtained with the same topographical model by Huybrechts at al. (1991), who calculated runoff and surface balance as 281.7 km^3 of ice/year and 317.6 km^3 of ice/year, respectively. However, the Huybrechts et al. results are erroneous because an inaccurate numerical integration procedure was used for calculating the number of positive degree days.

Column 5 presents results based on the KMS1 model. In order to be able to more directly compare the results obtained with this model to those of the EMI model, the 5'*10' resolution grid points are projected on a map by means of the polar-stereographic map projection (equations (1) and (2)). Surface elevations are then interpolated in a 3.2*3.2 km grid on the map, which is a somewhat better resolution than that of the original data set. Compared to the EMI model, the ice-sheet area is increased by about 1.7%, the accumulation has increased by 2.6%, whereas the

runoff has decreased by 14.7%. The decrease of the runoff in a higher resolution model disagrees with the expectation that inclusion of more low elevated areas with relatively large runoff in a higher resolution model should yield an increased runoff. As shown by van de Wal and Ekholm (in press), the explanation of the decreased runoff in the KMS1 model is found in the different topographical bases of the EMI and KMS models. The EMI model generally underestimates surface elevations near the ice margins, and the decrease of the calculated runoff resulting from using the higher, more correct ice margin elevations of the KMS1 model overrules the expected increase due to the higher resolution of the KMS1 model. That higher resolution actually results in an increased estimate of the runoff, is illustrated in column 4 of Table 1, showing results of a calculation using the high resolution KMS2 model. Again, in order to be able to directly compare the results obtained with this topographical model to those of the previous models, the 1.2' * 3' resolution grid points are projected on to a map by means of the polar-stereographic map projection. Surface elevations are then interpolated in a 3.6*3.6 km grid on the map which is a slightly lower resolution than that of the original data set. Compared to the KMS1 model, the ice sheet area is decreased by 0.8%, the accumulation is decreased by 1.5%, whereas the runoff is increased by 40.4 km^3 of ice/year, i.e. by 15.3%.

In figure 4, the mass-balance elevation relationship for the Greenland ice sheet as calculated by the KMS1 and KMS2 models are compared. Above 800 metre elevation, differences are insignificant. However, the lower the elevation, the larger the difference. This clearly illustrates that the increased runoff, and consequently the decreased surface mass balance calculated with the KMS2 model is due to a better representation of the low elevated areas near the ice sheet margin.

In the calculations described so far, correction for measuring areas in a plane map in stead of on the real Earth surface has been neglected. This correction has been applied in connection with the results shown in column 3 by using correction factors for the ellipsoidal Earth as given by equation (7). The effect of applying correction factors is to increase the ice sheet area by 1.3%, whereas the effect on accumulation and runoff is negligible. The increase of the ice-sheet area is due to the pronounced non-uniform latitudinal distribution of the ice-sheet area, with relatively large areas located at high latitudes, where the area factor is greater than 1. The increase of area in the northern part, therefore overrules the decrease at low latitudes where the area factor is smaller than 1. That the effect on the mass-balance values is insignificant is due to the fact that also accumulation rate and runoff have non-uniform latitudinal distributions, however with opposite trends as compared to the area distribution, so that the opposite effects of the non-uniform distributions cancel out in the mass-balance calculations.

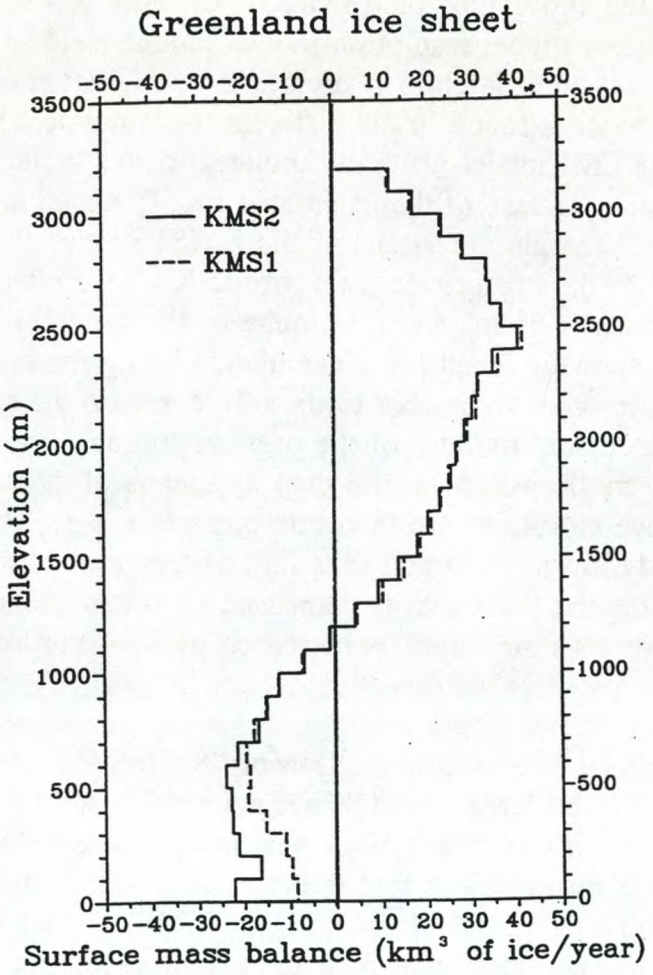

Figure 4. Distribution with elevation of the surface mass balance of the Greenland ice sheet as calculted from th4e KMS1 and KMS2 models.

Column 2 displays results of a calculation based on the original KMS2 model data as given on the 1.2'*3' resolution grid in geographical coordinates. These results deviate only insignificantly from the results of the previous column, thus confirming that errors have not been introduced by subjecting the data set to polar-stereographic projection, interpolation and area correction. Finally, in column 1, the ice-sheet area determined by KMS (Weng, 1995) is presented. It appears that, our results with the KMS2 model agrees very well with the result obtained with the same model by KMS.

CONCLUSION

It is a bit frustrating to have to conclude, that introducing a generally better model of the surface topography and increasing the model resolution by a factor of c. 100 has resulted in very small changes of the estimates of accumulation rate, runoff and

ICE-SHEET TOPOGRAPHY

The influence of ice-sheet topography and its resolution on Greenland mass-balance calculations is studied by comparing the results of surface mass-balance calculations using different representations of the surface topography. The mass-balance model used is based on the degree-day model developed by Reeh (1991). Accumulation rates are based on the digitization on a 20 kilometre grid (Huybrechts et al., 1991) of the map published by Ohmura and Reeh (1990). In calculations with a finer grid spacing than 20 kilometres, accumulation rates are interpolated from this dataset. As noticed by van de Wal (in press), slightly different temperature parameterizations and sets of model parameters were used in the melt-rate calculations by Reeh (1991) and Huybrechts et al. (1991). For all calculations presented in the following, the temperature parameterizations and the choice of model parameters are identical to what is used by Huybrechts et al. (1991), i.e. all calculations are performed with the same mass-balance model.

Three different topographical bases of the ice sheet are compared:

1) The EMI model as presented by Letréguilly et al. (1991) on a 20 by 20 kilometre grid laid out over the polarstereographic map projection given by equations (1) and (2) above. The surface elevations have been determined from data obtained by radio-echo sounding flights undertaken by Electromagnetic Institute (EMI), Technical University of Denmark.

2) The KMS1 model as compiled by S. Ekholm, Kort- og Matrikelstyrelsen (KMS), Denmark (Tscherning et al., 1993) given on a grid in geographical coordinates with a resolution of 5' and 10' in latitude and longitude directions, respectively, which corresponds to a grid resolution of approximately 10 km in north-south and 3 to 9 km in east-west directions. The model basis is GEOSAT satellite radar altimetry data, airborne radar altimetry and photogrammetric and manual map scanning.

3) The KMS2 model also compiled by S. Ekholm (Ekholm, in press) given on a grid in geographical coordinates with a resolution of 1.2' and 3' in latitude and longitude directions, respectively, which corresponds to a grid resolution of approximately 2.5 km in north-south and 1 to 3 km in east-west directions. The model basis is the same as for KMS1 but supplemented with ERS1 satellite radar-altimetry and airborne laser-altimetry data.

The mean accuracy of the ice sheet elevations of the KMS2 model is estimated to be 12-13 m (Ekholm, in press). For the KMS1-model, errors in the marginal zone of the ice sheet are probably of the order of 75-100m (van de Wal and Ekholm, in press), whereas the errors of the EMI model in general could be as high as 100-200 metre.

Ohmura, A. and Reeh, N., 1991: New precipitation and accumulation maps for Greenland. Journal of Glaciology, vol. 37, no. 125, p. 140-148.

Reeh, N., 1991: Parameterization of melt rate and surface temperature on the Greenland ice sheet. Polarforschung 59/3, p. 113-128.

Tscherning, C.C., Knudsen, P., Ekholm, S., and Baltazar Andersen, O., 1993: An analysis of the gravity field in the Norwegian Sea and the mapping of the ice cap of Greenland using ERS-1 altimeter measurements. Proceedings of the first ERS-1 Symposium - Space at the service of our environment, European Space Agency, ESA Special Publication, ESA SP-359, 413-418.

van de Wal, R.S.W., in press: Mass balance modelling of the Greenland ice sheet: A comparison of an energy balance and a degree-day model. Annals of Glaciology.

van de Wal, R.S.W. and Ekholm, S., in press: On elevation models as input for mass balance calculations of the Greenland ice sheet. Annals of Glaciology.